UNIVERSITÀ DI TORINO

PhD course in:

Pharmaceutical and Biomolecular Sciences

XXXV cycle

Relaxometric/structural characterization and preclinical development of MRI contrast agents based on paramagnetic metals (Gd, Fe)

Candidate: Lorenzo Palagi

Supervisor: Prof. Eliana Gianolio

Contents

Aim of the thesis

This PhD project aimed to investigate coordination compounds based on paramagnetic metals as potential contrast agents for magnetic resonance imaging (MRI). The manuscript describes the route starting from the design, the development and the characterization of these metal complexes, until their *in vitro* and *in vivo* validation at a preclinical level.

The first chapter is a general introduction about the main topics encountered during this PhD project. The second and the third chapters describe the development of two novel gadolinium complexes with promising potential as MRI contrast agents. The forth chapter, originated from the work carried during the period abroad spent at the MD Anderson Cancer Center in Houston, Texas, illustrates the use of different metal complexes for measuring pH in the extracellular tumor environment by a combined and simultaneous use of MRI and positron emission tomography (PET) techniques. In the fifth chapter, the original studies concerning an iron complex based on a chelator already used in clinics are reported. The sixth chapter finally presents the preliminary studies on two improved derivatives of the iron complex described in the fifth chapter.

Chapter 1

General Introduction

1.1 Magnetic resonance imaging (MRI)

1.1.1 Introduction to MRI

Magnetic resonance imaging (MRI) is a non-invasive diagnostic medical imaging technique widely employed to generate high quality images of the inside of the human body, through the use of powerful magnets and low-energy radiofrequency (RF) pulses.[1] After its first clinical applications in the early '80s, MRI has been routinely used in the last 40 years for disease detection, diagnosis and therapeutic treatment monitoring. Unlike other imaging methods, MRI does not rely on ionizing radiations, making it a safer option.[1]

MRI is based on the nuclear magnetic resonance (NMR) principle: nuclei of atoms that possess spin, when placed in a magnetic field, absorb and emit energy at a specific radiofrequency. Nuclear spin or, more precisely, nuclear spin angular momentum, is one of several intrinsic properties of an atom and its value depends on the precise atomic composition. The nucleus can be seen as a charged sphere constantly rotating around an axis at a constant rate or velocity. This self-rotation axis is perpendicular to the direction of rotation. A limited number of values for the spin are found in nature: it is quantized to certain discrete values that depend on the atomic number and atomic weight of the particular nucleus.[2] In addition to its spin, a positively charged nucleus also possesses a local magnetic field or magnetic moment. For a nucleus, this magnetic moment is parallel to the axis of rotation. The orientation of the nuclear spin and the modifications it undergoes due to experimental manipulations applied to the nucleus, provide the basis for the MR signal.

Given the presence of hydrogen in all biological components, the ^{1}H nucleus, consisting of a single proton, is a natural choice for probing the human body with MRI. Furthermore, the response of ^{1}H to an applied magnetic field is one of the largest found in nature. Therefore, MRI can efficiently rely on protons within water, fat, and other chemical constituents.[3]

In MR, the nucleus (e.g., ^{1}H) rotates perpendicular to, or precesses about, the static magnetic field B_0 of the spectrometer magnet. This precession will occur at a frequency (ω_0) imposed by the nature of the nucleus and the strength of the magnetic field of the magnet: $\omega_0 = \gamma B_0/2\pi$ (Larmor equation). The Larmor frequency ω_0 is expressed in MHz and the magnetic field strength B_0 in T. The gyromagnetic ratio γ is a constant for each nucleus and is expressed in $s^{-1}\,T^{-1}$. The two possible ways of precession (parallel and antiparallel to B_0) correspond to two energy states in the presence of a strong magnetic field. According to the Boltzmann distribution, there are more ^{1}H protons in the lower level (parallel to B_0) than in the upper level.[1] Consequently, there will be total net magnetization (M_0) of the sample, parallel to B_0 (by definition, the z axis). The z component of the spin vector is the component of interest because it does not change in magnitude or direction as the proton precesses. The x and y components vary with time at a frequency ω_0 proportional to B_0 as expressed by Larmor equation. A schematic representation of this process is shown in Figure 1.1.

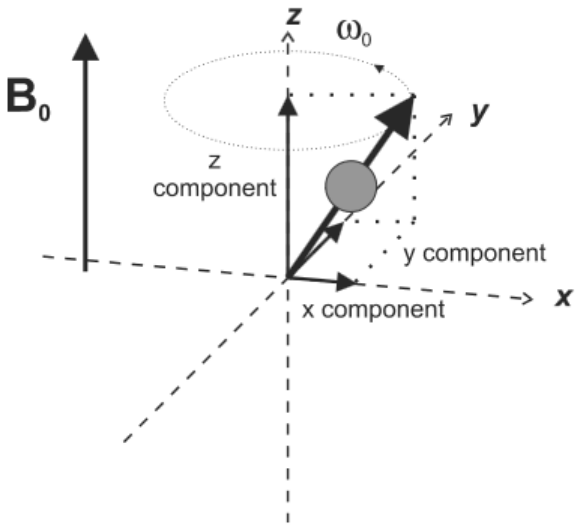

Figure 1.1. Inside a magnetic field, a proton precesses about the magnetic field. The precessional axis (z) is parallel to the main magnetic field B_0. Modified from [4].

Since the magnetization of the spins is parallel to the main magnetic field, it is not feasible to detect the signal from these spins. To enable signal detection, the magnetization must be shifted out of alignment with the main field and into the xy-plane. To achieve this, an RF pulse is employed, which reorients the magnetic field perpendicular to the main magnetic field, enabling its detection by a surrounding RF receiver coil (Figure 1.2c).

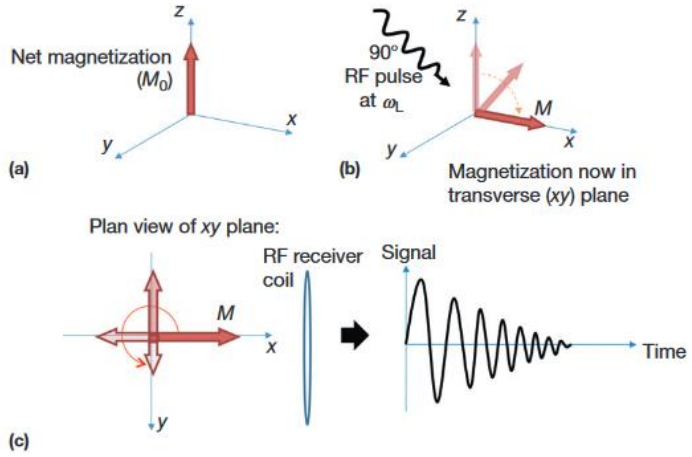

Figure 1.2. Schematic diagram of the creation of an MR signal. **(a)** The net magnetization is initially along the z-axis before excitation. **(b)** After a 90° pulse at the Larmor frequency, the magnetization is transferred into the xy-plane. **(c)** In the xy-plane, the spins precess around the z-axis, initially in phase but slowly becoming out of phase with time. This causes the decay in signal. Modified from [3].

It is crucial for the RF pulse to match the Larmor frequency for resonance. Therefore, a magnet, tissue, transmitter, and receiver coils constitute the fundamental components necessary for capturing an NMR signal.

MRI images are obtained through the spatial localization of protons present in the observed tissues and they are constructed by combining thousands of individual signals from different parts of the body. This process is called data acquisition. The data acquisition process can be divided into excitation and detection. During the excitation step, the MRI scanner applies a strong magnetic field and radio waves to the body. This causes the hydrogen atoms to absorb energy and realign themselves. During the detection step, the scanner measures the radio waves that are emitted from the body as the hydrogen atoms release the absorbed energy.[5] The data acquisition process is repeated many times from different angles around the body. This allows the MRI scanner to reconstruct a three-dimensional image of the body. Modern MRI applies a temporary gradient across the subject, acquiring RF signals, with a frequency and/or phase that are dependent on the position in the subject, which are decoded with a Fourier transform to produce an image.[6] The final processing to produce a MR image involves various steps. Through the signal filtering of the raw signals, noise and unwanted frequencies are removed. The filtered signals are then used to reconstruct the image that may be enhanced to improve contrast and readability. The final MR images are a representation of the distribution of hydrogen atoms in the body and it can be used to diagnose a variety of medical conditions.[5]
Tissue discrimination is obtained by virtue of the difference in relaxation times of nuclei in various positions, so that the features are determined by the rate at which excited atoms return to the equilibrium state. The magnitude of the obtained RF signal depends on the number of nuclei present (a property called spin density). The shape depends on the time it takes for the nuclei to relax. The MR signal that is received undergoes a relaxation process, returning to its pre-excitation state through two independent but concurrent mechanisms known as T_1 and T_2 relaxation.

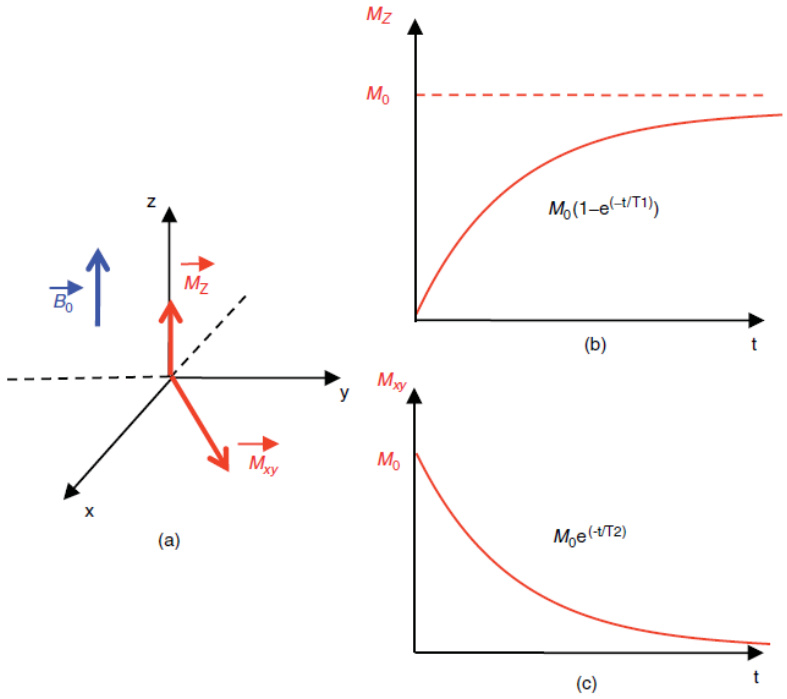

Figure 1.3. (a) Return to equilibrium of the magnetization. **(b)** Return to equilibrium on the z axis: ($M_z = M_0 (1-e^{-t/T_1})$). **(c)** Return to equilibrium in the xy plane: $M_y = M_0\, e^{-t/T_2}$. Modified from [7].

The longitudinal relaxation time T_1 (Figure 1.3b) reflects the return to equilibrium of the magnetization (Figure 1.3a) along the z-axis ($M_z = M_0\ (1-e^{-t/T1})$) and involves the spins' realignment along the main magnetic field.[7] This phenomenon results from the enthalpic interaction of the excited nucleus with its surrounding environment, particularly with magnetic active agents within this environment (i.e., ^1H protons and unpaired electrons e^-). For the relaxation to occur, a movement among the molecules (Brownian motion) is needed. Such motion of nuclear magnetic moments of other molecules (or unpaired e^-) induces a distribution of frequencies. Within this range of frequencies, the resonance frequency of the excited nucleus can be found, leading to stimulated relaxation. T_1 longitudinal relaxation, also called spin-lattice relaxation, relies on the mobility of these entities and, in turn, on the viscosity of the environment.

On the other hand, the T_2 transversal relaxation time is characteristic of the decay of the signal in the xy plane (Figure 1.2c).[7] This relaxation process, also called spin-spin relaxation, is driven by entropy and corresponds to the dephasing of nuclear spins in the xy plane. T_2 is always shorter than T_1. In MRI, a frequently employed parameter is the relaxation time T_2*: it encompasses both T_2 and the effects of magnetic field inhomogeneities, including those specific to the sample being studied. T_2* is, therefore, associated with distinct properties of the examined tissue and proves to be highly valuable in the realm of medical MRI.

As mentioned above, the spatial distribution of the spin density of a specific atom, usually water protons, can generate a MR image. The intensity of the MRI signal is influenced by intrinsic and extrinsic factors, including proton spin density, longitudinal (T_1) and transverse (T_2 or T_2*) relaxation times, chemical shifts, and instrumental parameters. Tissues naturally exhibit variations in their MRI signal intensities. These differences can be accentuated by employing specific MRI sequences that allow for adjustments in instrument parameters. Moreover, to enhance the visibility of structures such as vascular systems, inflammatory regions, tumors, and other features, the application of suitable contrast agents (CAs) becomes crucial. These CAs serve to amplify the contrast in the MR images, aiding in the precise visualization and characterization of various tissues and pathological conditions.

1.1.2 MRI contrast agents

MRI contrast agents (CAs) are substances that can interact with water protons and alter their relaxation times. Their role in medicine is crucial, as they can highlight the differences between healthy and diseased tissues by modifying the intrinsic parameters of the tissue itself (i.e. T_1 and T_2 relaxation times). Although a great intrinsic contrast can be achieved with MRI without the use of CAs, compared to other imaging techniques, contrast enhancement is needed when evaluating several diseases. Indeed, tens of millions of contrast-enhanced MRI exams are performed annually around the world.[8] Various MRI probes have been developed to create or enhance contrast, with approximately 40% of clinical scans involving their use.[9]

Overall, CAs can be classified as positive CAs, when they cause a reduction of T_1 relaxation time, and negative CAs if they are able to lower the T_2 relaxation time. In T_1–weighted images

the regions containing positive CAs appear brighter, while the regions where negative CAs are present appear darker on T_2–weighted images (Figure 1.4).
Superparamagnetic agents such as SPIONs (superparamagnetic iron oxide nanoparticles) are examples of negative CAs, as they provide darkened MR images. On the other hand, positive CAs are paramagnetic metal complexes containing lanthanides or transition metal ions. Examples of positive CAs containing transition metals are Mn(II)- Mn(III)- or Fe(III)-complexes. Undeniably, the lanthanide gadolinium is the most used metal ion in this context, and CAs containing the Gd(III) ion complexed to a chelator molecule are known as gadolinium-based contrast agents (GBCAs).

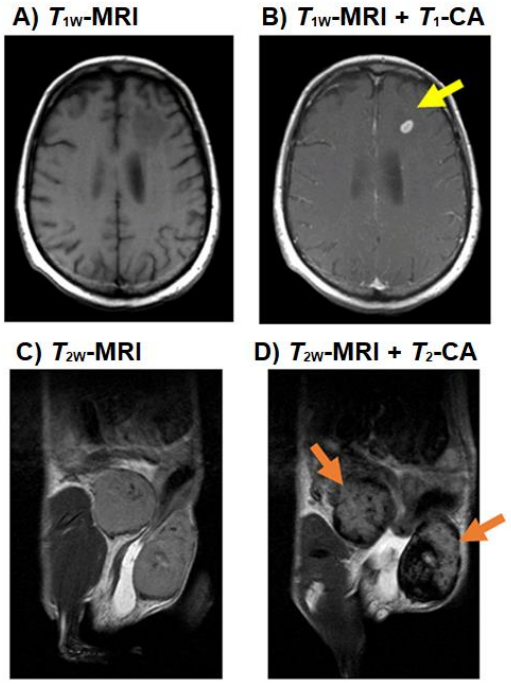

Figure 1.4. (A) pre- and **(B)** post-GBCA T_1-weighted MRI on a brain metastasis in a melanoma patient (15 min post-injection); **(C)** pre- and **(D)** post-SPION T_2-weighted MRI on inflamed mouse mammary gland tumors (24 h post-injection)**.** Modified from [10].

A third category of contrast agents, known as CEST (chemical exchange saturation transfer) agents, has emerged more recently.[11] Unlike T_1 and T_2-agents, these compounds do not directly affect the relaxation time of water protons. Instead, they contain hydrogens that can chemically exchange with hydrogens of H_2O. When the ^1H protons of these exchangeable hydrogens are selectively saturated during their exchange with water protons, it leads to a decrease in the intensity of the H_2O signal, which can be observed locally with MRI.[7]

1.1.2.1 Relaxivity of MRI CAs

The efficiency of paramagnetic CAs in MRI is determined by a property known as relaxivity (r_1 and r_2). Relaxivity expresses how much the relaxation rate of water protons can be enhanced

by a 1 mM solution of CA. A significant challenge in MRI is to reduce the amount of CA required for obtaining informative images. One approach to achieve this is by increasing the relaxivity of the CA.

Relaxivity is influenced by both external factors, such as the strength of the applied magnetic field and temperature, and the molecular properties of the contrast agent.[12] In the last 30 years, an extensive research about the molecular and structural determinants influencing relaxivity led to well-known protocols for the characterization and the validation of MRI CAs, especially in the case of the most used GBCAs.

The total relaxivity comprises multiple contributions, regarding the inner, the second, and the outer coordination spheres:

$$r_1 = r_1^{\mathrm{IS}} + r_1^{\mathrm{SS}} + r_1^{\mathrm{OS}}$$

Inner-sphere relaxivity is usually the most crucial and arises from the rapid exchange of water molecules coordinated to the gadolinium ion with water molecules in the bulk fluid. It can be expressed as:

$$r_1^{\mathrm{IS}} = \frac{[\mathrm{CA}]q}{55.6} \frac{1}{T_{1\mathrm{M}} + \tau_{\mathrm{M}}}$$

[CA] represents the concentration of the contrast agent; q is the hydration state, indicating the number of water molecules coordinated to the metal ion; τ_M is the main residence lifetime of water molecules in the inner sphere of the metal; T_{1M} is the relaxation time of water protons located in the inner sphere of the metal.[8,13]

The increase in relaxivity is directly proportional to the number of water molecules bound to the paramagnetic center and the speed at which they exchange with the surrounding water molecules. Typically, the Gd^{3+} ion has nine coordination sites, and the common use of octa-dentate ligands leaves one site available for coordination with a water molecule, resulting in $q = 1$. Reducing the denticity of the ligand can increase the hydration number and enhance the relaxivity of the complex. However, a reduction in denticity often accompanies a decrease in thermodynamic stability, which is a crucial feature for CAs.[14,15] The exchange speed is determined by τ_M. Beyond a certain value, a higher τ_M leads to lower relaxivity and reduced CA efficiency. The structural characteristics of CAs, such as their size, shape and charge, can influence the mean residence time of each water molecule on the paramagnetic center. The longitudinal relaxation rate ($1/T_{1M}$) is significantly influenced by the correlation time τ_C, that is the shorter of the rotational correlation time (τ_R), the electronic relaxation time (T_{1e}), or the water residency time (τ_M):[8]

$$\frac{1}{\tau_{\mathrm{C}}} = \frac{1}{\tau_{\mathrm{R}}} + \frac{1}{\tau_{\mathrm{M}}} + \frac{1}{T_{1\mathrm{e}}}$$

In clinical imaging, especially at common magnetic field strengths (0.5 - 1.5 T), and for small rapidly tumbling complexes, τ_C is dominated by the rotational (or reorientational) correlation time τ_R, which represents the rotational dynamics of the molecule.[14] Increasing τ_R by reducing

the molecular tumbling can enhance relaxivity. This can be achieved, for example, by attaching CAs to molecules with high molecular weight, both covalently or non-covalently.[16]

1.1.2.2 Gadolinium(III)-based MRI contrast agents (GBCAs)

GBCAs are the most widely used class of MRI CAs and one of the most successful examples of inorganic diagnostic agents, as they provide fundamental diagnostic information that is often unobtainable with other noninvasive technics.[8]

Gadolinium belongs to the lanthanide group of the periodic table. Since it contains 7 unpaired electrons, the Gd(III) ion exhibits strong paramagnetism. These unpaired electrons are able to reduce the relaxation time of nearby water protons. Although Gd(III) ion is very effective as a CA, it is toxic, so it must be always used as a very stable chelate. Its toxicity is due to the low solubility at physiological pH, resulting in a slow systemic excretion, and to the competition with the endogenous Ca(II) ion. Being the two metal ions very similar in size, gadolinium can interfere with various biological pathways that are normally controlled by calcium.[17] Chelating molecules are required to encapsulate the gadolinium ions, preserving their paramagnetic properties while reducing their toxicity. Consequently, the stability of these metal complexes must be very high.

Structurally, GBCAs can be categorized into two groups based on the type of chelator employed, namely linear and macrocyclic. Linear agents are made by an elongated chelator that wraps around Gd^{3+}, while macrocyclic agents are characterized by a cage-like structure with Gd^{3+} trapped in a central cavity. It has been demonstrated that macrocyclic GBCAs offer greater stability compared to linear GBCAs, making them the preferred choice in the development of new contrast agents.[9] Indeed high thermodynamic stability and kinetic inertness are crucial for GBCAs due to the well-known toxicities of the dissociated metal ions. It is believed that kinetic inertness is the most critical factor regarding Gd(III) release.[8]

In the past, a devastating disease named nephrogenic systemic fibrosis (NSF) has been identified in renally impaired patients undergoing multiple doses of GBCAs.[8] Although the risk is considered very low, most NSF occurs after exposure to linear contrast agents.[18] In recent years, increased attention has also been dedicated to the observation that small amounts of GBCAs, administered intravenously, can extravasate from the bloodstream and enter the extracellular extravascular compartments of the body, and potentially being retained for long time.[19–21] Of particular concern is when the organ retaining Gd is the brain, although no clinical implications have been demonstrated yet.[22,23] In numerous studies, linear GBCAs have demonstrated a higher propensity to release gadolinium, leading to Gd retention in the body.[24–26] The more stable macrocyclic GBCAs are expected to flow intact through the glymphatic pathway, although their transit times may vary significantly from one agent to another.[9]

Nevertheless, the wide employment of gadolinium enhances the risk for this element to be potentially released into the environment, in particular into rivers, lakes and coastal areas through industrial wastewaters or exhausted devices. Although still limited information exists about the effects induced to aquatic organisms by Gd, its impacts in invertebrate aquatic species were identified at different biological levels, such as alterations on gene expression,

cellular homeostasis, shell formation, metabolic capacity and antioxidant mechanisms.[27] Consequently, gadolinium may represent an environmental threat and a risk to human health.[28] Further research on Gd toxicity towards aquatic wildlife as well as the development of new water remediation strategies are definitely needed.

1.1.2.3 Iron(III)-based MRI contrast agents

In recent times, concerns over gadolinium retention in the body along with the potential environmental threat, have stimulated renewed interest in Fe(III) complexes as potential alternatives to the highly successful GBCAs, with the expectation that the use of an essential paramagnetic metal ion may avoid the issues possibly raised by the exogenous gadolinium.[29,30] Fe(III) complexes exhibit similar biodistribution and pharmacokinetic clearance profiles to the clinically utilized GBCAs. Moreover, the high thermodynamic stability, the expected low long-term toxicity, and the large relaxivity that Fe(III) complexes show at higher magnetic field, make them promising MRI CAs.

Compared to Gd(III) and Mn(II) complexes, the theory of water proton relaxation for Fe(III) complexes, has not been as thoroughly studied. However, papers reporting novel investigations about this class of compounds as MRI CAs are growing every year.[31–38]

The Fe(III) ion is endowed with strong Lewis acid characteristics due to its small ionic radius and high charge. Typically, Fe(III) complexes exhibit coordination numbers of six or seven. Those investigated as MRI probes either lack water ligands or contain a single inner-sphere water molecule.[39] The design of these probes has to deal with the non-banal aqueous solution chemistry of iron complexes with inner-sphere waters. For instance, these complexes may encounter ligand deprotonation at neutral pH leading to dimeric species with μ-oxo bridges.[30]

Iron complexes have two primary oxidation states, Fe(II) and Fe(III), with various spin states. In MRI CAs, high-spin Fe(III) complexes are needed as they yield 5 unpaired electrons in a stable, long-lived symmetrical electronic state. The spin state is influenced by the geometry of the complex and the nature of the donor groups. Stabilizing Fe(III) in the biological environment is crucial as is guarantees the efficacy of MRI *in vivo*. Extracellular agents should have a negative Fe(III)/Fe(II) redox potential (< 0.1 V or > 0.9 V vs. NHE) to prevent undesired redox cycle, possibly leading to Fenton reactions.[40]

Since the research in this topic is increasing in the last years, Fe(III) complexes have a promising future in MRI applications, and may become attractive in diagnosis and therapy.[29]

1.1.2.4 Responsive MRI contrast agents

MRI CAs primarily behave as static tracer agents that vary in concentration in different organs during imaging, but without any deliberate alteration of their physicochemical properties. Alternatively, MRI CAs can be employed to detect specific biological processes or pathologies by taking advantage of their changes in relaxivity or chemical exchange.[41] Within the physiological microenvironment, various features such as ion flux, pH, enzymatic activity, redox potential, and temperature can undergo alterations in disease processes.[8] Responsive

MRI CAs are designed to exhibit changes in relaxivity or in CEST effect in response to specific stimuli in their immediate microenvironment, leading to detectable changes in MRI signal.[42] However, the quantitative detection of a specific biomarker using responsive MRI CAs during practical biomedical applications is a substantial challenge.[41] This is due to the dependence of the MR signal amplitude on the concentration of the agent. Then, the use of another imaging technique to assess the concentration of the MRI CA, in a specific region of interest at a specific time point, can be the solution to overcome this issue. For example, positron emission tomography (PET) can be used in this context, by the development of both dual probes suitable for MRI and PET or also the use of co-agents endowed with the same pharmacokinetics injected simultaneously.[43,44]

Chapter 2

Towards new concepts in the design of improved Gd-based MRI contrast agents

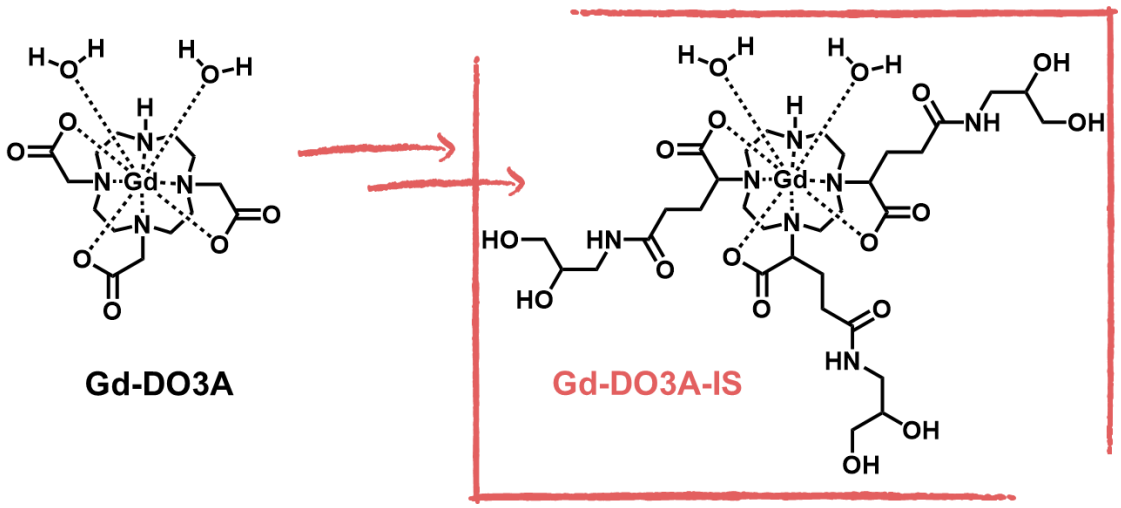

2.1 Introduction

Most of clinically used GBCAs were design to have only a single coordinated water molecule (q = 1) directly coordinated to the paramagnetic metal ion. This choice is driven by the early discovery that complexes formed with octa-dentate ligands offer high stability and minimize the *in vivo* release of Gd^{3+} ions.[8] However, since it is known that the relaxivity of a GBCA increases as q increases, there is growing interest in developing systems containing two or three water molecules coordinated to the Gd^{3+} ion, while maintaining sufficient stability for *in vivo* applications.[45] In this context, the DO3A ligand is a promising system for the development of GBCAs with q = 2. Although in Gd-DO3A the metal coordinates two water molecules, it was demonstrated that in biological fluids they can be displaced by bidentate anions such as phosphate, carbonate and carboxylate moieties.[46] This replacement of coordinated water molecules with endogenous anions, that are often present on the surface of proteins, leads to a decrease in relaxivity of the MRI CA *in vivo*.[47]

In this context, the structure of Gd-DO3A (Chart 2.1) was modified in order to investigate the possible overcoming of the described drawbacks.

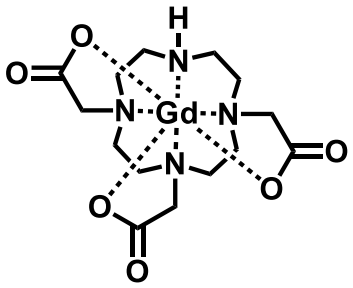

Chart 2.1. Chemical structure of Gd-DO3A.

Inspired by the recently reported high relaxivity agent Gadopiclenol[48] (based on the q = 2 system Gd-PCTA), Gd-DO3A-IS (Scheme 2.1) was designed starting from the structure of the macrocyclic Gd-DO3A. The introduction of several hydroxyl moieties on the outer sphere of the Gd-DO3A structure were expected to limit the accessibility of bidentate anions into the inner coordination sphere as well as to enhance the contribution to relaxivity from water molecules arising from of the second coordination sphere.

2.2 Results

2.2.1 Synthesis of Gd-DO3A-IS

The synthetic pathway to obtain the new complex Gd-DO3A-IS is shown in Scheme 2.1. The synthesis, performed by coworkers in our laboratory, is not treated in detail, as it is not the objective of this chapter. The Gd complex was made available for this study.

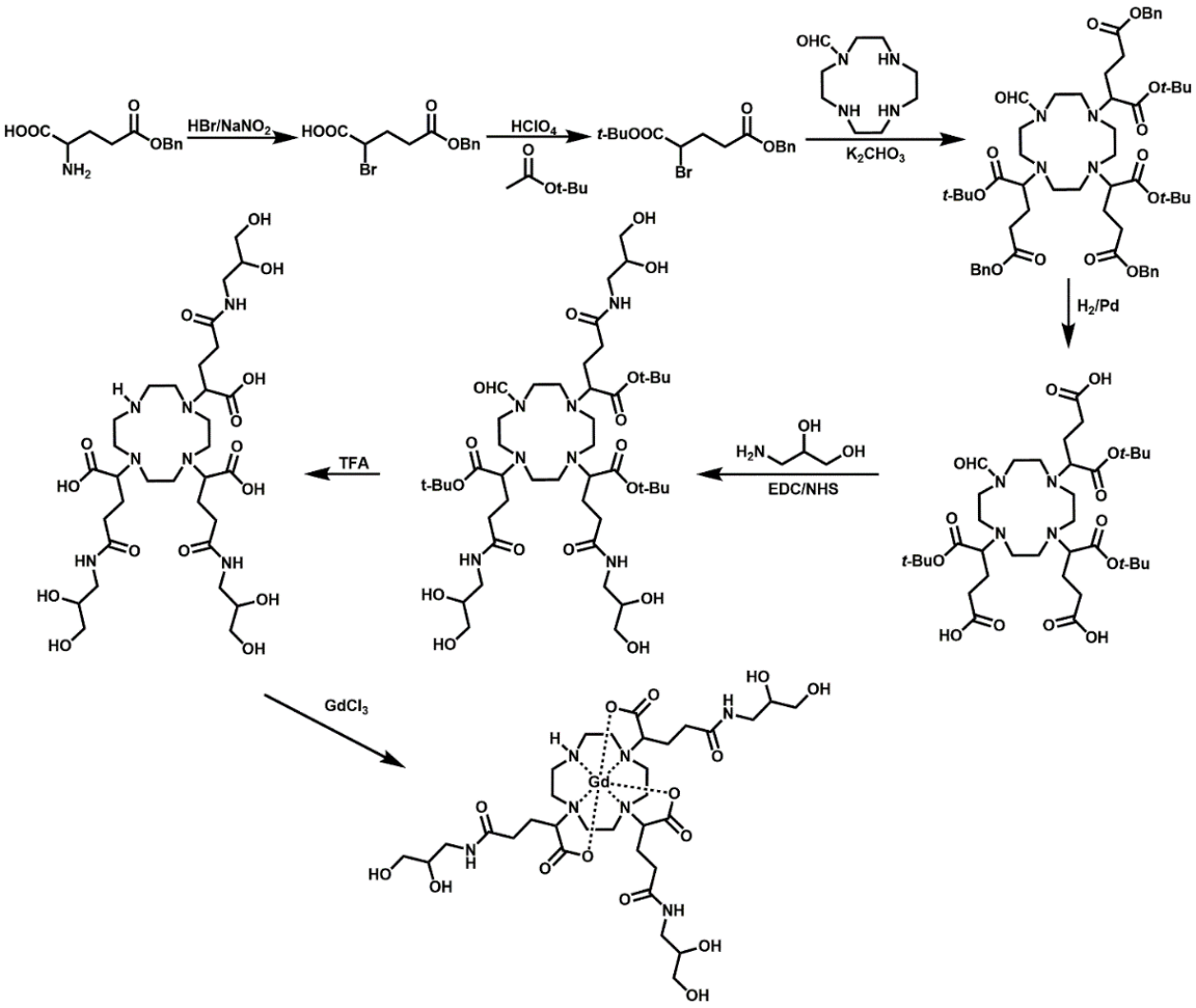

Scheme 2.1. Synthesis of the Gd-DO3A-IS.

2.2.2 *In vitro* relaxometric investigations

Relaxivity values (r_1) of Gd-DO3A and Gd-DO3A-IS as a function of pH, measured in water at 21.5 MHz and 298 K are shown in Figure 2.1. The pH dependence of Gd-DO3A-IS relaxivity recalls the one of the parent Gd-DO3A. The r_1 values remained almost constant in the range of pH 6 - 9.5, while significantly decreased above pH 9.5 for both complexes.

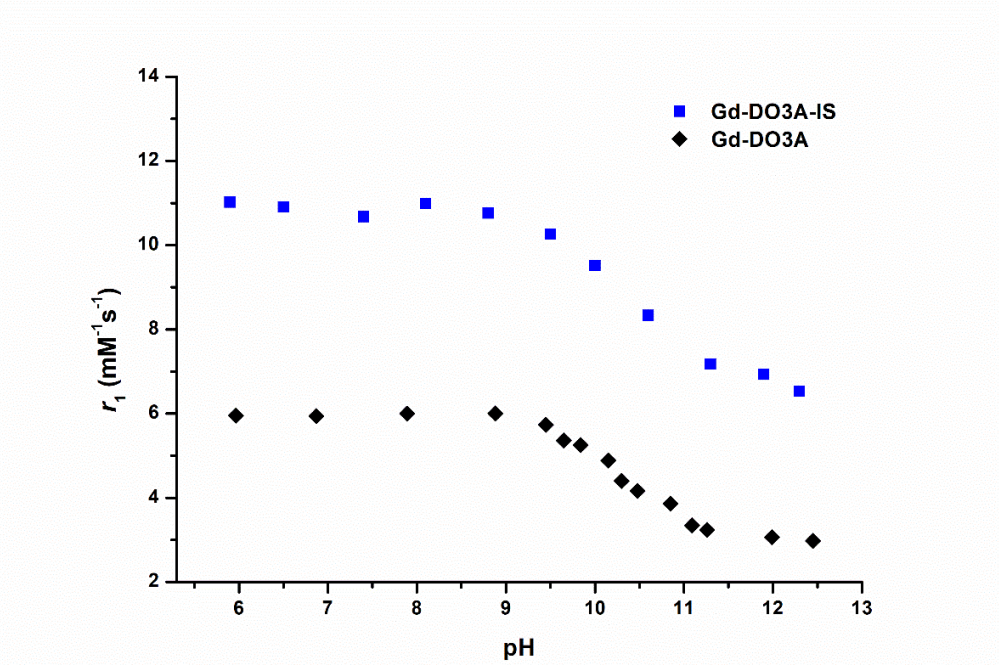

Figure 2.1. Relaxivity values (r_1) of Gd-DO3A-IS (blue squares) and Gd-DO3A (black diamonds) as a function of pH. 21.5 MHz, 298 K. Data measured at [Gd^{3+}] = 1 mM.

The r_1 relaxivity values of Gd-DO3A and Gd-DO3A-IS, measured at 21.5 MHz, 298 K and pH = 7.4 in water, iSBF (ionic simulated body fluid) and human serum are reported in Table 2.1. iSBF is a buffer containing all the ions normally present in serum but lacking proteins and it is very useful to investigate compounds interacting with salts.[49]

Table 2.1. Relaxivity values of Gd-DO3A and Gd-DO3A-IS measured at 21.5 MHz, 298 K and pH 7.4 in water, iSBF and human serum. Data measured at [Gd^{3+}] = 1 mM.

	r_1 (mM^{-1} s^{-1})		
	Water	**iSBF**	**H. Serum**
Gd-DO3A	**6.0**	**4.4**	**6.6**
Gd-DO3A-IS	**12.1**	**8.3**	**10.3**

To get more insight into the relaxation enhancement properties of the new Gd-complex, in Figure 2.2 the relaxivities of Gd-DO3A and Gd-DO3A-IS are compared with those of previously reported q = 2 Gd-complexes as a function of their molecular weight.[50] Gd-DO3A-IS relaxivity appears at the expected position, well along the straight line obtained by plotting the relaxivity of known Gd(III) complexes with q = 2 versus their molecular weight.

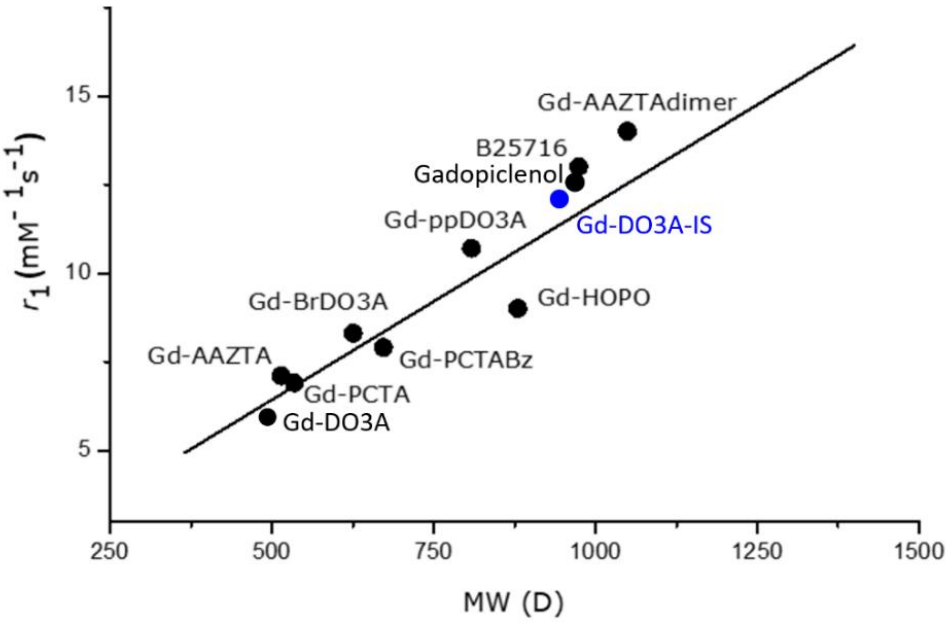

Figure 2.2. Molecular weight (MW) dependence of the Gd-DO3A-IS relaxivity (21.5 MHz, 298 K) compared with typical Gd complexes with two inner-sphere water molecules.[50] For Gadopiclenol: 21.5 MHz, 310 K.[48]

The kinetic parameters governing the water exchange process can be conveniently determined by measuring, via NMR spectroscopy, the transversal relaxation rate (R_2) of the ^{17}O nucleus of $H_2{}^{17}O$ at different temperatures, in the presence of the paramagnetic complexes.[51] In Figure 2.3, the ^{17}O-R_2 vs. T profile of Gd-DO3A-IS is compared with that of Gd-DO3A.

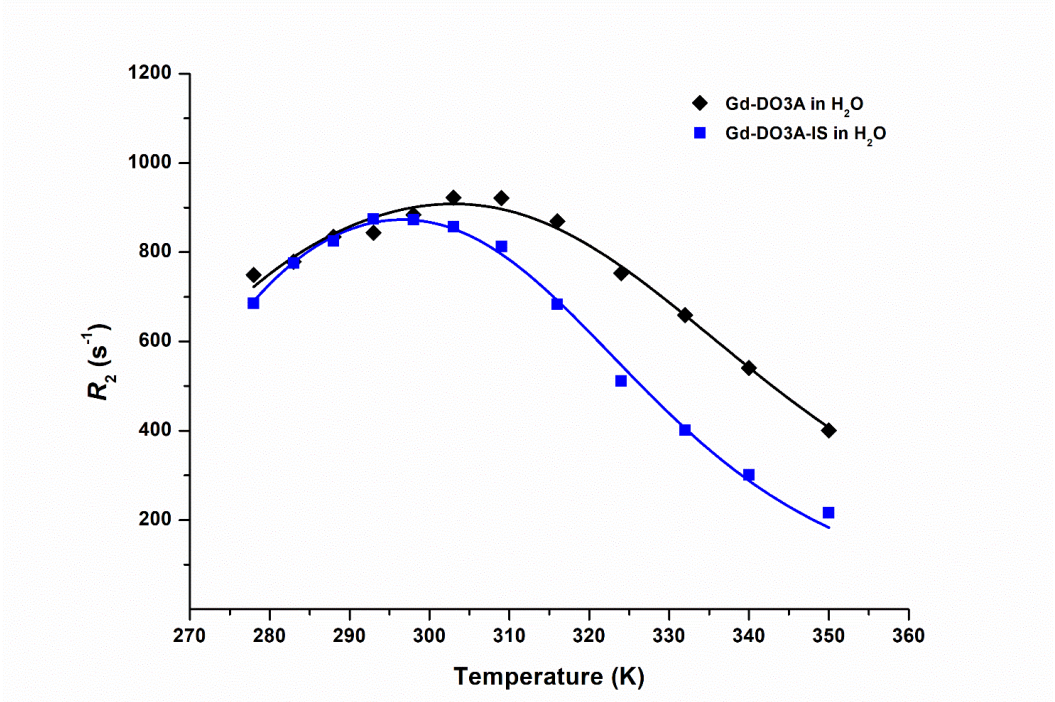

Figure 2.3. Comparison between the temperature dependence of the water ^{17}O transverse relaxation rate (R_2) of aqueous solutions of Gd-DO3A-IS (blue squares) and Gd-DO3A (black diamonds), at 14.1 T and pH = 7.4. Data normalized at 20 mM.

The investigated complex showed transverse relaxation rate values consistent with the presence of two inner sphere water molecules, analogously to the parent Gd-DO3A. The analysis of the observed profiles, using the modified Swift-Connick equations,[52] yielded an exchange lifetime (τ_M) value of 99.8 ns (see Table 2.2). Compared to the value obtained for the parent Gd-DO3A (τ_M = 160 ns), the value obtained for Gd-DO3A-IS showed a reduction of ca. 40%. A shortening in the exchange lifetime of the coordinated water molecules is a favorable characteristic for obtaining GBCAs with high relaxivities.

To investigate the interaction of Gd-DO3A-IS in the presence of endogenous anions, the transverse relaxation rate was measured in iSBF, to simulate the physiological inorganic environment. Figure 2.4 reports the comparison of ^{17}O-R_2 vs. T profiles relative to Gd-DO3A-IS in water and in iSBF.

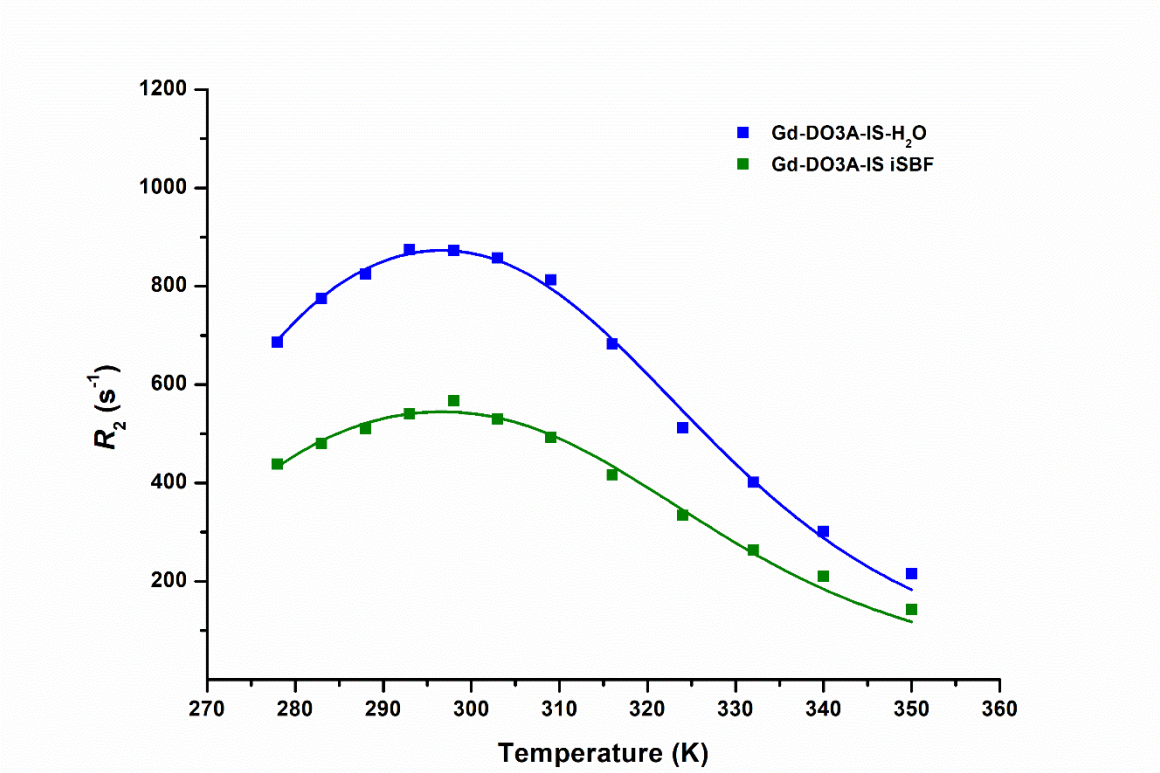

Figure 2.4. Comparison between the temperature dependence of the water ^{17}O transverse relaxation rate (R_2) of Gd-DO3A-IS solutions in pure water (blue squares) and in iSBF (green squares), at 14.1 T and pH = 7.4. Data normalized at 20 mM.

The experiment in iSBF yelded R_2 values halved with respect to those measured in water, to indicate a reduction in the hydration of the complex. In fact, in iSBF, the fitting of the experimental data afforded a q value of 1, while maintaining the same value of exchange lifetime τ_M = 99.8 ns (see Table 2.3).

More information about the determinants of the observed relaxivity was obtained recording the $1/T_1$ NMRD profiles over an extended range of magnetic field strengths (0.01 - 80 MHz as proton Larmor Frequency). The NMRD profiles, measured in water at neutral pH and 298 K, for Gd-DO3A-IS and Gd-DO3A are shown in Figure 2.5.

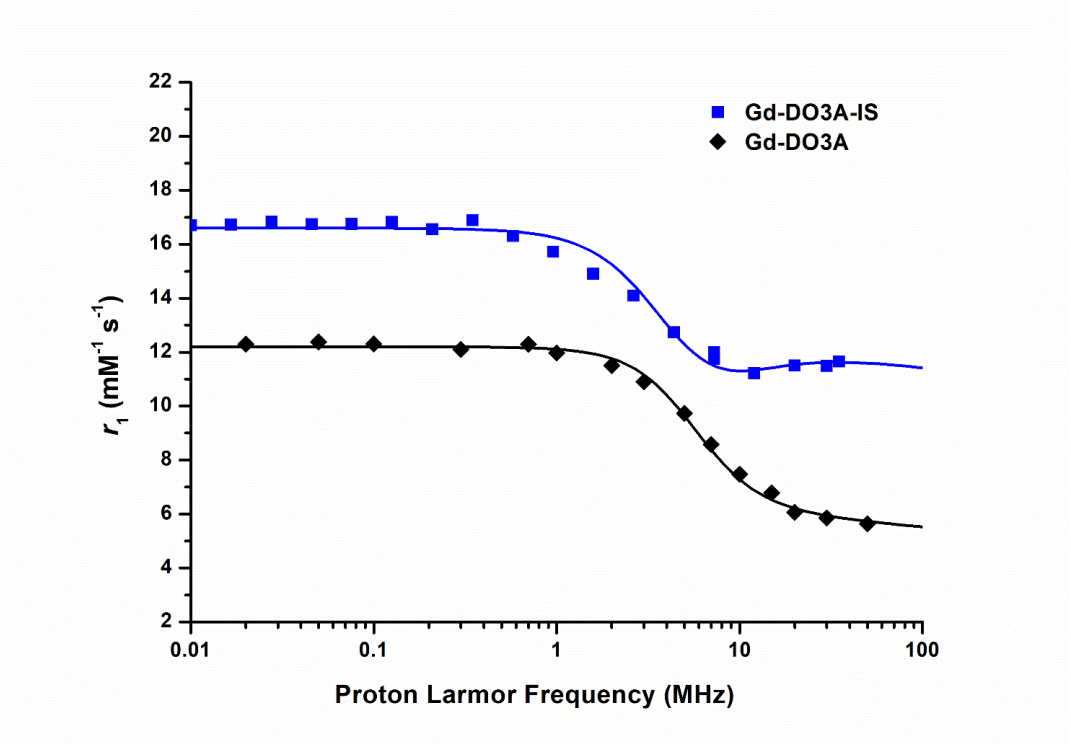

Figure 2.5. NMRD profiles from 0.01 to 80 MHz of 1 mM aqueous solutions of Gd-DO3A-IS (blue squares) and Gd-DO3A (black diamonds) at pH = 7.4 and 298 K.

The experimental data were fitted using the Solomon Bloembergen Morgan theory to extract the relevant relaxometric parameters (Δ^2, τ_V and τ_R) reported in Table 2.2. In the fitting procedure, the values of τ_M for the two derivatives were kept fixed to the values determined by the ^{17}O-R_2 vs. T experiment.

Table 2.2. Relaxation parameters of the Gd-DO3A-IS and Gd-DO3A complexes as derived from fitting of ^{17}O-R_2 vs. T data in Figure 2.3 and NMRD profiles in Figure 2.5 in water, at neutral pH.

	Δ^2 (10^{19} s^{-2}) [a]	τ_V (ps) [b]	τ_R (ps) [c]	τ_M (ns) [d]	q [e]
Gd-DO3A	**2.9 ± 0.22**	**20.6 ± 2.1**	**55.9 ± 1.5**	**160 ± 5.1**	**2**
Gd-DO3A-IS	**2.8 ± 0.15**	**28.7 ± 1.8**	**157 ± 3.4**	**99.8 ± 1.1**	**2**

[a] Squared mean transient zero-field splitting (ZFS) energy as obtained from fitting of NMRD profiles. [b] Correlation time for the collision-related modulation of the ZFS Hamiltonian as obtained from fitting of NMRD profiles. [c] Reorientational correlation time as obtained from fitting of NMRD profiles. [d] Exchange lifetime of the coordinated water molecules as obtained from fitting of ^{17}O-R_2 vs. T data. [e] Number of inner sphere water molecules as obtained from fitting of ^{17}O-R_2 vs.T data.

The τ_R value obtained for Gd-DO3A-IS was 157 ps, which is in line with what expected on the basis of the increased molecular weight if compared to Gd-DO3A.
In figure 2.6 the NMRD profile Gd-DO3A-IS in water is compared with those measured in human serum and in iSBF. The corresponding parameters derived from the fitting of these data are reported in Table 2.3.

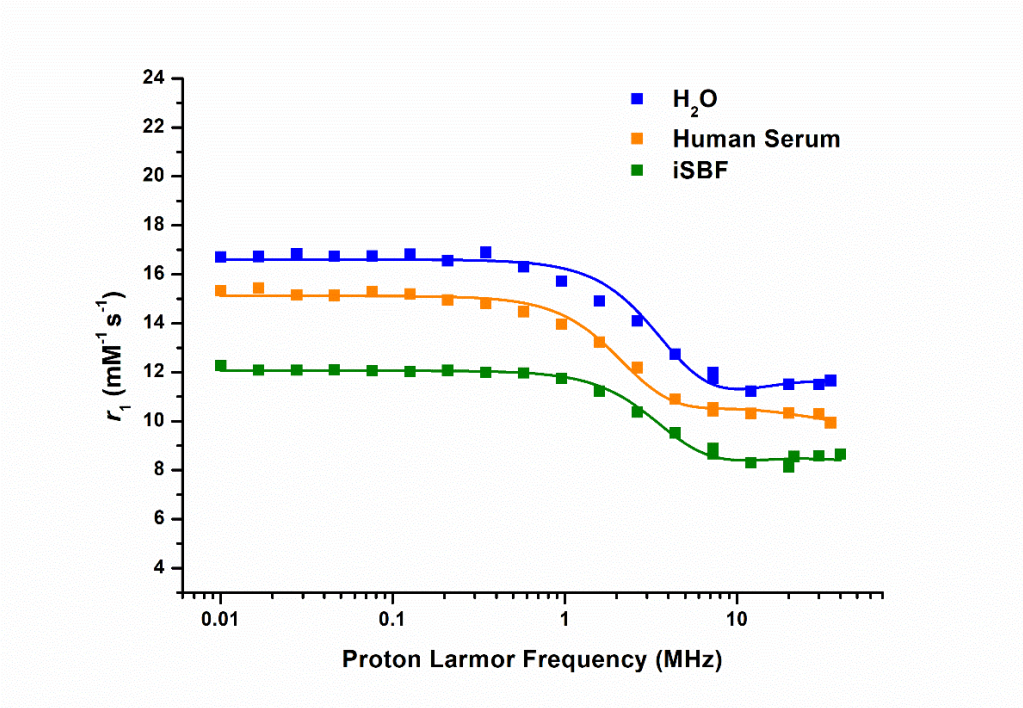

Figure 2.6. NMRD profiles of Gd-DO3A-IS in water (blue), human serum (orange) and iSBF (green) at neutral pH and 298 K.

Table 2.3. Relaxation parameters of the Gd-DO3A-IS complex as derived from fitting of ^{17}O-R_2 vs. T data in Figure 2.4 and NMRD profiles in water, iSBF and human serum in Figure 2.6.

	medium	Δ^2 (10^{19} s^{-2}) [a]	τ_V (ps) [b]	τ_R (ps) [c]	τ_M (ns) [d]	q [e]
Gd-DO3A-IS	Water	2.8 ± 0.15	28.7 ± 1.8	157 ± 3.4	99.8 ± 1.1	2
	iSBF	2.7 ± 0.33	29.1 ± 2.3	168 ± 6.1		1
	H. serum	0.9 ± 0.11	49.2 ± 4.1	256 ± 5.2		1

[a] Squared mean transient zero-field splitting (ZFS) energy as obtained from fitting of NMRD profiles. [b] Correlation time for the collision-related modulation of the ZFS Hamiltonian as obtained from fitting of NMRD profiles. [c] Reorientational correlation time as obtained from fitting of NMRD profiles. [d] Exchange lifetime of the coordinated water molecules as obtained from fitting of ^{17}O-R_2 vs. T data. [e] Number of inner sphere water molecules as obtained from fitting of ^{17}O-R_2 vs. T data.

As anticipated from the ^{17}O-R_2 vs. T experiment, when passing from water to iSBF and to human serum, a decrease in the inner sphere water molecules (q) was observed for Gd-DO3A-IS, with the best fitting obtained with q = 1.

The increase in τ_R observed for Gd-DO3A-IS in serum, with respect to pure water, is likely associated to the increase in viscosity or to the occurrence of a weak interaction with serum proteins. To investigate a possible interaction with human serum albumin (HSA), the most abundant protein in serum, a proton relaxation enhancement (PRE) titration was done with both complexes by measuring the variation in the longitudinal relaxation rate (R_1) of the paramagnetic guest for increasing concentrations of the protein (Figure 2.7). Both Gd-DO3A and Gd-DO3A-IS did not show any remarkable interaction with HSA. The observed linear enhancement prevented to fit the experimental data with univocal values, but it suggests that the formation of strong macromolecular adducts between these complexes and albumin can be ruled out.

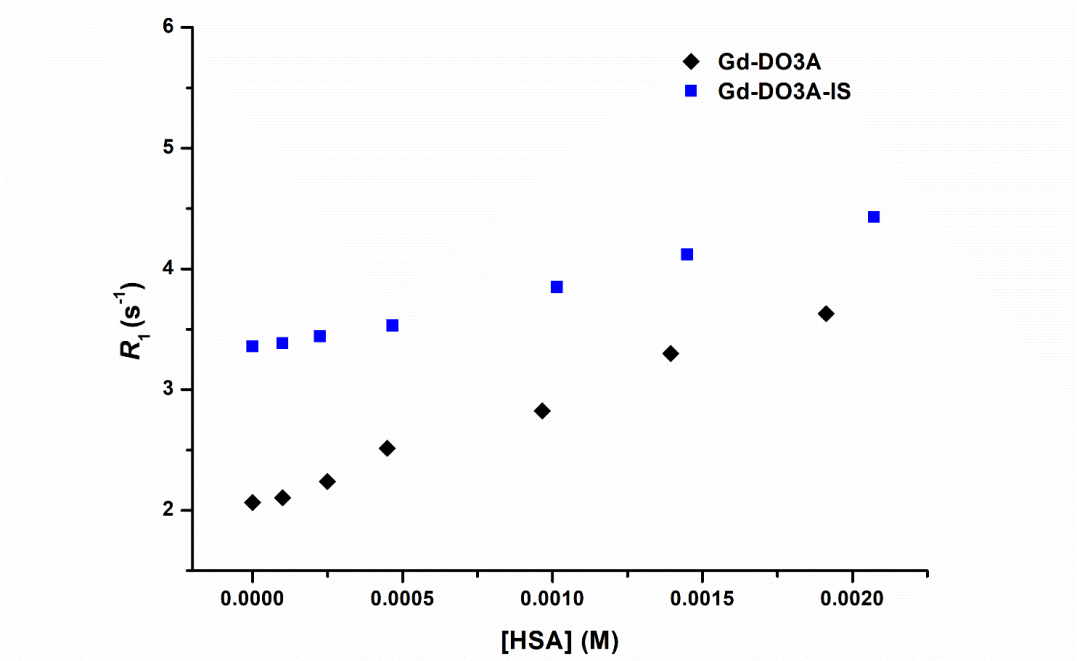

Figure 2.7. Observed relaxation rate of 0.3 mM Gd-DO3A (black diamonds) and Gd-DO3A-IS (blue squares) with increasing concentration of HSA. Samples measured in PBS at 21.5 MHz and 298 K.

The next step was testing Gd-DO3A-IS for its interaction with phosphate (Na_2HPO_4), carbonate ($NaHCO_3$), citrate and lactate by measuring the observed relaxation rates of 1 mM solutions of the Gd-complexes as a function of the concentrations of anions (Figure 2.8).

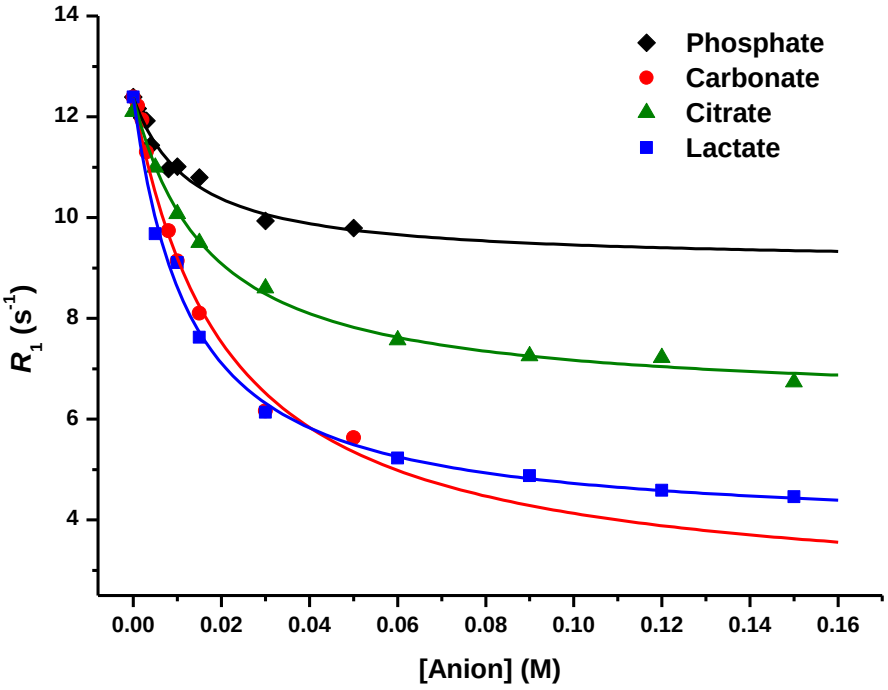

Figure 2.8. Observed relaxation rate of 1 mM Gd-DO3A-IS with increasing concentration of phosphate (black diamonds), carbonate (red circles), citrate (green triangles) and lactate (blue squares). Samples measured in PBS at 21.5 MHz and 298 K.

Experimental data were fitted to obtain the binding parameters collected in Table 2.4 and compared with the previously reported data obtained for Gd-DO3A.

Table 2.4. Anion binding parameters obtained from fitting of data reported in Figure 2.8, compared with previously reported Gd-DO3A data.

	Gd-DO3A		Gd-DO3A-IS	
	K_a (M^{-1})	$r_1^{Gd\text{-}anion}$ (mM^{-1} s^{-1})	K_a (M^{-1})	$r_1^{Gd\text{-}anion}$ (mM^{-1} s^{-1})
Phosphate	100 ± 20	5.3 ± 0.1	82 ± 14	8.7 ± 0.2
Carbonate	47 ± 9	1.5 ± 0.4	49 ± 7	2.0 ± 0.7
Citrate	42 ± 6	3.7 ± 0.08	52 ± 4	5.9 ± 0.1
Lactate	120 ± 7	2.5 ± 0.04	81 ± 7	3.3 ± 0.2

The parameters obtained for Gd-DO3A-IS, showed, with respect to Gd-DO3A, a slight decrease in the binding affinity in the case of phosphate and lactate binding, whereas binding affinity toward carbonate and citrate was maintained to a similar extent. The values of relaxivity obtained for the Gd-complex/anion adducts suggest that, in the case of both Gd-DO3A-IS and Gd-DO3A, the addition of phosphate leads to the displacement of only one of the two coordinated water molecules. Contrarily, the addition of carbonate and lactate reduces the inner sphere hydration of the Gd-complexes to $q = 0$, as expected on the basis of bidentate chelation.

Gd-DO3A-IS was then tested for its kinetic stability (Figure 2.9).

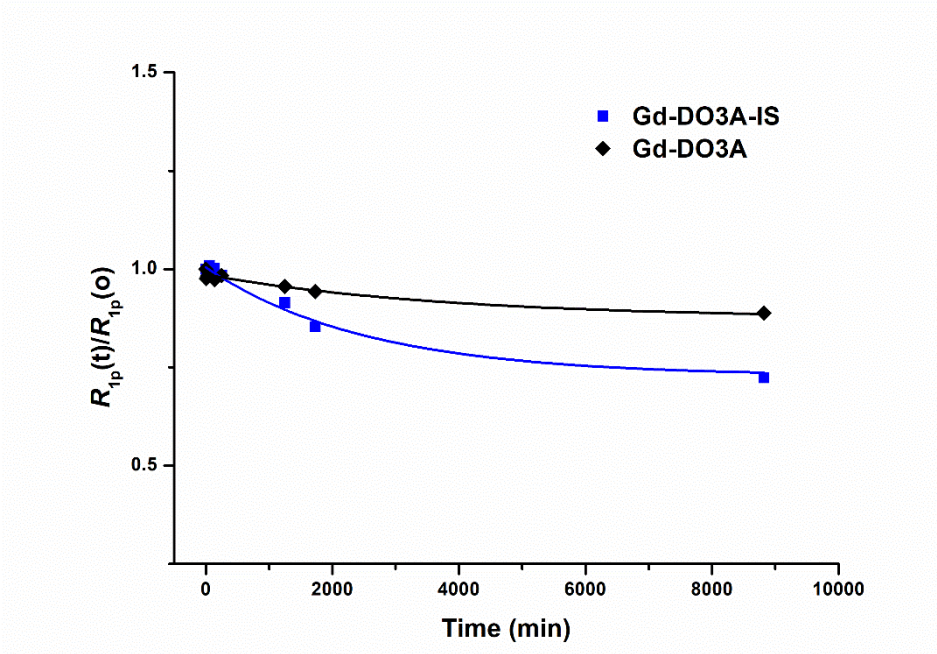

Figure 2.9. Zinc transmetallation as modelled by the change in $R_{1p}(t)/R_{1p}(0)$ (observed paramagnetic relaxation rate at a time point divided by the initial measured value in the absence of zinc) over time for the two Gd-complexes kept at 310 K in the presence of 1 eq. of $ZnCl_2$. Data measured at 21.5 MHz, 298 K.

The rate of transmetallation of the agent was monitored by measuring the relaxation rate in the presence of 1 equivalent of zinc chloride in PBS, analogously as previously reported for other Gd-complexes.[53] The method relies on the fact that, upon transmetallation between Zn^{2+} and Gd^{3+} ions, the released Gd^{3+} ions are precipitated as insoluble Gd-phosphate that, being a solid, does not contribute to the observed relaxation of water protons. By fitting the experimental data it is possible to extrapolate the value of $t_{0.8}$ which is the time for R_1 to reach 80% of its initial value. However, in this condition the relaxivity of both complexes is influenced by the presence of phosphate ions present in solution and a decrease in R_1 is expected. Although it is not possible to compare the two complexes due to the different affinity with phosphate, the kinetic inertness of Gd-DO3A-IS towards transmetallation with Zn ($t_{0.8}$ = 3500 min) showed to be much higher than clinically approved linear MRI CAs (i.e., for Gd-DTPA, $t_{0.8}$ = 260 min)[8]. It is worth to note that in the absence of phosphate the obtained value could be higher.

2.2.3 *In vivo* MRI studies

To test its *in vivo* efficiency as MRI CA, imaging experiments with Gd-DO3A-IS were performed and compared to Gd-HPDO3A (ProHance, Bracco), a macrocyclic GBCA routinely used in clinics. The complex was tested in murine models bearing a TS/A mouse mammary adenocarcinoma to evaluate both its efficiency as MRI contrast enhancer and its *in vivo* biodistribution. Figure 2.10 shows representative MRI images of mice acquired pre- and post-CA injection, after 10 min and 60 min.

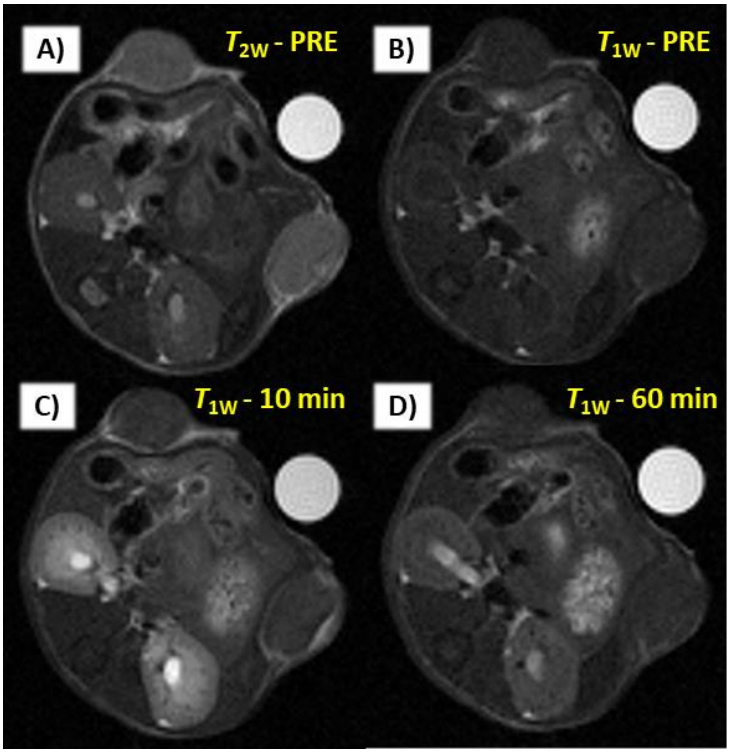

Figure 2.10 A) Axial high resolution T_2-weighted MR image showing tumours, spleen and kidneys; **B)** T_1-weighted MSME MR image (pre-contrast); **C)** T_1-weighted MSME MR image post i.v. injection of Gd-DO3A-IS (0.05 mmol/kg) at t = 10 min and **D)** post t = 60 min. Images were acquired on a 7 T scanner.

The signal enhancement percentage (SE%) over time in tumor, liver and kidneys is plotted in Figure 2.11. The initial signal enhancement of Gd-DO3A-IS was markedly higher than the one of Gd-HPDO3A, in all investigated organs. Notably, in tumors the signal of Gd-DO3A-IS remained relatively high (10 - 15%) over one hour of acquisitions, while with Gd-HPDO3A the signal dropped to less than 5% over the same time period. Gd-DO3A-IS displayed significantly higher uptake in the kidneys than in the liver, indicating the likelihood of renal excretion as found for the low molecular weight, highly hydrophilic currently used MRI contrast agents.

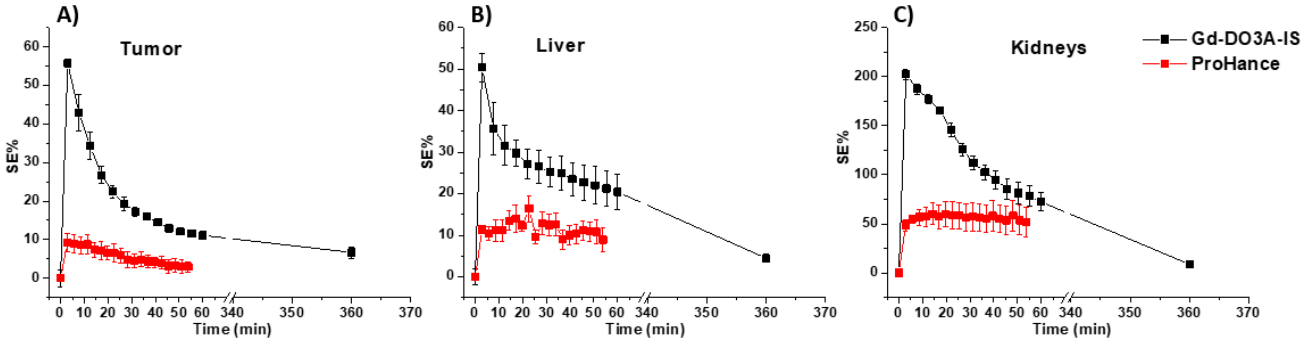

Figure 2.11. Percentage of MR signal enhancement in tumor tissue **(A)**, liver **(B)** and kidneys **(C)** obtained for Gd-DO3A-IS (black squares) and Gd-HPDO3A (red squares). Data are the mean + SD from three independent experiments (n = 3) for each curve.

2.3 Discussion

The pH dependence of relaxivity shown in Figure 2.1 for the new complex Gd-DO3A-IS recalls that of the parent compound Gd-DO3A. The r_1 values remain almost constant in the pH range 6-9.5, while from pH 9.5-10, the hydrolysis of the coordinated water molecules takes place with a consequent decrease in relaxivity. Such behavior likely involves the coordination of OH^- groups present in basic conditions at the positions previously occupied by two water molecules. In Figure 2.2 the relaxivity (in water at neutral pH) of Gd-DO3A-IS is compared with those of previously reported Gd-complexes with $q = 2$. It can be noticed that the relaxivity of the new complex is at the position expected in the plot of relaxivity as a function of molecular weight.

The study of the temperature dependence of water ^{17}O transverse relaxivity allowed to determine, for Gd-DO3A-IS, a reduction in the exchange lifetime of the coordinated water molecules: the insertion of the quite bulky pendant groups in Gd-DO3A-IS reduces the exchange lifetime of the coordinated water molecules of ca. 40% with respect to the parent Gd-DO3A.

The measurement of the water proton relaxation rate over an extended range of magnetic field strengths (NMRD profile) is a complementary method for the complete characterization of a paramagnetic complex. The resulting plot of relaxivity versus proton Larmor frequency is reported in Figure 2.5 and Figure 2.6. The inner and outer sphere contributions are determined by several structural and dynamic parameters (Δ^2, τ_V, τ_M, τ_R, q, r, a, D). The possibility of fixing the values of some of the involved parameters during the fitting makes the determination of

the other ones more accurate. Among the relaxometric parameters resulting from the fitting of NMRD profiles collected in Table 2.2 and Table 2.3, the reorientational correlation time (τ_R) is the most accurately determined. The molecular reorientational correlation time tends to dominate the overall correlation time of low molecular weight Gd(III) chelates, particularly in the high field region, and therefore represents a key parameter in governing their relaxivity. The effect of the increase of τ_R on the shape and amplitude of the NMRD profiles is well-established and many attempts for the optimization of the relaxivity were primarily focused at slowing down the molecular reorientational motion by increasing the size of the complexes. The increased relaxivity of Gd-DO3A-IS in water with respect to Gd-DO3A is in fact ascribable to the three times increase in τ_R (Table 2.2) associated to its increased molecular weight (Figure 2.2).

Some interesting considerations can be drawn when comparing the NMRD profile of Gd-DO3A-IS in water with those measured in human serum and in iSBF (a medium containing all the ions present in serum but lacking proteins) (Figure 2.6). An increase in τ_R, although limited, was observed when NMRD profile was measured in human serum. The relatively slight increase observed for Gd-DO3A-IS can be likely associated to the increase in viscosity in serum, with respect to pure water, as well as the occurrence of a weak interaction with macromolecular serum components cannot be ruled out. A proton relaxation enhancement (PRE) titration of the complex with increasing amounts of HSA (the most abundant protein in serum) did not show any evidence of relevant binding interaction (Figure 2.3).

The fitting of NMRD profiles of Gd-DO3A-IS in human serum and in iSBF afforded a number of coordinated water molecules $q = 1$ for both media. The same result was obtained by fitting of the ^{17}O-R_2 vs. T experiment carried out in iSBF (Figure 2.4), which gave $q = 1$. This displacement of a coordinated water molecule is ascribable to the interaction with endogenous anions in the inner coordination sphere, as in the case of the parent compound Gd-DO3A, although the more encumbered substituents present in Gd-DO3A-IS were expected to shield the paramagnetic center from the entry of such endogenous species. A direct and quantitative evaluation of the affinity of Gd-DO3A-IS towards the principal endogenous anions was obtained through the specific titrations of the two Gd-complexes with phosphate, carbonate, citrate and lactate (Figure 2.8).

Inspection into values reported in Table 2.4 allows realizing that the introduction of the hydroxyl functionalities on the outer surface of Gd-DO3A did not afford the desired reduction in anion binding affinity. In fact, Gd-DO3A-IS showed a very slight decrease in binding affinity towards phosphate and lactate, with respect to Gd-DO3A, and the binding affinity toward carbonate and citrate was maintained to a similar extent. Looking at the values of relaxivity obtained for the Gd-complex/anion adducts it can be concluded that, as for the parent Gd-DO3A, the addition of phosphate leads to the displacement of only one of the two coordinated water molecules, whereas the addition of carbonate and lactate reduces the inner sphere hydration of the Gd-complexes to $q = 0$. It is likely in fact that phosphate coordinates the Gd(III) ion in a monodentate manner while carbonate and lactate have a bidentate chelation ability.

However, even though the affinity of the new Gd-DO3A derivative towards anions remains high, its relaxivity measured in serum (at 21.5 MHz and 298 K) is more than doubled (r_1 = 10.3 $mM^{-1} s^{-1}$) with respect to that of commercial q =1 clinically used contrast agents (r_1 = 4 - 5 $mM^{-1} s^{-1}$).

An important property for the use of new Gd-based complexes *in vivo* as MRI contrast agents is related to their thermodynamic and kinetic stability, which strictly affects their safeness. The evaluation of the thermodynamic stability was not object of this study, but the Gd complexes were tested for their kinetic inertness through an established relaxometric method in the presence of zinc chloride in phosphate buffer (Figure 2.9).[53] Although in the presence of phosphate a drop in R_1 was observed, as expected by the previous experiments, the kinetic inertness of Gd-DO3A-IS towards transmetallation with Zn showed to be much higher than clinically approved linear MRI CAs, with a $t_{0.8}$ of at least 3500 min.

Then, the efficiency of Gd-DO3A-IS as MR contrast agent was tested in a tumor murine model and compared to that of a q = 1 contrast agent (Gd-HPDO3A, ProHance – Bracco Imaging) currently used in the clinics. As shown in Figures 2.10 and 2.11, the initial signal enhancement is markedly higher upon the administration of Gd-DO3A-IS complex with respect to Gd-HPDO3A. After a partial rapid washout, an appreciable signal (ca. 15%) remains up to one hour after the injection. The initial contrast enhancement is even more of what one would expect on the basis of the respective relaxivities in serum. The relaxivity of the herein investigated complex is doubled with respect to the q = 1 commercial Gd-HPDO3A being respectively r_1 = 8.00 $mM^{-1} s^{-1}$ for Gd-DO3A-IS vs. r_1 = 3.5 $mM^{-1} s^{-1}$ for Gd-HPDO3A, in serum at 310 K). The observed behavior may likely reflect effects associated to the differences in the biodistribution of the two complexes.

2.4 Conclusion

In summary, although the hydroxyl containing moieties demonstrated to be not sufficient to prevent the access of endogenous anions in the inner sphere of the Gd(III) ion, the obtained results indicate that the observed relaxivity of the new complex Gd-DO3A-IS is markedly higher than the one observed for the parent Gd-DO3A. Moreover, the *in vivo* validation of the Gd-based probe demonstrated significantly higher enhancement properties as compared with Gd-HPDO3A in this murine tumor model, at half of the common clinical dose.

2.5 Experimental section

Chemicals were purchased from Sigma-Aldrich Co.

2.5.1 Synthesis

The ligands 1,4,7,10-tetrazacyclododecane-1,4,7-triacetic acid (DO3A) and 1,4,7,10-tetraazacyclododecane-1,4,7-triyl)tris(5-((2,3-dihydroxypropyl)amino)-5-oxopentanoic acid (DO3A-IS) were previously synthesized by coworkers in the same research group. Thus, in this this section the experimental details of the synthesis steps are not reported. The resulting Gd(III)-complexed products, Gd-DO3A and Gd-DO3A-IS (Chart 2.1 and Scheme 2.1, respectively) were made available for this study.

2.5.2 Relaxometric measurements

Observed longitudinal relaxation rate ($R_1^{obs} = 1/T_1^{obs}$) values were determined by inversion recovery at 21.5 MHz and 298 K using a Stelar SpinMaster spectrometer (Stelar s.r.l, Mede (PV), Italy). Temperature was controlled with a Stelar VTC-91 airflow heater and the temperature inside the probe checked with a calibrated RS PRO RS55-11 digital thermometer. Data were acquired using a recovery time ≥ 5 x T_1 and with 2 scans per data point. The absolute error in R_{1obs} measurements was less than 1%.

Gadolinium concentration of each solution was determined by the relaxometric preaviously reported method:[50] a solution containing equal volumes of the Gd(III)-complex solution and 37% HCl was mixed in a sealed vial and left overnight at 393 K. R_1^{obs} values of the acidic solution were determined and the total concentration of Gd^{3+} was evaluated on the basis of the following equation: $[Gd] = (R_1^{obs} - R_1^{d}) / r_{1p}^{Gd}$, where R_1^{d} is the diamagnetic contribution (0.5 s^{-1}) and r_{1p}^{Gd} the relaxivity of the Gd(III) ion in acidic conditions (13.5 $mM^{-1}\,s^{-1}$).

pH profiles were acquired by measuring the R_1^{obs} of aqueous solutions of the Gd(III)-complexes at increasing values of pH. pH was altered using NaOH 1 M and pH measurements were performed using an AS instruments pH meter equipped with a glass electrode.

NMRD profiles were obtained using a Stelar SmartTracer FFC NMR relaxometer from 0.01 to 10 MHz. Additional data in the 20 − 80 MHz frequency range were obtained with a High Field Relaxometer (Stelar) equipped with the HTS-110 3T Metrology cryogen-free superconducting magnet and a Bruker WP80 NMR electromagnet (21.5 – 80 MHz), both equipped with a Stelar VTC-91 for temperature control; the temperature inside the probe was checked with a calibrated RS PRO RS55-11 digital thermometer. Aqueous and human serum solutions of the complex were measured at 298 K. The NMRD profile data were fitted using the Solomon-Bloembergen-Morgan and Freed's models.

The analyses of the NMRD profiles collected in recent years for a series of structurally similar Gd(III) chelates allowed reliable estimates for some relaxation parameters. In particular, the value of q (number of coordinated water molecules) was assumed to be 2, as expected for DO3A derivatives and determined through ^{17}O-NMR vs. T experiment; r (the distance between the Gd(III) ion and the protons of the coordinated water molecules) was fixed at 3.1 Å; a (the distance between the Gd(III) ion and the outer sphere water proton nuclei) was set at 3.8 Å; D (the solute–solvent diffusion coefficient) was fixed at 2.24×10^{-5} $cm^2\,s^{-1}$. The values of the coordinated water exchange lifetime (τ_M) were fixed to those obtained from ^{17}O-NMR experiments.

O^{17}-R_2-NMR measurements were recorded at 14.1 T on a Bruker Avance 600 spectrometer at variable temperature, with a D_2O sealed capillary for sample locking inside the tube. The 20 mM Gd-complexes solutions were enriched with 1% of $H_2{}^{17}O$ (Cambridge Isotope). The width at half maximum ($\Delta\omega_{dia}$) of the $H_2{}^{17}O$ signal in pure water was measured over the investigated temperature range and subtracted from the width at half maximum ($\Delta\omega_{Gd}$) of the tested Gd-complexes solutions. Then, R_2 was calculated as follows: $R_2 = \pi[\Delta\omega_{Gd} - \Delta\omega_{dia}]$.

Transmetallation experiments were performed following the previously described procedure:[53] Gd complexes were dissolved in phosphate buffer (26 mM KH_2PO_4 and 41 mM Na_2HPO_4) at

pH 7. A $ZnCl_2$ solution (100 mM $ZnCl_2$ in H_2O) was added to give an equimolar Gd : Zn solution. The relaxation rate of the solution at 298 K and 21.5 MHz was measured. The NMR tubes were kept at 310 K at a moderate stirring between subsequent measurements over the course of 6 days. At each measurement, the ratio $R_{1p}(t)$ / $R_{1p}(t=0)$ was determined, were $R_{1p}(t=0)$ corresponds to the paramagnetic longitudinal relaxation rate of water protons at t=0, and $R_{1p}(t)$ is the paramagnetic longitudinal relaxation rate of water protons at each time measurement.

Anion binding interaction was determined by the measurement of the relaxation rate at 298 K and 21.5 MHz of solutions containing known concentrations of Gd(III)-complex and increasing concentrations of the given anion at pH 7. Solutions of NaH_2PO_4 (100 mM), $NaHCO_3$ (100 mM), $C_6H_5Na_3O_7$ (sodium citrate) (100 mM) and $C_3H_5NaO_3$ (sodium lactate) (100 mM) were prepared and added to Gd(III)-complex aqueous solutions of known concentrations, in order to reach increasing concentrations of anions (0-50 mM).

2.5.2 Cell preparation and animal handling

The tumour model was a breast cancer model obtained by inoculating TS/A mouse mammary adenocarcinoma cell line subcutaneously in six female BALB/C mice. TS/A cells, a BALB/c-derived mouse mammary carcinoma corresponding to stage IV of human breast cancer, were purchased from American Type Culture Collection (ATCC LGC Standards, Sesto San Giovanni, Italy). Cells were grown in RPMI-1640 medium supplemented with 10% fetal bovine serum, 1% glutamine, 100 IU/mL penicillin and 100 μg/mL streptomycin. Cells were seeded in 75-cm^2 flasks at density of *ca*. 4×10^4 cells/cm^2 in a humidified 5% CO_2 incubator at 310 K. At confluence, they were detached by adding 1 mL of Trypsin-EDTA solution (0.25 % (*w/v*) Trypsin-0.53 mM EDTA). Cells were negative for mycoplasma as tested by using MycoAlert™ Mycoplasma Detection Kit (Lonza Sales AG-EuroClone S.p.A., Milano, It). The day of inoculation, cells were collected and washed two times with PBS 1X, then $3x10^5$ cells were re-suspended in 100 μL serum-free medium and inoculated in animals with a syringe (needle 29G) on both flanks. BALB/c female mice (Charles River Laboratories Italia S.r.l., Calco, Italy) were maintained in the animal facility of the Molecular Biotechnology Center, University of Turin, under specific pathogen-free conditions. All animal studies were approved by the University Ethics Committee in accordance with the European Community Parliament and Council Directives of 24 November 1986 (86/609/EEC) and 22 September 2010 (2010/63/EU).

2.5.3 In vivo MRI studies

MR images were acquired 10 - 13 days after the tumor inoculation, with tumor dimensions in a range of 80 - 200 mm^3. For administration of the contrast agent, an intravenous catheter was inserted in the tail vein of the animal under anesthesia, before positioning inside the MR scanner. Animals were anaesthetized by intramuscular injection of a mixture of Tiletamine/Zolazepam (Zoletil 100, Virbac, Milan, Italy) 20 mg/kg and xylazine (Rompun; Bayer, Milan, Italy) 5 mg/kg and the breath rate was monitored by an air pillow placed below the animal (SA Instruments, Stony Brook, NY, USA). Mice were injected with the GBCA

(0.05 mmol/kg). MR images were acquired at 7.1 T on a Bruker Avance 300 spectrometer equipped with the Micro 2.5 microimaging probe at room temperature (R.T. = 21 °C).

^{1}H sequences (RARE T2-weighted) on each geometry was acquired on the animal to obtain a proper anatomical reference, with the following parameters: TR = 4000 ms, TE = 35 ms, RARE factor = 24, flip angle = 180°, number of averages = 2, FOV = 30 mm × 30 mm, slice thickness = 1 mm, matrix size 128 × 128, spatial resolution = 0.234 mm/pixel × 0.234 mm/pixel.

A series of T_1-weighted MSME scans were acquired before and after the intravenous administration (50 min) of the gadolinium complex in order to follow the kinetic of the contrast agent in the diseased mass, having the following parameters: TR = 221.714 ms, TE = 8 ms, number of averages = 6, FOV = 30 mm × 30 mm, slice thickness = 1 mm, matrix size 128 × 128, spatial resolution = 0.234 mm/pixel × 0.234 mm/pixel, acquisition time = 2:50 min.

A 5 mm NMR glass tube containing 0.5 mM of Gd-HPDO3A in water as reference was inserted close to the mouse body.

After the acquisition of the images, the T_1 contrast enhancement (S.E.%) was calculated as follows: $S.E.\% = [(S.I._{post} - S.I._{pre}) / S.I._{pre}] \times 100$, where $S.I._{post}$ and $S.I._{pre}$ are the signal intensities (both normalized by dividing for the external standard reference) post and pre the injection of both Gd-contrast agents.

Regions of Interest (ROIs) were manually drawn inside the reference standard sample, tumours, kidneys and different regions of the liver and S.E.% was calculated in all the ROI as reported above.

Chapter 3

Relaxation enhancement via weak and dynamic electrostatic/cation-π interactions with protonated groups on endogenous macromolecules

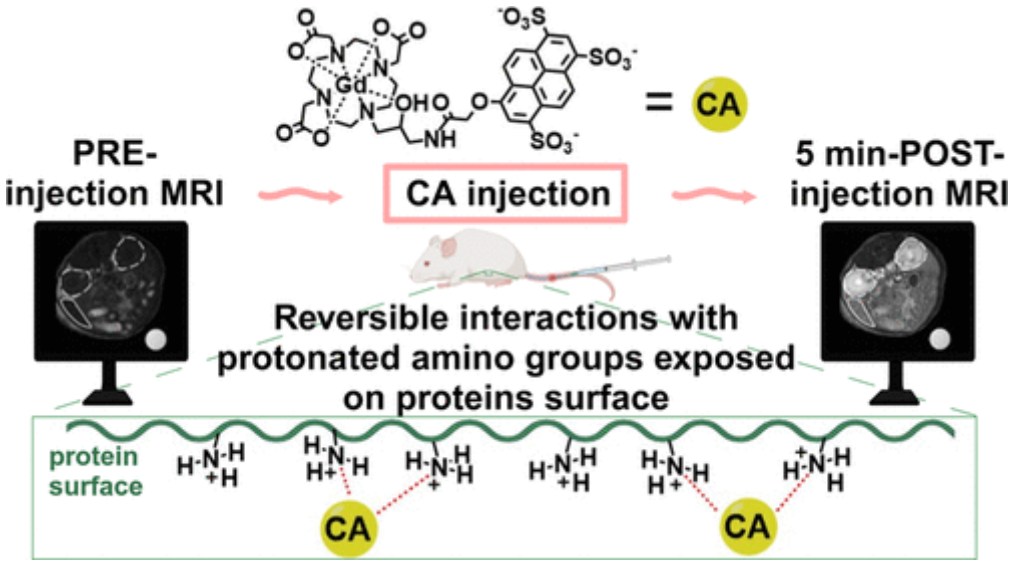

3.1 Introduction

The aim of this project is to seek for the generation of relaxation enhancement through the involvement of novel types of non-covalent interactions with endogenous systems. In this chapter, a novel approach involving the reversible set up of binding motifs with the abundant positively charged moieties exposed on the outer surface of endogenous proteins is described. Protonated groups on endogenous macromolecules provide a good source for the setup of electrostatic salt bridges or cation-π interactions. Indeed, cation-π interactions play a significant role in various biological systems, contributing to crucial processes such as generating robust wet adhesion and cohesion in humid or underwater environments.[54] They are primarily of electrostatic origin, resulting from the attractive forces between a positively charged cation and the negatively charged electron cloud of π systems (aromatic rings). The strength of these interactions stands out as stronger than typical hydrogen bonds.[55]

Human serum albumin (HSA) and γ-globulins are excellent examples of potential substrates for the set-up of cation-π interactions.[56,57] HSA contains a high number of positively charged NH_3^+ lysine residues, which can engage in cation-π interactions with aromatic functionalities.[58] γ-globulins, which have a high isoelectric point (pI), can also participate in cation-π interactions due to the presence of positively charged amino acid residues on their surface.[59,60]

Based on this premise, naturally occurring structural motifs that involve protonated nitrogen-containing chains appear as intriguing systems as they often come into close proximity with aromatic moieties, as evidenced by several crystallographic studies.[61,62] Also, it was reported that the strength of cation-π interactions is sufficient to stabilize the structure of small peptide-based drugs.[63] Therefore, macromolecules that expose NH_3^+ functionalities are potential sites for the formation of cation-π interactions. Notably, in aqueous media, the energy of these interactions is comparable to, or even stronger than, that observed in the case of ammonium-carboxylate salt bridges.[64] Such properties make these macromolecules promising candidates for fostering stable and robust interactions in biological environments.

In this context, a novel gadolinium-based contrast agent (GBCA) bearing on its surface the trisulfonated aromatic derivative of 8-hydroxypyrene-1,3,6-trisulfonic acid (HPTS, pyranine) was synthesized in our lab. The presence of a large π system is expected to be beneficial for the set-up of stronger cation-π interactions.

The relaxometric characterization of such compound, the investigation of its interaction with macromolecules exposing cationic amino groups on their surface, and the *in vivo* studies to test its efficiency as a potential MRI CA are described in this chapter.

3.2 Results

3.2.1 Synthesis of Gd-L1 and Eu-L1

The synthesis of Ln-L1, performed by coworkers in our laboratory, is shown in Scheme 3.1 (Ln = Gd or Eu).

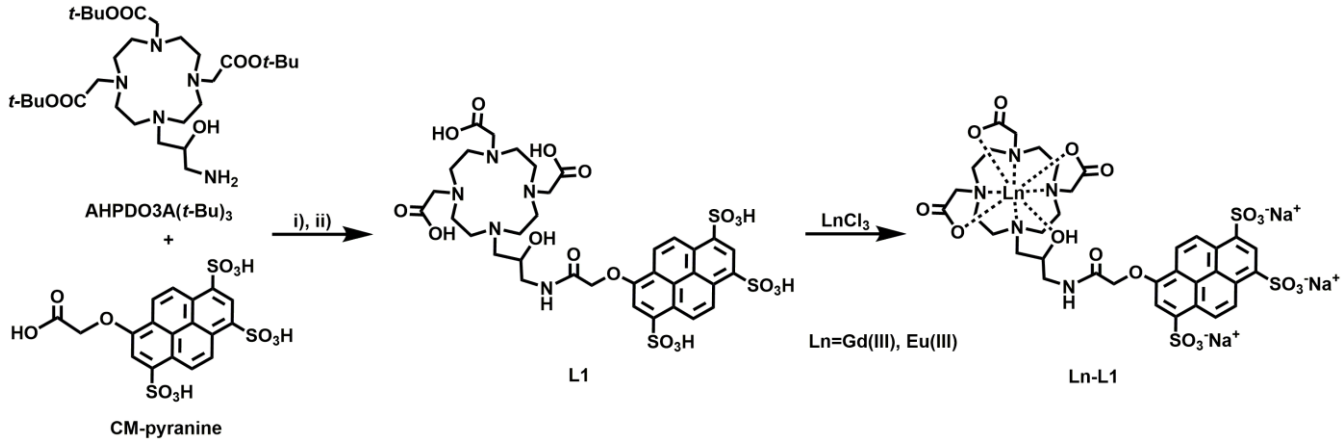

Scheme 3.1. Synthesis of the L1 ligand and its Ln(III) (Gd(III) or Eu(III)) complexes. Reagents and conditions: (i) HBTU, DMF, DIPEA (ii) TFA, DCM ¼ v/v.

The ligand L1 was obtained by coupling 8-O-carboxymethylpyranine (CM-pyranine) to amino functionalized AHPDO3A(*t*-Bu)$_3$ using HBTU (*o*-(Benzotriazol-1-yl)-*N*,*N*,*N*′,*N*′-tetramethyluroniumhexafluorophosphate) and DIPEA (*N*,*N*-Diisopropylethylamine) in DMF, followed by the deprotection of *t*-butyl esters in the presence of TFA (trifluoroacetic acid) with an overall yield of about 50%. The protected AHPDO3A(*t*-Bu)$_3$ ligand was synthesized as reported in the literature;[65] briefly, *N*-Cbz-2,3-epoxypropylamine was opened by the secondary amine of DO3A-(O-*t*-Bu)$_3$ and then the Cbz group was removed by Pd/C catalyzed hydrogenolysis. Conversely, CM-pyranine was prepared by alkylation of the commercially available HPTS with methyl bromoacetate in refluxing methanol. Then, the obtained methyl ester was quantitatively hydrolyzed with 2.4 M aqueous HCl at 90 °C. The final L1 ligand was purified by chromatography on an Amberchrom® resin with an ovaerall 46% yield. The corresponding Ln(III)-complexes (Ln(III) = Gd(III) or Eu(III)) were then prepared by mixing stoichiometric amounts of L1 and $LnCl_3$ at pH = 6.7 in water. Upon removal of the formed salts, Ln-L1 complexes were obtained at an excellent purity level. The ^{1}H NMR spectrum (Figure 3.7A) of Eu-L1 showed the presence of the two expected diastereoisomers, namely TSAP (twisted square anti prismatic) and SAP (square anti prismatic) in the ratio of 3:2, respectively.[66–68]

3.2.2 *In vitro* relaxometric investigations

The measurement of the relaxation rates, R_1, of a 1 mM aqueous solution of Gd-L1 as a function of pH (at 21.5 MHz and 298 K) yielded a relaxivity value of 7.1 mM^{-1} s^{-1} which remained almost constant upon increasing the pH up to 9-10 showing a slight decrease at higher pH values (Figure 3.1A). Notably, this finding indicates a substantial difference in respect to the pH dependence of the relaxivity of the parent complex Gd-HPDO3A that shows an increase at basic pH due to the mobilization of the coordinated hydroxyl proton.[51]

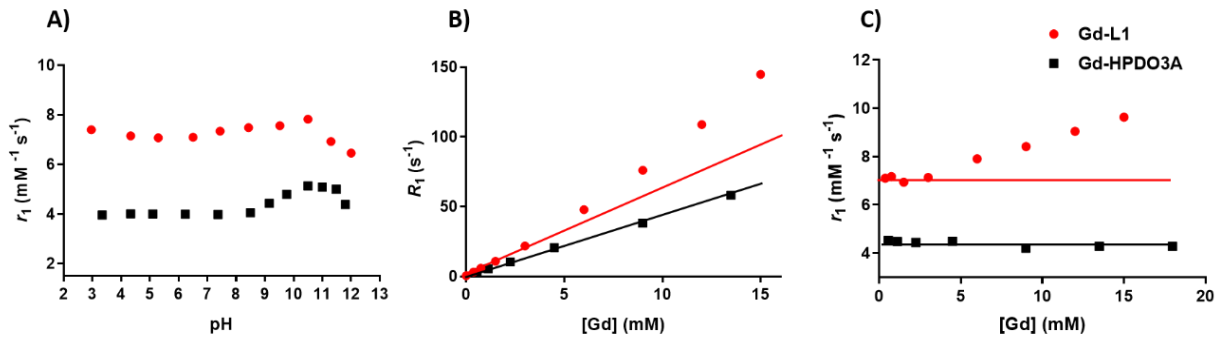

Figure 3.1. A) Relaxivity values (r_1) of Gd-L1 and Gd-HPDO3A in H_2O as a function of solution pH. **B)** Relaxation rates (R_1) in H_2O as a function of Gd-L1 or Gd-HPDO3A concentration at neutral pH. **C)** Corresponding relaxivity values (r_1) in the same concentration range and neutral pH. Data measured at 298 K and 21.5 MHz. In B) and C) the best-fit lines for Gd-L1 were obtained only with the points at [Gd] < 5 mM.

In pure water and at neutral pH, when Gd-L1 concentration was increased (Figure 3.1B), the relaxation rate values did not yield the expected linearity. This deviation from linearity is also evident in the relaxivity plot (Figure 3.1C), indicating that the relaxivity is not constant by varying the Gd-L1 complex concentration. This observed behavior suggests the occurrence of a weak intermolecular self-aggregation among Gd-L1 molecules, likely due to an interaction established between the pyrene-containing functionality and the tetra-aza macrocycle of Gd-HPDO3A, analogously to what was recently reported.[69] Indeed, such interaction causes a slowing-down of the molecular tumbling, leading to an increase in relaxivity. This behavior is consistent with the assumption that the linking arm is flexible enough to allow the interaction. The parent Gd-HPDO3A, as expected, showed a linear increase in R_1 as the concentration of the paramagnetic complex was increased (Figure 3.1B), with r_1 remaining constant throughout the entire range of examined concentrations (Figure 3.1C).

In human serum, the relaxivity of Gd-L1 displayed markedly higher values than in pure water, and it remained almost constant from 2 mM to 12 mM (Figure 3.2A).

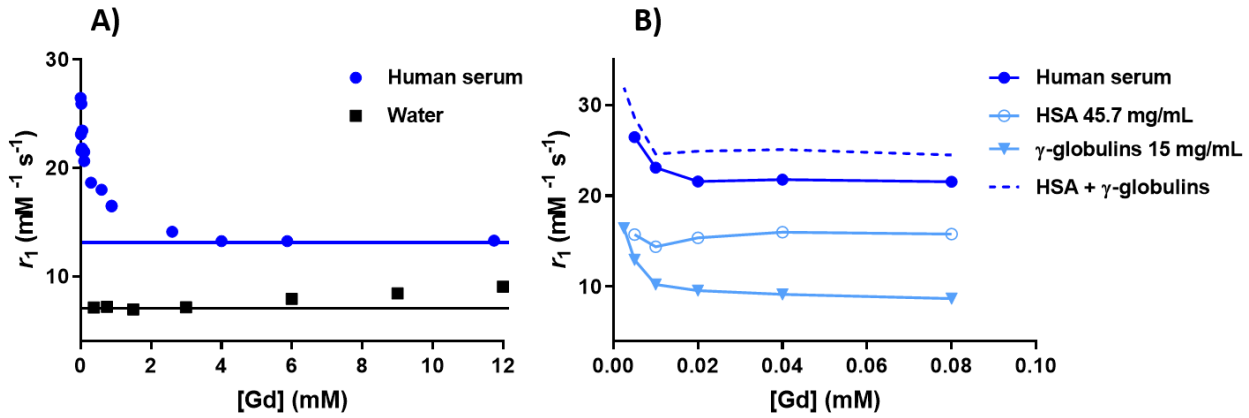

Figure 3.2. A) Relaxivity values of Gd-L1 in human serum and in pure water at neutral pH in the concentration range 0.005 - 12 mM. **B)** Expansion of the low concentration range data (0.005 - 0.08 mM) with the addition of relaxivity data obtained in PBS solutions containing HSA (45.7 mg/mL) and γ-globulins (15 mg/mL). The dotted line represents the calculated profile obtained by summing the relaxivities measured in the media containing γ-globulins and HSA, respectively. Data acquired at 298 K and 21.5 MHz.

Interestingly, in contrast to the behavior observed in water, the relaxivity values in serum showed a significant increase as the concentration of Gd-L1 was decreased below 1 mM, reaching exceptionally high values in the micromolar concentration range (Figure 3.2A). This unexpected trend prompted further investigation by measuring the relaxivity at concentrations below 0.1 mM (Figure 3.2B). To this end, the individual contributions of serum albumin and γ-globulins, which together constitute about three quarters of total serum proteins,[70] were examined (at their standard concentration in serum) in the low concentration range of Gd-L1. In PBS, in the presence of physiological HSA concentration (45.7 mg/mL), the relaxivity was almost constant at ca. 15.8 $mM^{-1}\,s^{-1}$ over the explored range of GdL1 concentrations (5-80 μM) (Figure 3.2B). In the case of γ-globulins containing solutions (15 mg/mL), in the same Gd-L1 concentration range, the relaxivity enhancement attained the values shown with HSA only at very low Gd-L1 concentration. The concentration of γ-globulins in serum is much lower (ca. 0.1 mM) than that of albumin (0.6 mM). Notably, in the considered Gd-L1 concentration range, the sum of the relaxivities measured for HSA and γ-globulins containing solutions, at their physiologic concentrations, yielded a profile (dotted line in Figure 3.2B) that nicely parallels the one observed in the case of whole blood serum.

A proton relaxation enhancement (PRE) titration[71] of a GdL1 0.28 mM solution with HSA (Figure 3.3A) yielded the following binding parameters: K_a = 489 M^{-1} and r_1^b = 39.8 $mM^{-1}s^{-1}$. The obtained association constant allows to calculate that, under the applied experimental conditions (i.e. [HSA] = 0.6 mM, [Gd-L1] = 5-80 μM), around 22% of the Gd-complex is bound to HSA. The PRE titration of a Gd-L1 50 μM solution with γ-globulins yielded the following results: K_a = 56 M^{-1}, r_1^b = 47.8 $mM^{-1}s^{-1}$).

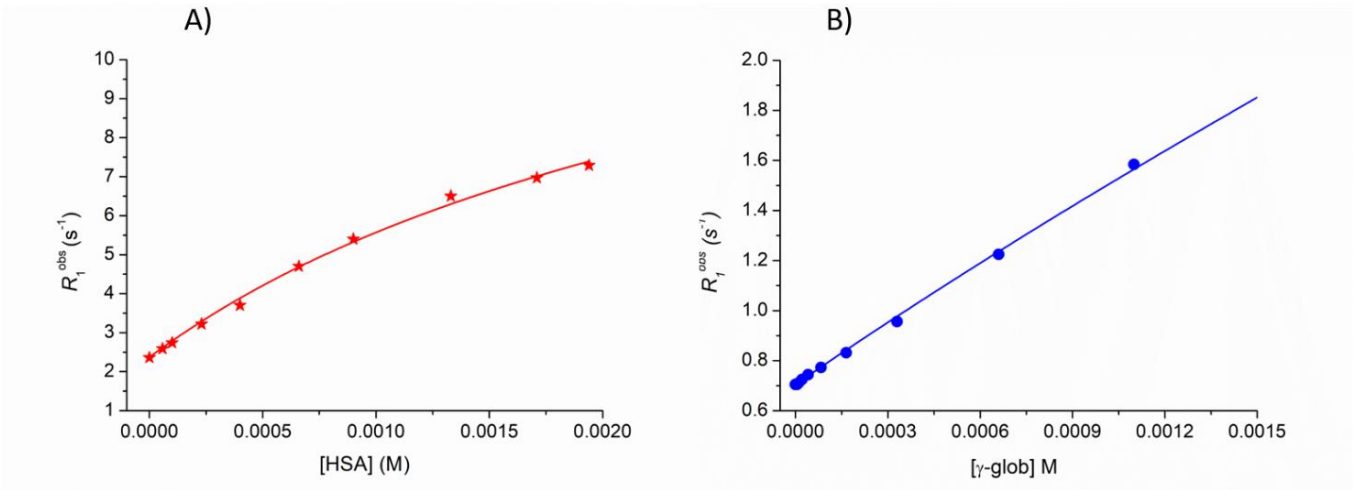

Figure 3.3. Proton relaxation enhancement (PRE) titrations of solutions of **A)** Gd-L1 (0.28 mM) with increasing amounts of human serum albumin (HSA) and **B)** Gd-L1 (0.05 mM) with increasing amounts of γ-globulins. Data measured at 298 K, 21.5 MHz, in PBS.

The striking similarities in the relaxivity behavior of Gd-L1 in the presence of both HSA and γ-globulins led us to hypothesize that the observed relaxation enhancement might be attributed to the interaction with NH_3^+ moieties exposed on the surfaces of these proteins. To gain further

insights into this possibility, we turned our attention to polylysine as an excellent model for investigating the role of amino groups on the surfaces of macromolecules. By studying polylysine, we aimed to better understand the impact of exposed amino groups on macromolecular surfaces and their potential involvement in the observed relaxation enhancement of Gd-L1 in the low concentration range. This investigation could provide valuable clues to unravel the underlying mechanisms behind the intriguing behavior of Gd-L1 in the presence of proteins, shedding light on the nature of the interaction responsible for the remarkable relaxivity enhancement observed at micromolar concentrations.

In the presence of 0.1 mM polylysine (MW = 30 - 70 kDa) Gd-L1 relaxivity increased up to ca. 13 $mM^{-1}\,s^{-1}$ (at 298 K and 21.5 MHz, in PBS, pH 7.4). The titration of Gd-L1 (0.1 mM) with increasing amounts of polylysine (concentration estimated on an averaged MW of 50 kDa) (Figure 3.4A) yielded a value of $n \times K_a = 1 \times 10^5\ M^{-1}$ and a relaxivity of the supramolecular adduct (r_1^b) of 15.3 ± 0.2 $mM^{-1}\,s^{-1}$. $n \times K_a$ indicates the association constant (K_a = 293 ± 48 M^{-1}) multiplied by the number of available binding sites (n = 342). It is worth to note that although the K_a value is relatively low, the overall value of $n \times K_a$ indicates a significant binding interaction. r_1 resulted dependent from the pH of the solution showing a steady increase to reach the maximum value of ca. 21 $mM^{-1}\,s^{-1}$ at pH 9 (Figure 3.4B).

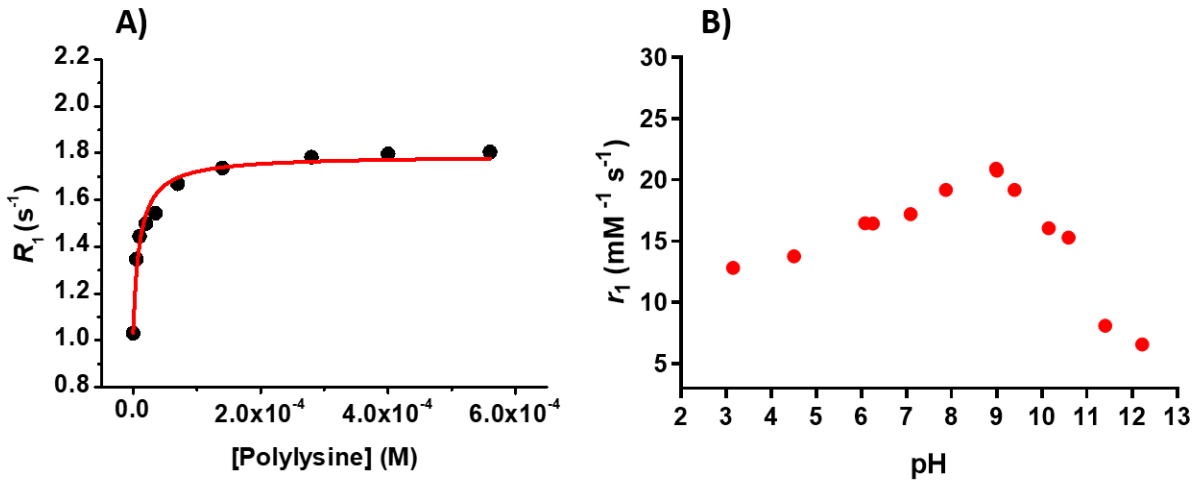

Figure 3.4. A) Relaxation rate of a 0.1 mM solution of Gd-L1 in the presence of increasing amounts of polylysine (avg. MW: 50 kDa). Data measured at 298 K and 21.5 MHz, in PBS at pH 7.4. **B)** Relaxivity values of Gd-L1 in the presence of polylysine (in 3:1 stoichiometric excess with respect to Gd-L1) as a function of the solution pH. Data measured at 298 K and 21.5 MHz, in PBS.

Based on these results, the next step dealt with the study of the relaxometric properties of Gd-L1 in a medium mimicking the extracellular matrix (ECM) whose collagen proteins are rich in NH_3^+ exposed residues.[72] A good material for simulating the complex tridimensional environment of ECM is Hystem™, a complex hyaluronic acid-based hydrogel matrix.[73] Hystem™ is commercially available in formulations in the presence or absence of collagen. In the collagen-containing medium Gd-L1 yielded the relaxivity of 12 $mM^{-1}\,s^{-1}$ that decreased to ca. 7 in the collagen-deprived product (Figure 3.5). As a control, the relaxivity of the parent

Gd-HPDO3A, measured under the same experimental conditions, showed only marginal difference considering the values in collagen-containing and collagen-free media. The different behavior of the two paramagnetic complexes clearly indicates that Gd-L1 is interacting with collagen. These fibrotic proteins, rich in lysine residues, are therefore excellent candidates for acting as target sites for Gd-L1 within the ECM.

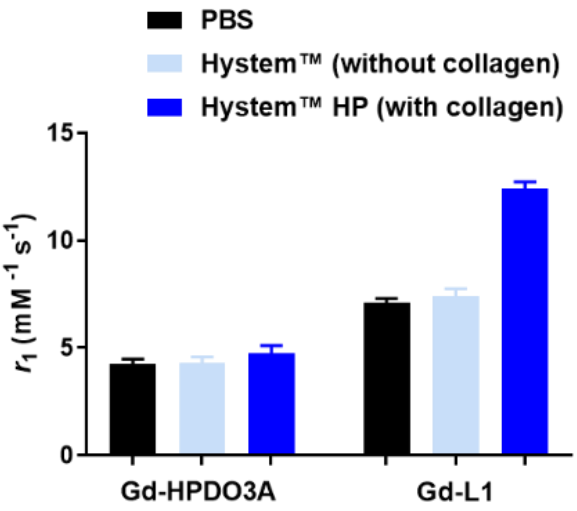

Figure 3.5. Relaxivity values of Gd-HPDO3A and Gd-L1 in PBS and in two Hystem™ media with and without the collagen component. The relaxation rates were measured with 0.1 mM Gd complex and normalized to 1 mM. Data acquired at 298 K and 21.5 MHz.

Next, the relaxometric properties of Gd-L1 were further investigated by measuring the ^{17}O-R_2 vs. T profile in water (compared to the parent Gd-HPDO3A in Figure 3.6A) and the nuclear magnetic resonance dispersion (NMRD) profiles in water and human serum (Figure 3.6B).

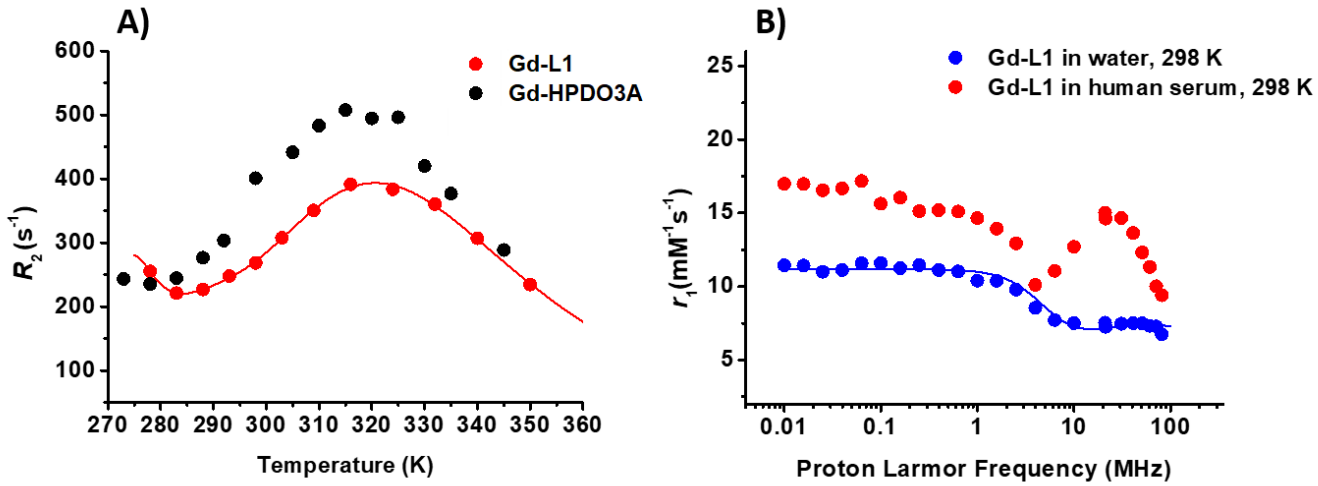

Figure 3.6. A) ^{17}O-R_2 vs. T profiles of Gd-L1 compared to that of Gd-HPDO3A measured in water at 14.2 T at pH 7.4; data normalized to 20 mM Gd concentration. **B)** ^{1}H-NMRD profiles measured on solutions of Gd-L1 1 mM in water and in human serum at 298 K, 298 K and pH 7.4.

The ^{17}O-R_2 vs. T profile measured for an aqueous solution of Gd-L1 (Figure 3.6A) has the typical shape observed in the presence of two species/isomers in solution.

As for the parent Gd-HPDO3A, they can be associated to TSAP and SAP diastereoisomers (TSAP/SAP ratio 30/70).[74,75] For Gd-L1, the isomers distribution resulted to be 60% TSAP and 40% SAP, in agreement with the ratio observed for Eu-L1 in Figure 3.7, where the mono- and bi-dimensional ^{1}H-NMR spectra are reported. The analysis of ^{17}O-R_2 vs. T profile allowed calculating the water exchange lifetimes (τ_M) of 1.9 ns and 470 ns for TSAP and SAP isomers, respectively, which resulted in a weighted average of 189 ns. Notably, the higher proportion of TSAP isomer is responsible for a τ_M substantially shorter than the one determined for Gd-HPDO3A, where the average τ_M was found to be 451 ns.[74,76]

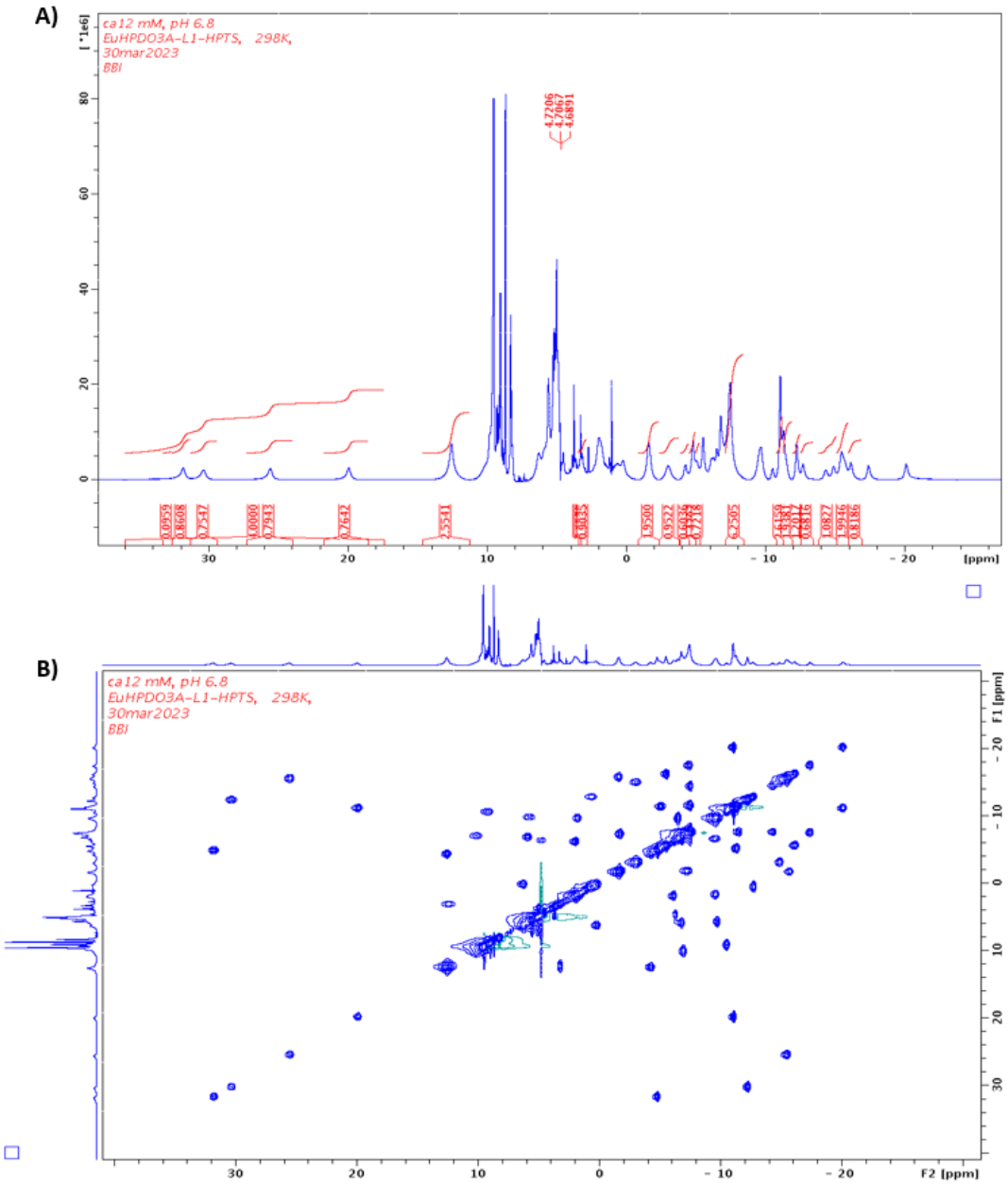

Figure 3.7. A) ^{1}H-NMR 1-D and **B)** 2-D EXSY spectra of 10 mM Eu-L1 (600 MHz, D_2O, water suppression, 298 K).

A rapid exchange of the coordinated water molecule is definitely a favorable feature for achieving high relaxivities upon binding to macromolecular systems.[8]
The NMRD profile of Gd-L1 in water (Figure 3.6B) was fitted by considering the contribution from 1.5 coordinated water molecules, i.e. one inner sphere water molecule plus the proton of coordinating alcoholic group whose involvement in the exchange with water appears to occur already at neutral pH. The NMRD profile of Gd-L1 in serum fully supports the view of the occurrence of a binding interaction to proteins that brings an elongation of the reorientational correlation time (τ_R) yielding a relaxivity hump at about 30 MHz. The quantitative analysis of ^{17}O-R_2 vs. T and NMRD profiles (in water) yielded the values of the relevant relaxometric parameters reported in Table 3.1.[74,76]

Table 3.1. Relaxometric parameters of Gd-L1 derived from the fitting of ^{17}O-NMR and ^{1}H-NMRD data measured in water (Figure 3.6), compared with the parameters reported for Gd-HPDO3A.[74,76]

	Gd-L1	**Gd-HPDO3A**
τ_M^{SAP} **(ns)**	470 ± 27.6	640 ± 35 [74]
τ_M^{TSAP} **(ns)**	1.9 ± 1.4	8.9 ± 0.5 [74]
$\tau_M^{w.avg.}$ **(ns)**	189 ± 11.2	451 [76]
τ_R **(ps)**	121 ± 3.5	65 ± 5 [74]
Δ^2 **(10^{19} s^{-2})**	5.45 ± 0.79	7.4 [76]
τ_v **(ps)**	17.5 ± 2.3	14.6 [76]

For the ^{17}O-NMR fitting procedure the following parameters were fixed: q = 1, r_{GdO} = 2.5 Å, E_r = 10 kJ mol^{-1}, E_v = 10 kJ mol^{-1}, A/ħ = -3.5 x 10^6 rad s^{-1}. The NMRD profiles were acquired at 298 K and the following parameters were fixed during the fitting procedure: q = 1.5, r_{GdH} = 3.1 Å, a_{GdH} = 3.8 Å, D_{GdH} = 2.24 x 10^{-5} cm^2 s^{-1}.

3.2.3 *In vivo* imaging studies

The MRI properties of Gd-L1 were investigated on healthy Balb-c mice. Very good contrast enhancements were observed in liver, spleen, and kidneys (Figure 3.8). The observed maxima in contrast enhancement in T_1-weigthed images were ca. two-six fold the values observed for ProHance (Gd-HPDO3A) administered at the same dose. Interestingly, the contrast effect decreased quite rapidly and the observed contrast enhancements for Gd-L1 and Gd-HPDO3A were almost the same already 15-30 minutes after the administration (Figure 3.9).

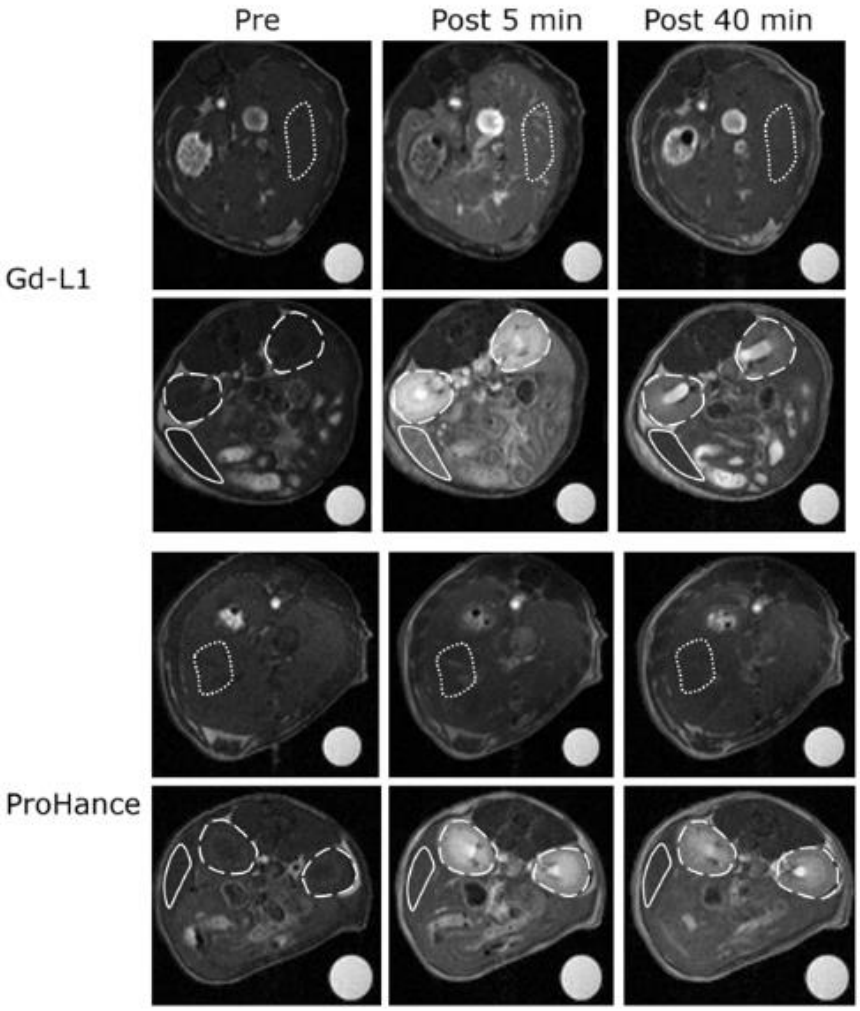

Figure 3.8. *In vivo* axial T_{1w}-MR images (at 7.1 T) of healthy Balb/c mice *pre* and *post* (at 5 min and 40 min) i.v. injection of Gd-L1 or ProHance 0.15 mmol/kg. For both agents the two rows of images show two representative slices. Dotted line indicates liver ROI, dashed line indicates kidneys ROI and continuous line indicates spleen ROI

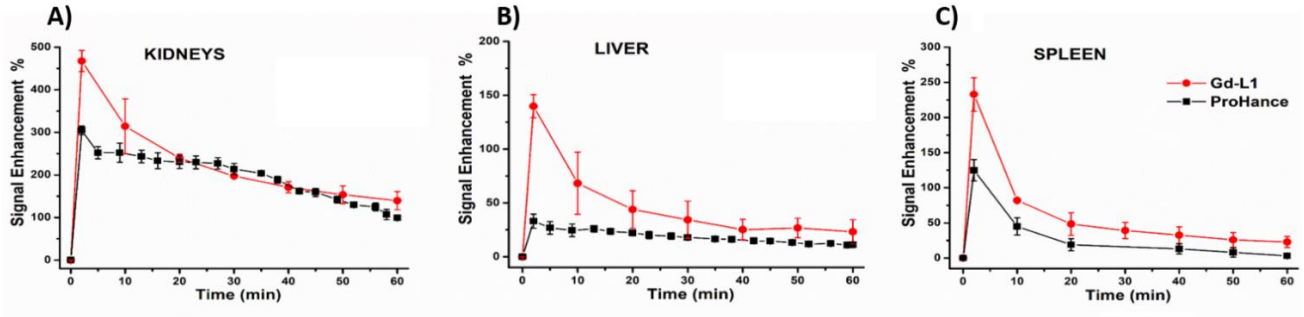

Figure 3.9. MR signal enhancement in kidneys (A), liver (B) and spleen (C) of healthy Balb/c mice (n = 3) upon injection of Gd-L1 or ProHance 0.15 mmol/kg. Squares and circles indicate the mean values; error bars indicate standard deviation.

3.2.4 Assessment of the elimination of Gd-L1 from blood

ICP-MS analyses for Gd quantification were conducted on blood samples collected from healthy mice at different time points (as shown in Figure 3.10) after intravenous administration of 0.15 mmol/kg of contrast agent, in order to determine the rates of elimination of Gd-L1 and ProHance from the blood.

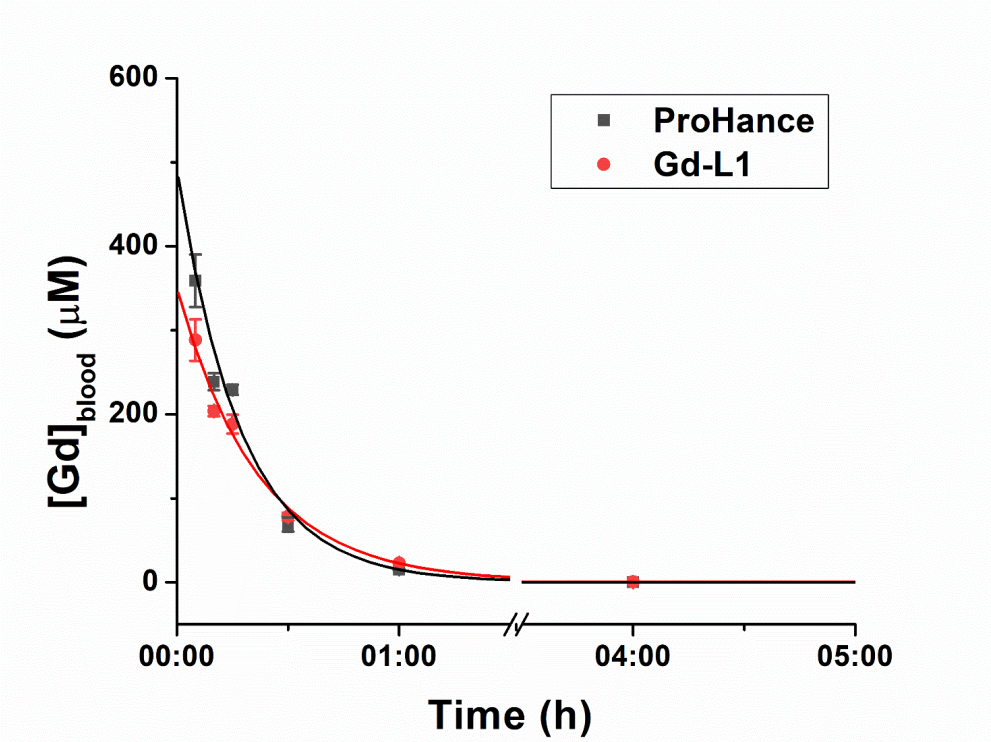

Figure 3.10. Blood elimination curves of Gd-L1 and ProHance upon the intravenous administration of 0.15 mmol/kg of contrast agent in healthy mice.

The elimination rate of Gd-L1 from the bloodstream resulted to be only slightly less rapid than that of ProHance, with elimination half-lives of 14.1 ± 1.7 and 12.1 ± 1.6 minutes observed for Gd-L1 and ProHance, respectively.

3.3 Discussion

Gd-L1 has proven to be a valuable model system for the investigation of novel interactions with endogenous proteins. The metal complex has three residual negative charges located at the external perimeter of the pyrene substituent. The presence of the sulfonate moieties endows the molecule with good water solubility, while the conjugated aromatic system provides an excellent source of π-electrons.

In a recent study, it was demonstrated that the parent HPTS system can be exploited for the set-up of hydrophobic interactions with the tetraazacyclododecane cage of macrocyclic Gd-complexes.[69] In the case of Gd-L1, aside from similar weak π-bonding associations, the primary binding properties appear to be driven by interactions with positively charged aminoacidic residues exposed on protein surfaces. These are typically represented by lysine or

arginine residues found in serum proteins and collagen proteins. Gd-L1 is not expected to show any binding interaction with proteoglycans, the main constituents of the ECM, as they are often negatively charged systems (e.g., heparan sulfate, hyaluronic acid, chondroitin sulfate, dermatan sulfate). However, there may be a limited effect due to increased viscosity, as indicated by the slight increase observed for the parent Gd-HPDO3A in Hystem™ (Figure 3.5).

In water, the Gd-L1 relaxivity value of 7.1 mM^{-1} s^{-1}, measured for a concentration of 1 mM at 21.5 MHz, 298 K, and neutral pH, is consistent with the occurrence of intramolecular catalysis of the prototropic exchange of the coordinated alcoholic group.[77,78] This catalysis likely involves the amide proton, as previously demonstrated for similar systems.[79–81] In the case of Gd-L1, the catalytic effect appears even more pronounced, as the contribution of the OH moiety is evident already at neutral pH values. Additionally, the increased rotational correlation time (τ_R), due to the higher molecular weight compared to the parent Gd-HPDO3A, also plays a significant role in the observed relaxivity enhancement.

The observed decrease in relaxivity at pH > 10 seems to indicate a structural change following the deprotonation of the alcoholic moiety, as previously observed for the parent Gd-HPDO3A.[51,79]

The ^{17}O-R_2 vs. T measurement of Gd-L1 suggests the occurrence of the SAP and TSAP diastereoisomers as observed for the parent Gd-HPDO3A, with an increase of the TSAP form. This finding is further supported by the acquisition and interpretation of the ^1H-NMR spectra of Eu-L1 which clearly showed a distribution of the two diastereoisomers with a ratio TSAP/SAP 3:2 (Figure 3.7). Indeed the cationic radii of Eu^{3+} and Gd^{3+} are very similar (94.7 pm and 93.5 pm, respectively) so that the TSAP/SAP ratios of their HPDO3A-like complexes are commonly considered analogous with reasonable approximation.[74,75]

In water, the increase in r_1 upon increasing the Gd-L1 concentration suggests the reversible formation of aggregates based on the hydrophobic interactions between the pyrene derivative moiety and the tetra-aza macrocycle of Gd-HPDO3A, similarly to what previously observed in binary mixtures of Ln-HPDO3A (Ln = Gd, Eu, Yb) and HPTS.[82] It seems reasonable to expect that the constrain introduced on the pyrene derivative containing moiety upon its binding to Gd-HPDO3A causes a weakening in the hydrophobic interaction with respect to the case of the binary mixtures of the two parent molecules.

In human serum, at the GdL1 concentration 0.1 mM, the relaxivity reached the value of 21.5 mM^{-1} s^{-1}, at 21.5 MHz and 298 K. A set of r_1 measurements of Gd-L1 as a function of the Gd concentration (Figure 3.2) clearly showed that the relaxivity in serum is markedly affected when the concentration is < 0.02 mM reaching the exceptional value of 26.5 mM^{-1} s^{-1} at the lowest measured concentration (5 μM). Above 4 mM, the relaxivity in serum remained constant at the remarkable value of ca. 13.5 mM^{-1} s^{-1}. These observed high values indicate that, in serum, Gd-L1 is interacting with sites on the endogenous macromolecules that cause an elongation of its reorientational time (τ_R) and, in turn, yields to the observed enhancement. The comparison of the NMRD profiles acquired in water and in human serum (Figure 3.6B) unambiguously supports this view.

The marked effects on the relaxation enhancements when decreasing the molar ratio between Gd-L1 and the interacting macromolecule (Figure 3.2B) can be associated with the shift of the equilibrium towards the bound form endowed with higher relaxivities. This finding aligns with the concept that, in the presence of multiple binding sites, there is a preference for binding to sites with higher affinity.

Upon carrying out a relaxivity vs. HSA concentration assessment, it was clear that this protein is the major pool for the set-up of binding interactions of Gd-L1, in serum. Considering the presence of three sulfonate groups on the outer perimeter of the pyrene moiety, it seems unlikely for the metal complex to bind at the hydrophobic Sudlow sites. Therefore, it appears reasonable that hydrophilic pyrene substituent may interact with the positively charged NH_3^+ groups of lysine or arginine residues exposed on protein surfaces. To gain a deeper understanding of this possibility, we undertook a relaxometric study of Gd-L1 with polylysine (PL) (Figure 3.4). Although the highly flexible random coil configuration adopted by PL at neutral pH[83] may restrict the potential enhancement, the observed relaxivity increase revealed a binding interaction with the positively charged NH_3^+ groups. When the binding occurs, the decrease in PL protonated ε-NH_3^+ moieties may induce a conformational change to a less flexible alpha helix structure that, in turn, results in an enhanced relaxivity.[83] This effect is indeed counteracted by the decrease of protonated ε-NH_3^+ moieties but the lengthening of τ_R is likely more crucial in determining the observed relaxation enhancement. Given that the $n \times K_a$ value is high (1×10^5 M^{-1}), one could conclude that each binding site in this polypeptide is independent from the others. Obviously, the large number of binding sites (up to 342 lysine residues are available in the used homopolymer) indicates that the affinity for each lysine residue is relatively low.

Next, it was decided to investigate whether other proteins might contribute to the increased relaxivity of Gd-L1 in serum, as compared to the buffered HSA solution, in particular at the lower concentrations of the paramagnetic complex. Reasoning that electrostatic and cation-π binding interactions may be responsible for the observed effect, we studied Gd-L1 relaxivity in γ-globulin containing media. This class of proteins, characterized by a basic isoelectric point, appeared as a good candidate for the desired interactions. The titration of a buffered solution of γ-globulins with increasing amounts of Gd-L1 resulted in a profile that clearly paralleled the behavior observed in serum. This suggests that γ-globulins are likely the macromolecular system contributing to the relaxation enhancement detected in serum, in addition to the greatest one provided by HSA.

To determine whether the molecular interactions responsible for the relaxation enhancement in serum are also active in the ECM, it was deemed of interest to measure r_1 of Gd-L1 in an ECM-mimicking medium. To this intent, we used Hystem™ (a mixture of polysaccharides, proteins and other components) which is commercially available in a composition with or without collagen.[73] The comparison between the relaxivities in the two Hystem™ media (Figure 3.5) clearly indicates that Gd-L1 displays a higher relaxivity in the presence of collagen, whereas for the parent Gd-HPDO3A such a difference is much less pronounced. Collagen fibers own a large number of lysine residues only partially used for the generation of

the matrix network; thus, collagen in the ECM may represent a potential binding site for Gd-L1. Further evidence for this hypothesis was gained by acquiring the in vivo MRI images of three organs (liver, spleen, kidneys) that are known to be highly fenestrated, thus allowing an easy extravasation of Gd-L1 to the ECM. The signal enhancement (SI%) measured immediately after the i.v. administration of Gd-L1 in the three organs reached values up to two-sixfold higher than those observed for the parent Gd-HPDO3A (Figure 3.9). At a first glance, the *in vivo* results were not expected, since the MRI scans were acquired at 7 T; in fact, this field strength does not allow to take advantage of the remarkable relaxation enhancement whose maximum is at around 1 T. A possible explanation is that the observed behavior reflects an increased retention of Gd-L1 in the vascular and extravascular space due to the set-up of numerous binding interactions with the proteins in these media.

The *in vitro* results appear then fully confirmed by the *in vivo* observations, showing that the weak electrostatic and cation-π interactions, likely exploiting the NH_3^+ moieties of lysine or arginine residues on different endogenous proteins, are a powerful source for the generation of an improved response in contrast enhanced (CE)-MR images.

The improved *in vivo* response of Gd-L1 showed a limited persistence (Figure 3.9). Indeed, the effect largely disappeared already after 10-15 minutes, when the detected SI% for Gd-L1 became comparable to the one shown by the clinical Gd-HPDO3A. The observed behavior can be explained in terms of the "washing out" of Gd-L1 from ECM. In the tissues examined, the ECM space is limited and the ratio between the amount of extravasated Gd-L1 and the number of interaction sites on the endogenous macromolecules may favor the involvement of the strongest binding sites.

According to the Gd elimination curves from blood (Figure 3.10), the excretion kinetics of Gd-L1 from the bloodstream are very similar to those of Gd-HPDO3A.

Therefore, the exploitation of the weak, although abundant, NH_3^+-involving interactions yielded a great signal enhancement without affecting the excretion characteristic, that remained comparable to those of the parent Gd-HPDO3A. The limited persistence of the strong enhancement may be considered with interest as the CE-MR images are commonly acquired immediately after the administration of the contrast agent.

3.4 Conclusion

In summary, Gd-L1 proved to be a good model for investigating new routes to electrostatic and cation-binding interactions with NH_3^+-exposing macromolecules, to search for significant relaxation enhancement and increased signals in T_1-weigthed MR images. The significant rise in signal enhancement found shortly after i.v. administration suggests that Gd-L1 can be employed at doses significantly lower than those normally used with currently available GBCAs.

As a result, Gd-L1 can be regarded as the prototype of a novel class of GBCAs: small-sized and hydrophilic paramagnetic complexes capable of interacting with endogenous proteins in the vascular system and the ECM. The findings presented here provide fresh insights into the development of paramagnetic MRI CAs with high relaxivity and a regulated biodistribution and excretion pathway.

3.5 Experimental section

Chemicals were purchased from Sigma-Aldrich Co. NMR spectra were recorded at 310 K on a Bruker AVANCE 600 spectrometer operating at 14 T (corresponding to 600 and 150 MHz ^{1}H and ^{13}C Larmor frequencies, respectively). Analytical and preparative HPLC−MS was carried out on a Waters Auto Purification system (3100 Mass Detector, 2545 Pump Gradient Module, 2767 Sample Manager, and 2998 PDA detector). The purity was double checked by analytical HPLC using Atlantis C18, 3.5 μm, 4.6 mm × 150 mm column and 0.1% TFA in water (solvent A) and acetonitrile (solvent B); applying a gradient of CH_3CN in H_2O (0.1 %TFA) from 5 to 80% in 15 min and from 80 to 100% in 5 min, flow 1 mL min^{-1} (method 1). pH measurements were made using an AS pH meter equipped with a glass electrode.

3.5.1 Synthesis of Gd-L1 and Eu-L1

The synthesis of Gd-L1 and Eu-L1 was performed by colleagues in the research group. Thus, in this this section the experimental details of the synthesis steps are not reported.

The characterization data of the purified two final products investigated in this work are the following:

GdL1 retention time = 3.36 min, purity = 95%, λ = 220 nm; ESI-MS m/z calculated for $C_{35}H_{40}GdN_5O_{18}S_3$: $[M+H]^+$ 1073.08, found 1073.41; $[M+2H]^{2+}$ 537.04, found 537.31; $[M-H]^-$ 1071.08, found 1072.40; $[M-2H]^{2-}$ 535.04 , found 535.42.

EuL1 retention time = 3.46 min, purity = 95%, λ = 220 nm; ESI-MS m/z calculated for $C_{35}H_{40}EuN_5O_{18}S_3$: $[M+H]^+$ 1068.07, found 1068.06; [M-H] 1066.07, found 1066.06; $[M-2H]^{2-}$ 532.03, found 532.59.

3.5.2 Relaxometric measurements

Observed longitudinal relaxation rates ($R_1^{obs} = 1/T_1^{obs}$) values were determined by inversion recovery at 21.5 MHz and 298 K using a Stelar SpinMaster spectrometer (Stelar s.r.l, Mede (PV), Italy). Temperature was controlled with a Stelar VTC-91 airflow heater and the temperature inside the probe checked with a calibrated RS PRO RS55-11 digital thermometer. Data were acquired using a recovery time ≥ 5 x T_1 and with 2 scans per data point. The absolute error in R_{1obs} measurements was less than 1%.

Gadolinium concentration of each solution was determined as follows: a solution containing equal volumes of the Gd(III)-complex solution and 37% HCl was mixed in a sealed vial and left overnight at 393 K. R_1^{obs} values of the acidic solution were determined and the total concentration of Gd^{3+} was evaluated on the basis of the following equation: $[Gd] = (R_1^{obs} - R_1^{d})/ r_{1p}^{Gd}$, where R_1^{d} is the diamagnetic contribution (0.5 s^{-1}) and r_{1p}^{Gd} the relaxivity of the Gd(III) ion in acidic conditions (13.5 $mM^{-1}\,s^{-1}$).[50]

NMRD profiles were obtained using a Stelar SmartTracer FFC NMR relaxometer from 0.01 to 10 MHz. Additional data in the 20−80 MHz frequency range were obtained with a High Field Relaxometer (Stelar) equipped with the HTS-110 3T Metrology cryogen-free superconducting magnet and a Bruker WP80 NMR electromagnet (21.5–80 MHz), both equipped with a Stelar VTC-91 for temperature control; the temperature inside the probe was

checked with a calibrated RS PRO RS55-11 digital thermometer. Aqueous and human serum solutions of the complex were measured at 298 K. The NMRD profiles data were fitted using the Solomon-Bloembergen-Morgan and Freed's models.

O^{17}-R_2-NMR measurements were recorded at 14.1 T on a Bruker Avance 600 spectrometer at variable temperature, with a D_2O sealed capillary for sample locking inside the tube. The 20 mM Gd-complexes solutions were enriched with 1% of $H_2{}^{17}O$ (Cambridge Isotope). The width at half maximum ($\Delta\omega_{dia}$) of the $H_2{}^{17}O$ signal in pure water was measured over the investigated temperature range and subtracted from the width at half maximum ($\Delta\omega_{Gd}$) of the tested Gd-complexes solutions. Then, R_2 was calculated as follows: $R_2=\pi[\Delta\omega_{Gd}-\Delta\omega_{dia}]$.

3.5.3 Animal handling

For the *in vivo* imaging experiments, 8-10-week-old male Balb/c mice (Charles River Laboratories, Calco, Bergamo, IT) were used. The mice were bred at the animal house at the Molecular Imaging Center (MBC) at the University of Turin. They were kept in standard housing conditions with standard rodent chow, water available *ad libitum* and a 12-hour light/dark cycle. All procedures involving animals were performed in accordance with national and international laws on the use of experimental animals (L.D. 26/2014; Directives 2010/63/EU) under Ministerial Authorization (project Research Number 888/2021-PR protocol CC652.167.EXT.53).

3.5.4 MRI acquisition and data analysis

For MRI experiments, mice were anesthetized by intramuscular injection of a mixture of 20 mg/kg tiletamine/zolazepam (Zoletil 100, Virbac, Milan, Italy) 20 mg/kg plus 5 mg/kg xylazine (Rompun; Bayer, Milan, Italy). A permanent vein access was obtained by inserting a PE10 catheter into the tail vein. A glass tube containing a standard solution was used as internal reference. It was located in the field of view in close proximity to the mouse body. MR images were acquired, pre and post injection of Gd-complexes, at 7.1 T by using a Bruker Avance 300 spectrometer equipped with a Micro 2.5 microimaging probe, at room temperature (ca. 21 °C). Mice were intravenously injected with either 0.15 mmol/kg of Gd-L1 or 0.15 mmol/kg of ProHance. T_{2w} images were acquired by using a standard T_{2w} RARE (Rapid Acquisition with Refocused Echoes) sequence with the following parameters (TR=5000ms, TE=5.5ms, RARE factor=32, FOV=3.5x3.5 cm, slice thickness=1 mm, matrix 128x128). T_{1w} images were acquired immediately after the injection of Gd-L1 or ProHance by using a standard T_{2w}-MSME (multislice multiecho) sequence with the following parameters (TR=200 ms, TE=3.3ms, number of averages=6, FOV=3.5x3.5 cm, slice thickness=1 mm, matrix 128x128, resolution 0.273x0.273 mm/pixel).

ROIs were manually drawn inside the organs of interest (spleen, liver, kidneys) and the mean of signal intensity (at least 5 ROIs in different slices) were calculated. Signal enhancement was calculated used the following formula: (($SI^{post} - SI^{pre}$) / SI^{pre}) x 100

Where SI^{pre} and SI^{post} are the signal intensities in T_{1w} images before and after the injection of Gd-complexes, respectively, upon normalization for the signal in the reference tube.

3.5.5 Assessment of blood elimination by ICP-MS

The pharmacokinetics of intravenously administered Gd-L1 and ProHance were assessed by ICP-MS quantification of the Gd content in plasma. For this purpose, after the intravenous injection of 0.15 mmol/kg of Gd-L1 or ProHance to healthy mice (n=3), blood was collected from mouse tail veins at variable time points (t = 5 min, 10 min, 15 min, 30 min, 1 h and 4 h). Before ICP-MS analysis, blood samples were digested with concentrated HNO_3 (70%) under microwave heating (Milestone MicroSYNTH Microwave lab-station, Balgach, Switzerland, equipped with an optical fiber temperature control and HPR-1000/6M high-pressure reactor, Milestone, Bergamo, Italy). After the digestion, 3 mL of ultrapure water were added to each sample. The specimens were then subjected to ICP-MS analysis (Element-2; Thermo-Finnigan, Rodano (MI), Italy) to measure the concentration of Gd with respect to standard curves. Results were reported as Gd micromolar concentration as a function of collection time.

Chapter 4

PET/MRI co-agents for the measurement of extracellular pH in the tumor microenvironment

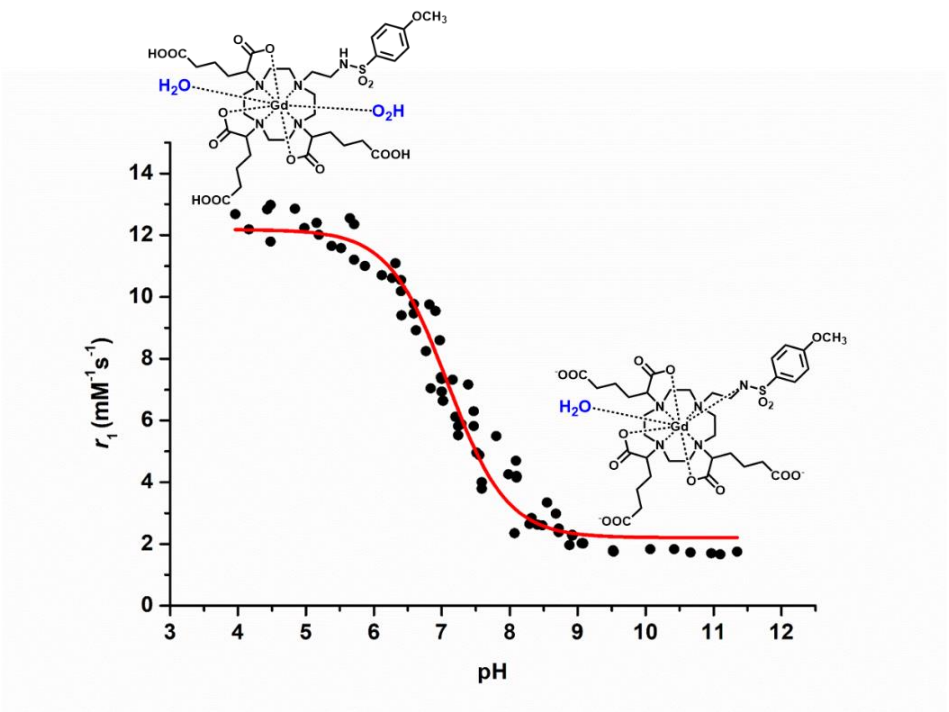

4.1 Introduction

Contrary to normal cells, malignant cancer cells exhibit a distinctive metabolic profile characterized by an elevated rate of aerobic glycolysis, often referred to as the Warburg effect.[84] In this condition, cancer cells preferentially convert glucose into lactate, even in an oxygen-rich environment. The production of lactate generates an accumulation of lactic acid in the extracellular region, leading to a more acidic extracellular pH (pHe).[85] Indeed, whereas the pHe of normal tissues is not lower than 7.0, solid tumors can reach pHe values as low as 6.5.[86] Such a change in pH, known as tumor acidosis, has been linked to a range of detrimental consequences for cancer progression, including augmented tumor growth rate, invasion, and metastasis.[87–89] Furthermore, tumor acidity can hinder the efficacy of immunotherapy and certain chemotherapeutic agents.[90,91] Assessments of pHe in tumors can additionally serve as a means to anticipate and track the impact of drugs and antibodies that are sensitive to pH.[92,93] Although these are crucial potential applications, there are limited methods available for non-invasively measuring tumor pHe, and none have gained routine clinical use. Optical imaging, while capable of assessing tumor pHe, is restricted to surface-accessible tumors and cannot provide comprehensive tumor volume information. Positron emission tomography (PET), electron paramagnetic resonance spectroscopy (EPR), and MR spectroscopy offer alternative approaches, but with limitations such as poor accuracy, sensitivity or arduous translation into clinical settings.[94]

In the absence of established methods for directly measuring tumor pHe in clinics, advancements in CA research have paved the way for indirect estimation of tumor extracellular pH. MRI CAs (clinically approved computed tomography (CT) CAs, repurposed for MRI) detectable by means of CEST effect have been intensively investigated and used to measure pH.[94,95] Many relaxivity-based MRI T_1 CAs with a pH-dependent relaxivity have also been developed. As previously explained in the paragraph 1.1.2.4, these responsive CAs undergo pH-dependent alterations that can be detected using MRI. However, being the MR signal amplitude dependent on the CA concentration, the use of another imaging technique to assess the concentration of the MRI CA is needed. Positron emission tomography (PET) can provide the opportunity to overcome this concentration dependence issue by using the PET component to report on the concentration of the pH-responsive MRI agent.

Pollard et al. designed and synthesized a pair of PET/MRI co-agents aiming to measure pHe.[44] Through a simultaneous PET/MRI procedure, they managed to accurately measure pH both in solution and *in vivo*, although metabolism studies on murine models showed evidence that the co-agents were degraded *in vivo* after 20 minutes. The designed co-agents consist in the Gd and ^{68}Ga complexes of a DO3A derivative functionalized with a sulfonamide arm that can be protonated or not based on the pH of the environment. In the case of the MRI co-agent, the protonation of the sulfonamide leads to the displacement of the coordinating nitrogen from the Gd ion, and to the replacement with a water molecule, with a relaxivity increase. This process is schematized in Figure 4.1.

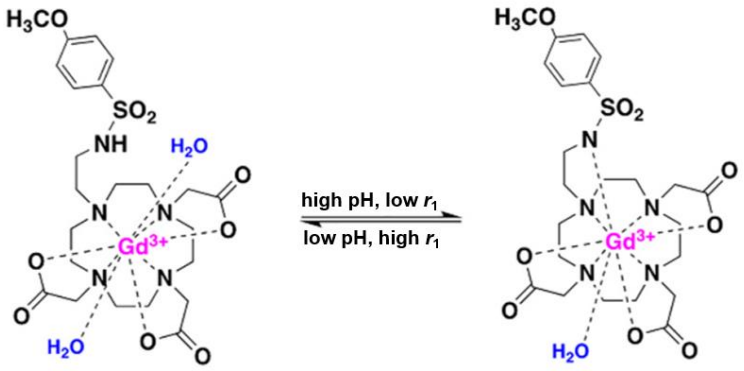

Figure 4.1. At lower pH values the sulfonamide group of the MRI co-agent is protonated and two water molecules are coordinated to the Gd ion (q = 2, higher r_1 relaxivity). At higher pH values the coordination of the deprotonated nitrogen displaces one water molecule (q = 1, lower r_1 relaxivity). Modified from [44].

As PET co-agent, the corresponding ^{68}Ga complex was used, assuming that the two co-agents have the same pharmacokinetics. Thus, with a known ratio of MRI co-agent to PET co-agent, the radioactivity measured by the PET detector can be translated into concentration of the MRI co-agent. Then the r_1 relaxivity values can be calculated from the measured relaxation rates via MRI and pH can be determined using a calibration curve of pH vs. r_1. Although the evidence of *in vivo* degradation for the compounds used in this initial study, this new approach definitely appeared promising and worthy of further investigations.

In this context, during the period abroad spent at the MD Anderson Cancer Center in Houston, Texas, I had the opportunity to work on new metal-based compounds aiming to the measurement of pHe through simultaneous PET/MRI.

Previous works on Gd complexes based on the DO3A macrocyclic structure reported that, the introduction of three β-carboxyalkyl substituents, α to three ring nitrogens, can inhibit the displacement of the bound water inducted by added proteins and also suppresses intermolecular binding by endogenous anions.[47] The presence of other carboxylate moieties is also expected to both increase the solubility of the ligand and its metal complexes and to improve their biocompatibility, while maintaining, in the case of the Gd(III) complex, a pH dependent relaxivity.

The compound 3b, previously synthesized and investigated in our research group in Torino, (chemical structure in Chart 4.1), was made available for these studies.

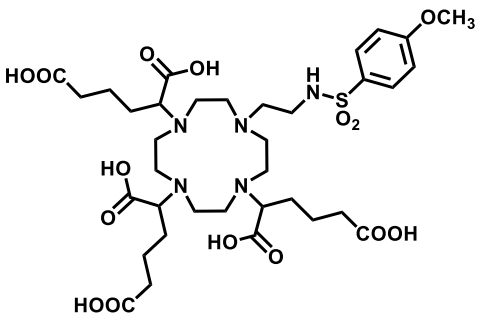

Chart 4.1. Chemical structure of the ligand 3b.

The aims of the project were the following: i) to synthesize the Gd complex of the compound 3b and test its pH-dependent relaxivity for application as MRI co-agent in simultaneous PET/MRI; ii) to synthesize the ^{68}Ga and ^{86}Y complexes of the compound 3b for the application as PET co-agents; iii) to test the ^{68}Ga-3b/Gd-3b and ^{86}Y-3b/Gd-3b PET/MRI co-agents pairs for the measurement of tumor extracellular pH in murine models.

4.2 Results and discussion

4.2.1 MRI co-agent

4.2.1.1 Synthesis of the MRI co-agent Gd-3b

The synthesis and purification of Gd(III) 1-[(2'-(4-methoxyphenylsulfonaminoethyl]-4,7,-10-tris-[(4'-carboxy)-1'-carboxybutyl]-1,4,7,10-tetraazacyclododecane (Gd-3b) (Scheme 4.1) was made by following the procedure reported in literature.[47] The absence of free Gd was confirmed using a solution of arsenazo III dye.[96]

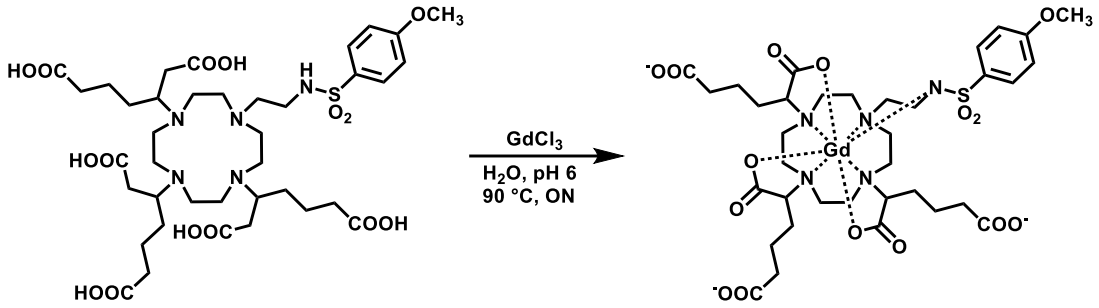

Scheme 4.1. Synthesis of Gd-3b.

4.2.1.2 pH-relaxivity calibration curve

To obtain a pH-relaxivity calibration curve, samples containing Gd-3b in pure water were prepared at different concentrations and pH values. The relaxation rates of the solutions were measured in a 7 T MRI scanner and used to calculate the relaxivity values shown in Figure 4.1. The fitting of the experimental data was done by using the modified Henderson-Hasselbach equation:

$$\mathrm{pH} = \mathrm{pKa} + \log\left(\frac{r_1 - \mathrm{a}}{\mathrm{b} - r_1}\right)$$

pKa is the pKa of the sulfonamide arm (7.09) of the MRI co-agent; r_1 is the relaxivity of the measured sample; *a* is the relaxivity at low pH when the sulfonamide is completely protonated; *b* is the relaxivity at high pH when the sulfonamide is completely deprotonated.

The fitting of the experimental data allowed to calculate the values of a = 12.18 $mM^{-1}\,s^{-1}$ and b = 2.20 $mM^{-1}\,s^{-1}$.

As schematized in Figure 4.1, at low pH the Gd complex is endowed with a very high relaxivity due the coordination of two water molecules (q = 2). Moving to higher pH values the coordination of the deprotonated sulfonamide nitrogen to the metal center leads to the displacement of a water molecule with the consequence of lower relaxivity values as the concentration of the agent with q = 1 increases.

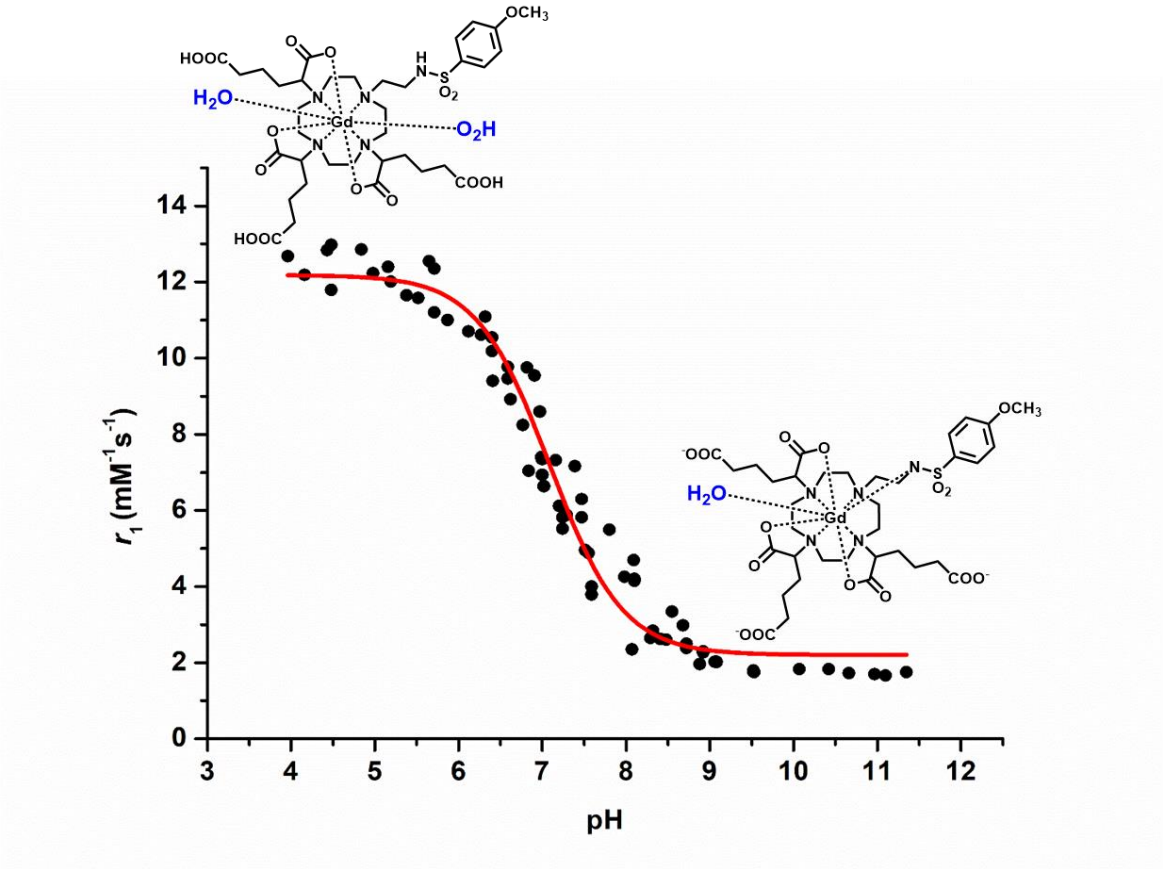

Figure 4.1. Observed relaxivity values as a function of pH, in water at 310 K and 7 T.

It is worth to note that the Gd-3b species with q = 2 has a relaxivity value more than twofold than the MRI co-agent previously studied (12.18 $mM^{-1}\,s^{-1}$ vs. 6.07 $mM^{-1}\,s^{-1}$), while the relaxivity of the form with q = 1 is rather similar (2.20 $mM^{-1}\,s^{-1}$ vs. 1.77 $mM^{-1}\,s^{-1}$).[44] This is a definitely favorable feature for this application, as it is reflected in a larger relaxivity variation upon slight pH changes allowing, in principle, more sensitive pH measurements.

4.2.2 PET co-agents

4.2.2.1 ^{68}Ga-3b

4.2.2.1.1 Radiosynthesis and purification

The synthesis of ^{68}Ga(III)-1-[(2'-(4-methoxyphenylsulfonaminoethyl]-4,7,-10-tris-[(4'-carboxy)-1'-carboxybutyl]-1,4,7,10-tetraazacyclododecane (^{68}Ga-3b) was optimized by varying different reaction conditions such as temperature, pH, time of reaction, type of buffer and amounts of reagents. The best conditions are shown in Scheme 4.2. After the optimization, the scale-down of the ligand amount necessary for the radiolabeling led to a value of [3b] = 0.1 mM in the final volume of reaction mixture.

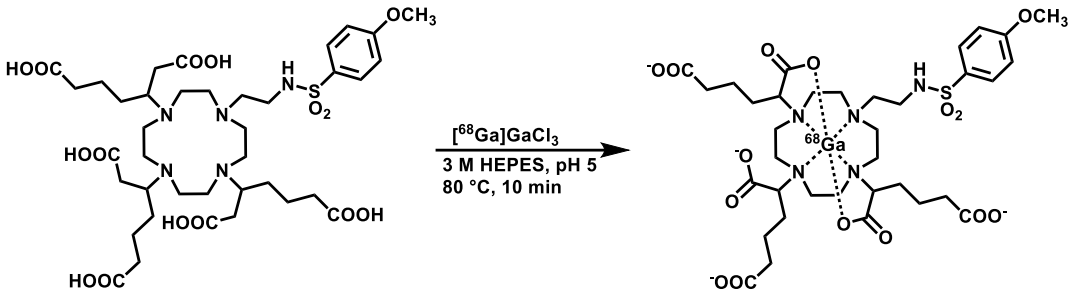

Scheme 4.2. Optimized conditions for the radiosynthesis of ^{68}Ga-3b.

Reaction completion was confirmed via radioHPLC. The reaction mixture was loaded onto a pre-conditioned C18 cartridge and eluted with 1 mL of ethanol and divided in 5 fractions, to obtain the pure concentrated product (radioHPLC chromatogram shown in Figure 4.2).

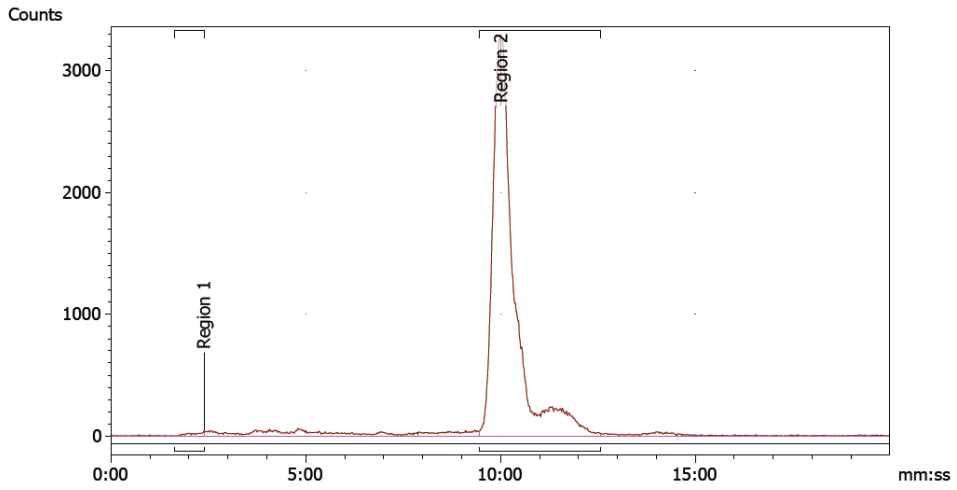

Regions: ^{18}F Detector: PMT

Name	Start (mm:ss)	End (mm:ss)	Retention (mm:ss)	Area (Counts)	%ROI (%)	%Total (%)
Region 1	1:38	2:24	2:23	628	0.52	0.47
Region 2	9:28	12:34	10:01	120484	99.48	89.36
2 Peaks				121112	100.00	89.82

Total Area: 134832 Counts
Average Background: 0 Counts

Figure 4.2. RadioHPLC chromatogram of ^{68}Ga-3b.

The optimization of synthesis and purification steps allowed to obtain the compound ^{68}Ga-3b with the high radiochemical purity of 99.5%.

4.2.2.1.2 Tumor uptake preliminary studies

To test the *in vivo* stability of ^{68}Ga-3b, tumor-bearing mice were injected with a saline/ethanol 8:2 solution of the agent. 3 mice were injected intratumorally (i.t.) and 3 mice were injected intravenously (i.v.). The mice were sacrificed and the tumors were treated with acetonitrile, mixed thoroughly and subjected to centrifugation for 10 min at 4000 rpm. The acetonitrile layer was removed and the samples were analyzed via radioHPLC to determine the composition the agent. In both cases the samples showed the presence of intact ^{68}Ga-3b (Figure 4.3). I.t injection showed also a small peak at a short retention time, ascribable to dechelated ^{68}Ga, indicating a possible degradation of the metal complex *in vivo*. Although a worst resolution of the chromatogram due to the more diluted samples, no evidence of free ^{68}Ga was observed in the case of mice injected intravenously.

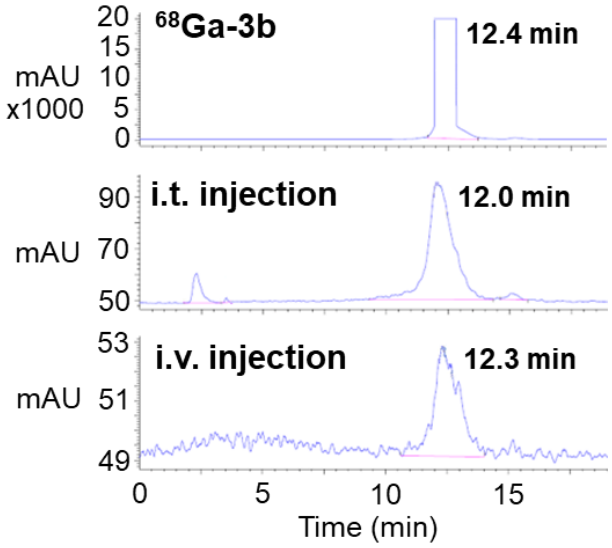

Figure 4.3. RadioHPLC chromatograms of tumor samples collected from two representative mice after intratumoral (i.t.) and intravenous (i.v.) injection with ^{68}Ga-3b, compared with pure ^{68}Ga-3b.

Based on the results of these promising preliminary studies on tumor uptake, it was decided to test ^{68}Ga-3b as PET co-agent for the measurement of tumor pHe in murine models, via an intravenous injection (see section 4.2.3.1).

4.2.2.2 ^{86}Y-3b

4.2.2.2.1 Radiosynthesis and purification

The synthesis of ^{86}Y(III)-1-[(2'-(4-methoxyphenylsulfonaminoethyl]-4,7,-10-tris-[(4'-carboxy)-1'-carboxybutyl]-1,4,7,10-tetraazacyclododecane (^{86}Y-3b) was optimized by starting from the conditions found for ^{68}Ga-3b. The optimization of the radiolabeling led to obtain the best conditions with pH 6.5 and a value of [3b] = 0.1 mM in the final volume of reaction mixture (See Scheme 4.3).

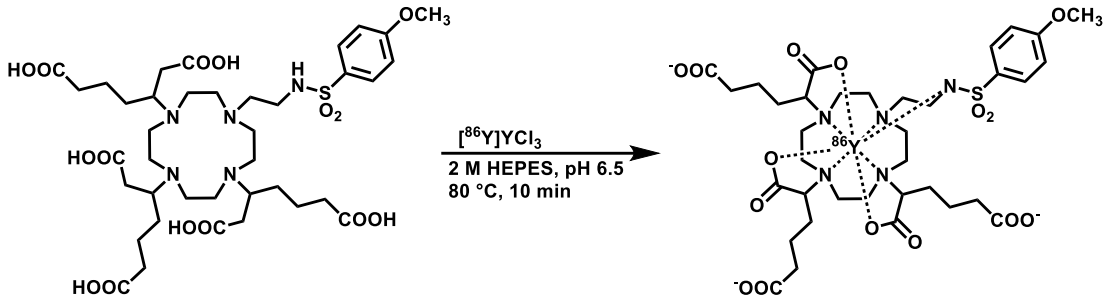

Scheme 4.3. Optimized conditions for the radiosynthesis of ^{86}Y-3b.

Reaction completion was confirmed via radioHPLC. The reaction mixture was loaded onto a pre-conditioned C18 cartridge and eluted with 1 mL of ethanol and divided in 5 fractions, to obtain the pure concentrated product (radioHPLC chromatogram shown in Figure 4.4).

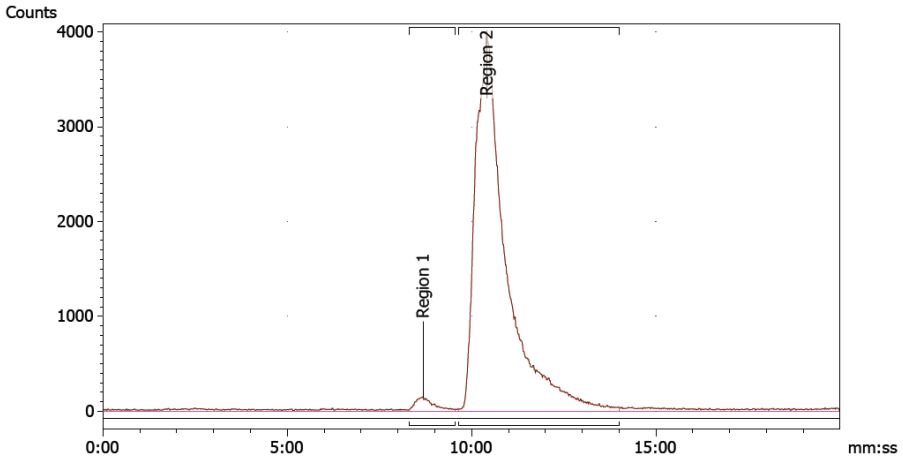

Regions: ^{68}Ga Detector: PMT

Name	Start (mm:ss)	End (mm:ss)	Retention (mm:ss)	Area (Counts)	%ROI (%)	%Total (%)
Region 1	8:18	9:33	8:41	4896	2.14	2.01
Region 2	9:39	14:00	10:25	223732	97.86	91.95
2 Peaks				228628	100.00	93.96

Total Area: 243321 Counts
Average Background: 0 Counts

Figure 4.4. RadioHPLC chromatogram of ^{86}Y-3b.

The optimization of synthesis and purification steps allowed to obtain the compound ^{86}Y-3b with the high radiochemical purity of 97.9%.
^{86}Ya-3b was then tested as PET co-agent for the measurement of tumor pHe in murine models, through simultaneous PET/MRI (see section 4.2.3.2).

4.2.3 *In vivo* PET/MRI for the measurement of tumor pHe

Two sets of *in vivo* PET/MRI experiments were done on mice bearing a subcutaneous flank PaCa-2 pancreatic tumor model. In the first test the ^{68}Ga-3b/Gd-3b co-agents pair was used, while the second one involved the ^{86}Y-3b/Gd-3b pair.

For both the experiments, the procedure for *in vivo* PET/MRI started with a baseline anatomical MR image and a T_1 map. A DCE MRI scan was then started, and the co-agents were injected i.v. simultaneously via a long catheter, in a known concentration ratio, into tumor bearing mice. Simultaneous DCE MRI and dynamic PET scan were then obtained. The change in R_1 relaxation rate can be determined from the MR images, while the concentration of the MRI co-agent can be calculated from the PET image via the known injected ratio of the two agents. These values can then be used to calculate relaxivity in various time frames over the dynamic PET/MRI scan. Once the curve reaches a steady value, the average relaxivity can be used to calculate tumor pHe, by using the equation of the r_1 vs. pH curve.

4.2.3.1 *In vivo* PET/MRI with ^{68}Ga-3b/Gd-3b PET/MRI co-agents

5 mice bearing a subcutaneous PaCa-2 pancreatic tumor model were imaged twice, two days apart, while in the meantime they were kept with 200 mM sodium bicarbonate as drinking water to search for a tumor pHe variation in the second experiment. In fact, it was reported that oral bicarbonate can increase tumor pH.[88]

Each mouse was catheterized via their tail vein, and a 125 μL line was used to connect the needle to the syringe outside of the scanner. The line was filled with a 25 μL lead of saline followed by a 250 μL injection volume of the PET/MRI co-agents at a known ratio. 125 μL of saline was then used to completely flush the co-agents out of the line and into the mouse.

Unfortunately, none of the five mice tested showed uptake of the PET co-agent in the tumor, making thus impossible the data analysis to measure the concentration and then to extrapolate the pHe value of interest through the previously described method. A representative image of a mouse is shown in Figure 4.5.

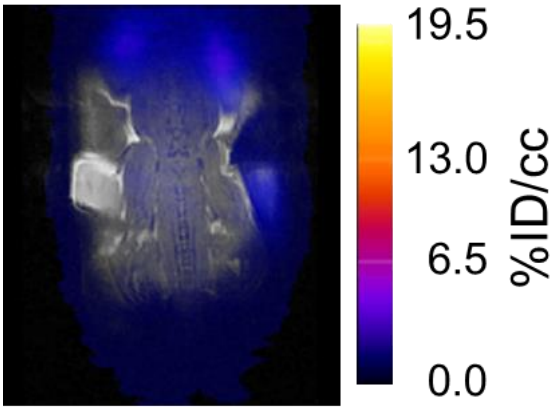

Figure 4.5. Representative PET/MRI image of a mouse injected with ^{68}Ga-3b/Gd-3b showing no uptake of the PET agent in the tumor. ID/cc: injected dose per cubic centimeter.

4.2.3.2 *In vivo* PET/MRI with ^{86}Y-3b/Gd-3b PET/MRI co-agents

2 mice bearing a subcutaneous PaCa-2 pancreatic tumor model were imaged twice, two days in a row, while in the meantime they were kept with 200 mM sodium bicarbonate as drinking

water to look for a possible pHe variation in the second day. The same steps described in the previous paragraph were followed.
As in the case of ^{68}Ga-3b, no evidence of uptake of the PET co-agent was observed in the tumor regions of the mice imaged and no further analysis was possible.

4.2.4 Evaluation of routes of administration

After the results regarding the poor tumor uptake in the *in vivo* PET/MRI trials, experiments to test the efficiency of the possible various routes of administration of PET agents were made. With the goal of finding the best way of administration, the tumor uptake of mice injected by different routes, with the same activity, was monitored.
In Figure 4.6, images of mice bearing a 4T1 tumor model injected with the same dose of Na^{18}F are shown, together with a graph indicating the tumor uptake found for the different routes of administration.

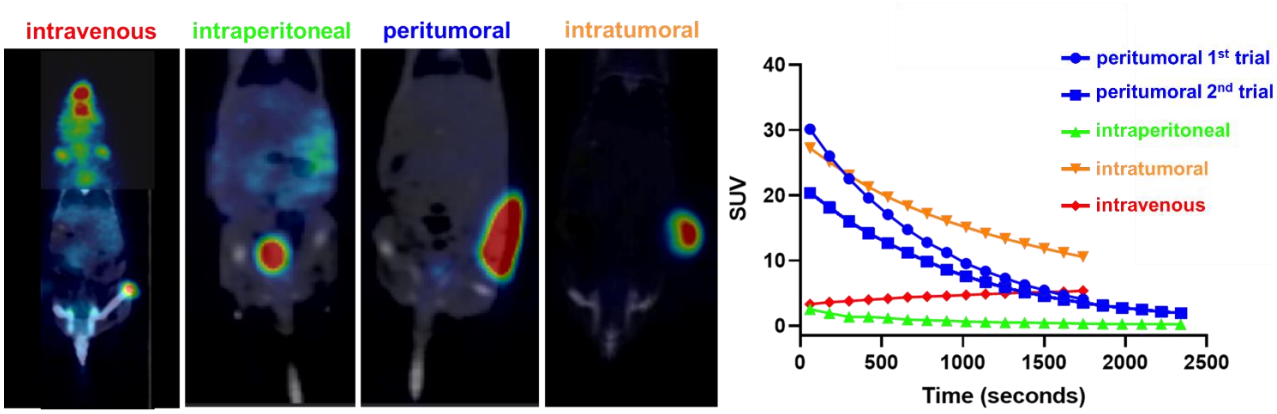

Figure 4.6. Images of tumor-bearing mice injected with the same activity of Na^{18}F through different routes of administration and graph showing the standardized uptake value (SUV) as a function of the time after injection. Values obtained by intravenous (red), intraperitoneal (green), peritumoral (blue) and intratumoral (orange) injections are displayed in the graph.

As it can be noted from the graph, intravenous and intraperitoneal routes showed the least uptake values in a time range of 30 min, indicating an expected low efficiency for these kind of studies. Intratumoral injection demonstrated an excellent amount of internalized PET tracer. Peritumoral injection, which is a subcutaneous injection in the proximity but not inside the tumor, also showed a good level of uptake, especially at short times after injection. Differently than intratumoral administration, peritumoral injection has the advantage to avoid potential damage or disruption of the tumor tissue.
Although also the type of PET agent can play a role in the level of tumor uptake, these preliminary experiments suggest that peritumoral injection can be considered the preferred route of administration for these PET/MRI studies.

4.3 Conclusion

The Gd-3b complex showed promising characteristics for its application as MRI co-agent in simultaneous PET/MRI for measuring pHe. The wide range relaxivity values it can exhibit (from 2.2 to 12.2 $mM^{-1} s^{-1}$, at 7 T) varies with the degree of protonation of its sulfonamide arm and thus it is expected to guarantee very sensitive pH measurement. Being its pKa 7.09 it is particularly suitable for measuring the extracellular microenvironment both in normal cells (pHe > 7.0) and in tumor cells (pHe < 7.0), potentially discriminating between healthy and cancer tissues.

The novel ^{68}Ga-3b and ^{86}Y-3b complexes were synthesized with high purity and tested *in vivo* as PET co-agents. Unfortunately, both PET/MRI experiments showed no evidence of tumor uptake, although preliminary pharmacokinetic studies showed evidence of ^{68}Ga-3b internalization in tumors both when administered intratumorally and intravenously.

By analogy with the previous work and due to the easier accessibility and relative inexpensiveness of ^{68}Ga radioisotope, most of the investigation was focused on ^{68}Ga-3b as PET co-agent. However, ^{86}Y-3b doubtless represent the most promising candidate for the herein application. One reason is that Y(III) ion is more structurally similar to Gd(III) ion than Ga(III) ion. In fact, a major assumption of this PET/MRI approach is that the PET and MRI co-agents are delivered to the tumor in the same ratio as in the injection volume. Although all the three cations have in common the same charge, the effective ionic radii of yttrium and gadolinium are rather similar (90 pm and 93.5 pm, respectively), unlike gallium (62 pm).[97] Also, different than gallium, yttrium has a coordination chemistry similar to that of lanthanides.[98] Another reason for the expected preference for ^{86}Y-3b in PET/MRI applications is the longer half-life of the ^{86}Y radioisotope ($t_{1/2}$ = 14.7 h), with respect to the short ^{68}Ga half-life ($t_{1/2}$ = 68 min). Indeed, the use of ^{86}Y for *in vivo* PET/MRI guarantees an advantage in terms of the potential use of this kind of measurement in clinics, since the PET co-agent could be prepared and shipped overnight.

In summary, although the *in vivo* studies were not successful, an improved MRI co-agent and two novel PET co-agents were synthesized with high purity and were preliminary tested. Investigations are currently ongoing to check the behavior of these new co-agents pairs via peritumoral injection, as suggested by the more recent studies. Furthermore, other versions of these probes under intense scrutiny.

4.4 Experimental section

All solvents and reagents were purchased from commercial sources and used as received. pH of solutions was recorded using a SevenCompact S221 benchtop pH/ion meter (Mettler Toledo, Columbus, OH). Ultra-performance liquid chromatography-mass spectrometry/mass spectrometry (UPLC-MS/MS) was performed using a Waters Xevo TQD IVD with Acquity UPLC using an Acquity UPLC BEH C18 1.7 μm column with 2.1 x 50 mm dimensions

(Waters, Milford, MA). Concentration of Gd-solutions was determined by the relaxometric preaviously reported method (see 2.5.2 section for details).[50]

RadioHPLC was performed on an analytical Agilent 1260 Infinity II Series (Agilent Technologies, Santa Clara, CA) with a XBridge C18 3.5 μm column with 4.6 x 250 mm dimensions using a Flow-RAM radioHPLC detector (LabLogic Systems Ltd., Brandon, FL) for compound identification and quality control. For metabolism studies, an analytical Agilent 1100 Series system (Agilent Technologies, Santa Clara, CA) was used with an Econosil 10 μm column with 4.6 x 250 mm dimensions (Alltech, Nicholasville, KY). Counts were detected using a Bioscan Model 106 detector (Bioscan, Inc., Poway, CA) interfaced with the HPLC using an Agilent Interface 35900E (Agilent Technologies, Santa Clara, CA). Purification with a C18 cartridge was performed using a light C18 Sep Pak® cartridge (Waters, Milford, MA) prewashed with ethanol (3 mL) and water (6 mL). HPLC was performed using one of the following solvent systems: 0.1% TFA in water (solvent A) and 0.1% TFA in acetonitrile (solvent B); or 0.05% formic acid in water (solvent C) and 0.05% formic acid in acetonitrile (solvent D). For prep HPLC, the following method was used: 5% solvent B (in solvent A) to 95% solvent B (in solvent A) over 34 min then hold at 95% solvent B (in solvent A) for 3 min with a 20 mL/min flow rate. For analytical HPLC, the following method was used: 5% solvent D (in solvent C) to 95% solvent D (in solvent C) over 15 min with a 1 mL/min flow rate.

[^{68}Ga]$GaCl_3$ ($t_{1/2}$ = 68 min) was produced from a 1.85 GBq capacity GalliaPharm® ^{68}Ge/^{68}Ga Radionuclide Generator (Eckert & Ziegler Radiopharma GmbH, Berlin, Germany) in the Cyclotron Radiochemistry Facility at the MD Anderson Cancer Center. [^{86}Y]YCl_3 ($t_{1/2}$ = 14.7 h) was ordered and delivered from the Cyclotron Research Group in the Department of Medical Physics of the University of Wisconsin-Madison.

4.4.1 Synthesis

4.4.1 Gd-3b

The synthesis of Gd(III) 1-[(2'-(4-methoxyphenylsulfonaminoethyl]-4,7,-10-tris-[(4'-carboxy)-1'-carboxybutyl]-1,4,7,10-tetraazacyclododecane (Gd-3b) was made by following the reported procedure.[47] LRMS (ESI): (*m*/*z*): [M - H]$^-$ calcd for $C_{35}H_{51}N_5O_{15}S_1Gd_1$, 971.23; found, 971.46.

4.4.1 Radiosynthesis of ^{68}Ga-3b

6 mL of 0.37% HCl was added to 5 mL (36 mCi) of [^{68}Ga]$GaCl_3$ in 0.1 M HCl and loaded onto a cartridge packed with UTEVA Resin 100-150 μM. The eluition with 1 mL of HCl 0.1 M led to a [^{68}Ga]$GaCl_3$concentrated solution of 21 mCi. 7 mCi (about 450 μL) of the concentrated solution was added to 350 μL of 3 M HEPES buffer at pH 8. Then 20 μL of 1-[(2'-(4-methoxyphenylsulfonaminoethyl]-4,7,-10-tris-[(4'-carboxy)-1'-carboxybutyl]-1,4,7,10-tetraazacyclododecane (3b) (2 mg/mL solution in water) was added, the pH was adjusted to 5, and the reaction was heated to 80 °C for 10 minutes. Reaction completion was confirmed with radioHPLC. The reaction mixture was loaded onto a pre-conditioned C18 cartridge and eluted with 1 mL of a ethanol divided in 200 μL fractions to concentrate the solution.

4.4.2 Radiosynthesis of ^{86}Y-3b

651 μCi (100 μL) of [^{86}Y]$GaCl_3$ in 0.1 M HCl was added to 50 μL of 2 M HEPES buffer at pH 7.3. Then 20 μL of 1-[(2'-(4-methoxyphenylsulfonaminoethyl]-4,7,-10-tris-[(4'-carboxy)-1'-carboxybutyl]-1,4,7,10-tetraazacyclododecane (3b) (2 mg/mL solution in water) was added, the was pH adjusted to 6.5, and the reaction was heated to 80 °C for 10 minutes. Reaction completion was confirmed with radioHPLC. The reaction mixture was loaded onto a pre-conditioned C18 cartridge and eluted with 1 mL of a ethanol divided in 200 μL fractions to concentrate the solution.

4.4.2 MR Imaging

Tubes for the pH-relaxivity calibration curve were imaged using a 7 T MR scanner with a 30 cm horizontal bore equipped with 20 cm fixed gradients and Avance HD architecture (Bruker, Billerica, MA). A 72 mm Bruker MRI coil was used. The following two MRI sequences were used for the imaging experiment: 1) 2D coronal rapid acquisition with relaxation enhancement with variable repetition time (RAREVTR) (TE = 21.68 ms, 12 TR = 300, 583.697, 897.052, 1246.995, 1643.217, 2099.848, 2638.683, 3295.960, 4138.860, 5315.362, 7278.213, 15000 ms, RARE factor = 8, echo spacing = 5.420 ms, 16 dummy scans, 1 average, 1 repetition, 1 slice, slice thickness = 1 mm, 100 x 100 mm FOV, 128 x 128 matrix, 0.781 x 0.781 mm resolution); 2) 2D RAREVTR (TE = 21.68 ms, 12 TR = 150, 244.528, 348.933, 465.522, 597.522, 749. 633, 929.107, 1147.994, 1428.622, 1820.126, 2472.524, 5000 ms, RARE factor = 8, echo spacing = 5.420 ms, 16 dummy scans, 1 average, 1 repetition, 1 slice, slice thickness = 1 mm, 100 x 100 mm FOV, 128 x 128 matrix, 0.781 x 0.781 mm resolution). MR images were reconstructed, and T_1 times were calculated using ParaVision 6 (Bruker, Billerica, MA).

4.4.3 pH-relaxivity calibration curve

To obtain a pH-relaxivity calibration curve, a matrix of samples containing Gd-3b in pure water were prepared at different concentrations of (0, 0.2, 0.4, and 0.6 mM) and pH values from 4.16 to 11.35. Each sample was prepared in a PCR tube of 200 μL volume. Concentrations were determined by the relaxometric method described above and confirmed using ICP-MS. pH values were confirmed using a calibrated pH meter. Samples were arranged in a small box filled with 2% agarose designed to hold 30 samples and fit into a Bruker 72 mm MRI coil. T_1 times were then converted to relaxation rates. The measured relaxation rates were plotted versus concentration, and the slope of the line was used to determine relaxivity for each pH value (data not shown). Relaxivity was then plotted versus pH value to produce a pH-relaxivity calibration curve. This data was fit to a modified Henderson-Hasselbach equation:

$$pH = pKa + log\left(\frac{r_1 - a}{b - r_1}\right)$$

pKa is the pKa of the sulfonamide arm on the MRI co-agent, r_1 is the relaxivity of the measured sample, *b* is the relaxivity when compound is completely deprotonated, and *a* is the relaxivity when the compound is completely protonated.

4.4.4 PET/MR imaging, reconstruction and analysis

All scans were performed on a Bruker 7 T MRI (Bruker, Billerica, MA) with a Cubresa NuPET™ insert (Cubresa, Inc., Winnipeg, MB). A 35 mm Bruker MRI coil was used. For PET/MRI studies in tubes, the two MRI acquisitions described above were obtained (except a FOV of 38.4 x 38.4 mm was used for a resolution of 0.300 x 0.300 mm) during a simultaneous 30 min PET scan. The ratio of the PET and MRI co-agent in the tube was measured prior to scanning and decay-corrected to the start of the scan. The amount of PET co-agent was measured using a CRC-15R dose calibrator (Capintec, Inc., Florham Park, NJ, USA). MRI reconstructions were performed using ParaVision 6 (Bruker, Billerica, MA). T_1 times were also calculated using ParaVision 6. Scatter, randoms, and decay corrections for PET images were applied through the Cubresa software. PET reconstructions were performed using an Ordered Subset Maximum a Posteriori One Step Late algorithm with 8 iterations and 4 subsets, and PET images were quantified using a Quantification Calibration Factor for ^{68}Ga or ^{86}Y. PET VOIs and representative images were generated and analyzed using VivoQuant (inviCRO, LLC, Boston, MA).

For *in vivo* PET/MRI studies, mice were placed on a sled fitted with a nose cone allowing the mice to be anesthetized with 2% isoflurane using oxygen as a carrier throughout the imaging experiment. A heated water pad under the mouse and a temperature-controlled hose that delivered warm air to the mouse (SA Instruments, Stony Brook, NY) were used to maintain mouse temperature at 37 °C. The breathing rate was monitored throughout the experiment. The following MRI acquisitions were obtained for all *in vivo* imaging sessions: 1) a localizer image to ensure proper placement of the mouse in the PET/MRI system; 2) pre-injection 2D coronal RARE (TE = 43.99 ms, TR = 1200 ms, RARE factor = 8, echo spacing = 5.499 ms, 2 dummy scans, 2 averages, 1 repetition, 9 slices, slice thickness = 1 mm, 58.8 x 38.4 mm FOV, 196 x 128 matrix, 0.300 x 0.300 mm); 3) 2D coronal RAREVTR (TE = 27.12 ms, 6 TR = 500, 650, 1000, 1500, 2500, 5000 ms, RARE factor = 8, echo spacing = 6.78 ms, 2 dummy scans, 2 averages, 1 repetition, 9 slices, slice thickness = 1 mm, 58.8 x 38.4 mm FOV, 196 x 128 matrix, 0.300 x 0.300 mm); 4) 2D coronal dynamic contrast enhancement fast low angle shot (DCE FLASH) (TE = 2.03 ms, TR = 59.462 ms, flip angle = 35 °, 1 average, 130 repetitions, 9 slices, slice thickness = 1 mm, 58.8 x 38.4 mm FOV, 196 x 128 matrix, 0.300 x 0.300 mm); 5) post-injection 2D coronal RARE (TE = 43.99 ms, TR = 1200 ms, RARE factor = 8, echo spacing = 5.499 ms, 2 dummy scans, 2 averages, 1 repetition, 9 slices, slice thickness = 1 mm, 58.8 x 38.4 mm FOV, 196 x 128 matrix, 0.300 x 0.300 mm). Mice were catheterized via their tail vein, and a 125 μL line was used to connect the needle to the syringe located outside of the scanner. This line was filled with a 25 μL lead of saline followed by a 250 μL injection volume of the PET/MRI co-agents (which completely filled the line and partially filled the syringe). The mice were injected with both co-agents simultaneously on the scanner at the beginning of

the DCE MRI scan. 125 μL of saline was then used to completely flush the co-agents out of the line and into the mouse, so the mice received a total injection volume of 275 μL. The dynamic PET scan was obtained simultaneously with the DCE MRI scan.

The ratio of the PET and MRI co-agent in the syringe was measured prior to injection and decay-corrected to the start of the scan. The actual injected dose of the PET co-agent was calculated by measuring the pre- and post-injection activity in the syringe using a CRC-15R dose calibrator (Capintec, Inc., Florham Park, NJ, USA). It was assumed that percent loss of the PET and MRI co-agents in the syringe was equal. The actual injected concentration of the MRI co-agent was confirmed using ICP-MS.

Scatter, randoms, and decay corrections for PET images were applied through the Cubresa software. For dynamic PET analysis, data were binned into 2 min time frames over the 16 min dynamic scan. To produce static images, data were binned over the entire 16 min PET scan. PET reconstructions were performed using an Ordered Subset Maximum a Posteriori One Step Late algorithm with 8 iterations and 4 subsets, and PET images were quantified using a Quantification Calibration Factor for ^{68}Ga or ^{86}Y. MRI reconstructions were performed using ParaVision 6 (Bruker, Billerica, MA). PET/MR image registration was manually performed using the pre-injection MR image and VivoQuant (inviCRO, LLC, Boston, MA). PET VOIs and representative PET/MR images were also generated and analyzed using VivoQuant. Injected doses were used to calculate percent of injected dose per cubic centimeter of tissue (%ID/cc). Errors in the averaged %ID/cc were reported as standard deviation. MRI RAREVTR and DCE data were analyzed using Matlab R2021b (MathWorks, Natick, MA).

4.4.5 Animal handling

MIA PaCa-2 pancreatic tumor cells were grown in Dulbecco's Modified Eagle Medium (DMEM) media (10-017-CV, Corning, Inc., Corning, NY) with 10% FBS in a T75 flask. All mouse experiments were approved by the University of Texas MD Anderson Cancer Center (MDACC). Female athymic nude mice were obtained from the MDACC Experimental Radiation Oncology (ERO) mouse colony. Subcutaneous tumor models were generated by subcutaneous injection of 50 μl of phosphate buffered saline containing 1.5 million MIA PaCa-2 cells and 50 μl of Matrigel (354234, Corning, Inc., Corning, NY).

Chapter 5

Fe(deferasirox)$_2$: An iron(III)-based MRI T_1 contrast agent endowed with remarkable molecular and functional characteristics

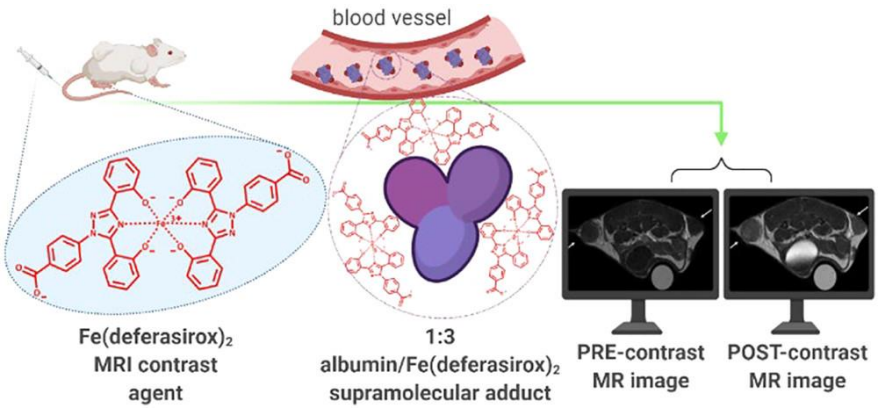

5.1 Introduction

Deferasirox (DFX) is an iron sequestering agent used for the treatment of thalassemic patients encountering iron overload, and it holds a prominent position among available treatment options.[99–101] It is administered orally and easily enters the bloodstream, where it tightly binds to human serum albumin (HSA). Upon its long circulation lifetime, DFX efficiently chelates the Fe^{3+} ions in excess in the anatomical regions where it is distributed, facilitated by the formation of a hexacoordinated Fe(III) complex involving two ligand units (chemical structure in Chart 5.1).

Chart 5.1. Chemical structure of the complex $Fe(DFX)_2$

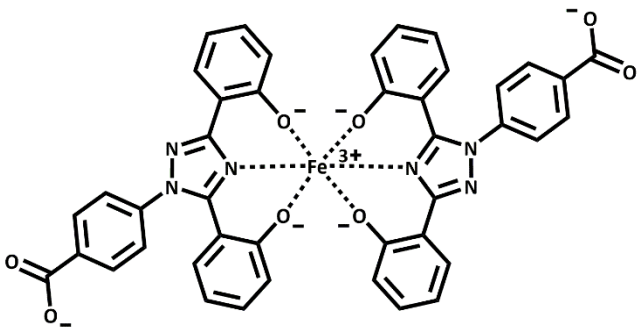

The inner coordination sphere of $Fe(DFX)_2$ displays four negatively charged oxygen atoms, offering potential sites for the set-up of hydrogen-bonded water molecules in the second coordination sphere. It is noteworthy that the Fe-H distance for these hydrogen-bonded water molecules in the second sphere is expected to be only marginally longer than that observed for protons in an inner sphere water molecule.

The $Fe(DFX)_2$ complex has been reported to be endowed with extremely high thermodynamic stability ($\log \beta = 38.6$)[102], and excretion predominantly occurs via the hepatobiliary route, with a lesser contribution from the renal route.[103,104] As shown by previously reported speciation diagrams, at physiological pH, only the $Fe(DFX)_2$ bis complex is present.[105]

Although a number of papers describing different aspects of both DFX and $Fe(DFX)_2$ can be found in literature, the relaxometric properties of the metal complex as a potential MRI contrast agent where never investigated before.

Analogously to the ligand, the metal complex also exhibits strong affinity for HSA.[106,107] Such property is particularly interesting for the intended application, as the formation of a supramolecular adduct may allow the exploitation of the relatively long electronic relaxation time of the Fe^{3+} ion, resulting in a highly effective contrast agent with enhanced relaxivity.

Herein, the *in vitro* and *in vivo* relaxometric, imaging and biodistribution studies on $Fe(DFX)_2$ are reported.

5.2 Results

The three negatively charged $[Fe(deferasirox)_2]^{3-}$ complex is easily formed by mixing 1:2 amounts of $FeCl_3$ and deferasirox (4-[(3,5-bis-(2-idroxyphenyl)-1,2,4)triazol-1-yl]-benzoic acid, DFX), as described in the experimental section. To improve the aqueous solubility, its salt with meglumine (*N*-methyl-glucamine, MGL) as counter ion was prepared ($[Fe(DFX)_2]MGL_3$). Such compound was used for all the *in vitro* and *in vivo* experiments, and it is simply reported as $Fe(deferasirox)_2$ or $Fe(DFX)_2$.

5.2.1 *In vitro* relaxometric investigations

The relaxivity (r_1 and r_2) values measured at 298 K and 310 K, at 0.47 and 1 T, in water and in human serum, are reported in Table 5.1.

Table 5.1. Longitudinal and transverse relaxivities of $Fe(DFX)_2$

Medium	Field	T (K)	r_1 ($mM^{-1} s^{-1}$)	r_2 ($mM^{-1} s^{-1}$)
Water	0.47 T	298	2.5 ± 0.31	2.9 ± 0.29
		310	1.7 ± 0.20	2.5 ± 0.22
	1 T	298	2.3 ± 0.22	3.1 ± 0.34
		310	1.4 ± 0.18	2.4 ± 0.21
Human serum	0.47 T	298	3.4 ± 0.32	5.4 ± 0.35
		310	3.1 ± 0.25	5.1 ± 0.41
	1 T	298	4.4 ± 0.33	6.3 ± 0.29
		310	4.1 ± 0.41	6.6 ± 0.42

Data measured at $[Fe^{3+}]$ = 1 mM, in water and in human serum, at 298 K and 310 K, at 0.47 T and 1 T, at pH 7.4.

The observed relaxivities remained constant over several days when the solutions were maintained at 310 K. The relaxivity of $Fe(DFX)_2$ was constant over the pH range 6-10. Moreover, our observations demonstrated a decrease in relaxivities as the temperature increased, indicating that the r_1 values were not affected by a slow exchange of the involved protons, and ruling out the possibility of "quenching" effects.

The absence of any contribution to the observed relaxivity arising from inner sphere water molecules coordinated to Fe(III) ion was assessed by carrying out the variable-temperature ^{17}O-R_2-NMR experiment, in analogy to what firstly proposed by Snyder et al.[36] It is clear that $Fe(DFX)_2$ behaves as a $q = 0$ system as it can be appreciated in Figure 5.1, where the ^{17}O-R_2-NMR data obtained at 14.1 T for a 20 mM solution of $Fe(DFX)_2$ are compared with those measured for two well-known complexes with $q = 1$ (Fe(CDTA)) and $q = 0$ (Fe(DTPA)).

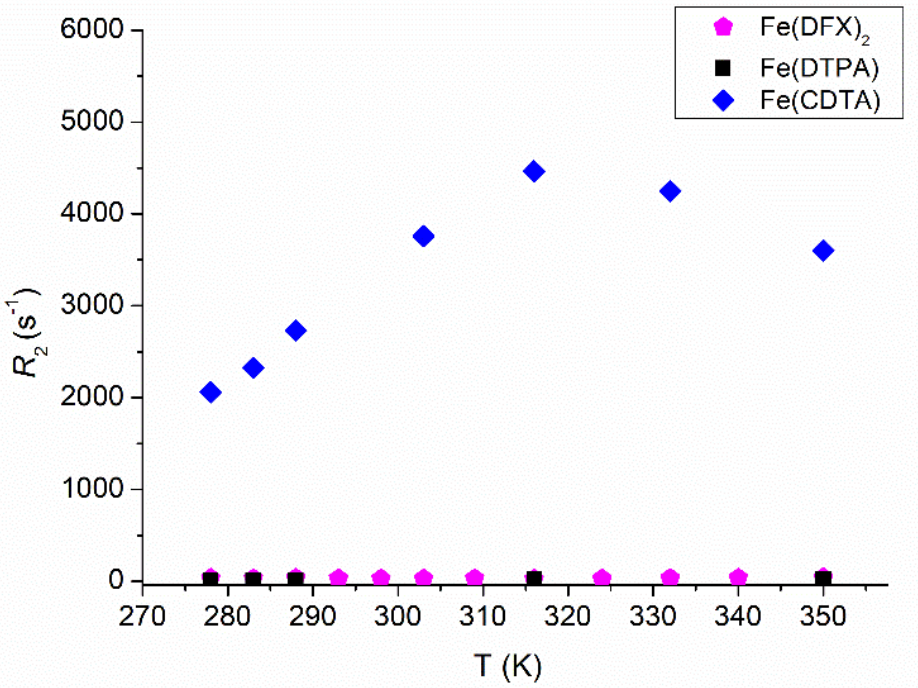

Figure 5.1. Comparison between $Fe(DFX)_2$, Fe(DTPA) and Fe(CDTA) ^{17}O-transverse relaxation rate measured as a function of temperature at 14.1 T and pH 7.4. Data are normalized to 20 mM iron concentration.

By evaluating the NMRD profiles on a fast field cycling (FFC) relaxometer, additional understanding of the impact of the applied magnetic field strength on the measured longitudinal and transverse relaxivities was achieved.

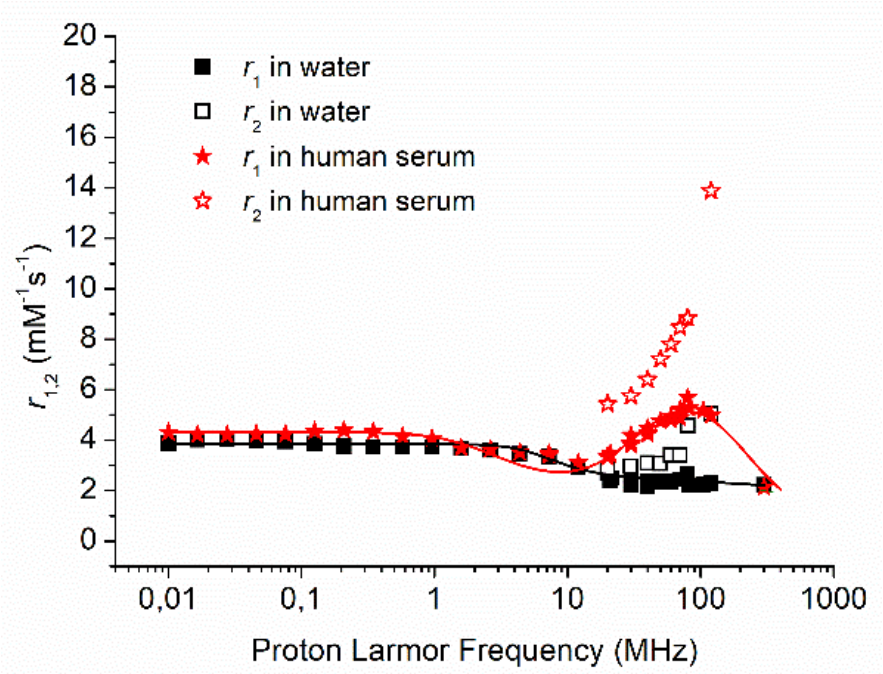

Figure 5.2. r_1 and r_2 NMRD profiles of $Fe(DFX)_2$ in water (black) and human serum (red) at 298 K and pH 7.4. Data are normalized to 1 mM iron concentration.

The experimental relaxivity data were fitted by using Solomon-Bloembergen-Morgan (SBM) theory of paramagnetic relaxation.[108–110] Although such theory is generally accepted for Gd and Mn complexes, a limited number of papers with fitted NMRD profiles of iron-based complexes can be found in literature.[111–114] More recently, a systematic investigation about the relaxometric properties of Fe(III)-EDTA derivatives, which sizes are very similar to $Fe(DFX)_2$, further supported the applicability of SBM theory for the fitting of $Fe(DFX)_2$ NMRD profiles.[33] From the fitting of the the experimental data it was possible to extract the relevant parameters responsible for the observed behavior (Table 5.2). The following parameters were fixed during the fitting procedure: q^{is} (number of inner sphere water molecules) = 0; D (solute-solvent diffusion coefficient) = 2.24 10^{-5} cm^2 s^{-1}; r_{FeH}^{ss} (distance between Fe^{3+} ion and protons of the second sphere water molecules) = 3.48 Å (calculated as follows: Fe-O average bond length from crystal structure = 1.98 Å[105] + O-H strong hydrogen bond = 1.5 Å[115]).

The number of exchanging protons that transfer the relaxation enhancement to the bulk water protons represents a key determinant. In the case of paramagnetic complexes with $q = 0$ this role is ascribed to mobile protons present on the ligand or, more commonly, to the water molecules in the second coordination sphere. In $Fe(DFX)_2$ no labile protons are present on the ligand and, therefore, the analysis of the NMRD profile in water was based, as far as concerns this term, to the occurrence of water molecules in the second coordination sphere (specifically 4 protons from 4 water molecules hydrogen bonded to the coordinating negatively charged oxygens on DFX ligands). This assumption is certainly valid in water but, in the case of the experiment in serum, one may not rule out the contribution from exchanging protons on HSA at the binding interaction sites of $Fe(DFX)_2$.

Table 5.2. Relaxometric parameters obtained for the complex $Fe(DFX)_2$ from the fitting of the NMRD data acquired at 298 K.

	Water	**H. Serum**
Δ^2 (10^{20} s^{-2}) [a]	**1.01 ± 0.2**	**1.10 ± 0.1**
τ_V (ps) [b]	**24.7 ± 2.1**	**13.3 ± 0.9**
T_{1e} (ps) [c]	**70 ± 9.1**	**284 ± 22**
n^{ss} [d]	**4**	**2**
τ_C^{SS} (ps) [e]	**74 ± 0.49**	**850 ± 53**

[a] Squared mean transient zero-field splitting (ZFS) energy; [b] Correlation time for the collision-related modulation of the ZFS Hamiltonian; [c] Longitudinal electronic relaxation time at 0.47 T; [d] Number of second sphere exchanging protons; [e] Correlation time for the modulation of the dipolar interaction of the second coordination sphere water molecules (exchange and/or rotation).

The obtained molecular correlation time (τ_c^{SS}) associated to second sphere water molecules or paramagnetically relaxed mobile protons on HSA reports on the modulation of the involved paramagnetic interaction. For $Fe(DFX)_2$ in water the fitting yielded a τ_c^{SS} value of 74 ps, i.e. a value consistent either with the molecular reorientational time expected for complexes of this molecular weight or with the lifetime of H-bonded water molecules on the complex surface.[116] Likely, an interplay of the two correlation times takes place. When we calculated the NMRD

profile in serum by using the value of 30 ns for the reorientational time of HSA (the complexes are tightly bound to the protein), the shape of the resulting profile was not consistent with the experimental one, as the relaxivity peak was much sharper. We conceived that the broad hump shown by $Fe(DFX)_2$ in the high field region was mainly determined, in addition to the elongated τ_R, by contributions to τ_c^{SS} arising from an interplay between the electronic relaxation time and the exchange lifetime of the second sphere water molecules. The latter exchange process is still fast on the NMR time scale as the relaxivity decreases upon increasing the temperature.

In serum, the fitting of the experimental to the calculated NMRD values suggested the occurrence of two H in the second coordination sphere (i.e. two hydrogen bonded water molecules) and a τ_c^{SS} approaching the ns range (more than one order of magnitude longer than the value in water). The marked increase in r_1 from 0.5 to 2 T observed in serum appears to be associated with the long τ_c^{SS}, thus making the change in T_{1e} the determinant of the observed relaxivity. Only at about 2 T, when T_{1e} (that it is known to increase with the magnetic field) becomes longer than calculated τ_c^{SS}, the observed relaxivity is determined by the latter parameter.

To investigate the binding strength to human serum albumin, two sets of experiments were conducted. In the first experiment (Figure 5.3A), we measured the relaxation enhancement of a PBS solution of $Fe(DFX)_2$ upon the addition of increasing amounts protein. The results showed a notable increase in relaxation enhancement with each addition of HSA. In the second experiment (Figure 5.3B), we determined the number of binding sites on HSA by measuring the observed relaxation rate while keeping the HSA concentration fixed and increasing the concentration of the paramagnetic complex. The data revealed an inflection point in the graph, indicating the ratio between $Fe(DFX)_2$ and HSA at which the protein becomes saturated by the paramagnetic complex. This point provided direct evidence for the number of binding sites. The analysis of the experimental data indicated that three units of $Fe(DFX)_2$ bind to one molecule of HSA with extremely high affinity, as the inflection point occurred at [HSA] = 0.6 mM and $[Fe(DFX)_2]$ = 1.8 mM. Notably, the titration shown in Figure 5.3A demonstrated that the initial aliquots of HSA bound almost quantitatively to the complex. The further increase in R_1 at higher HSA concentrations reflected the diamagnetic contribution to relaxation from the protein itself, along with an overall increase in viscosity.

Furthermore, we applied the proton relaxation enhancement (PRE) equations (see Experimental Section) to fit the experimental data. As a result, for the three binding sites, we obtained an average apparent binding constant (K_a) of 2.8×10^5 M^{-1} and a relaxivity of the HSA-bound complex (r_1^b) of 3.8 mM^{-1} s^{-1} at 0.47 T and 298 K.

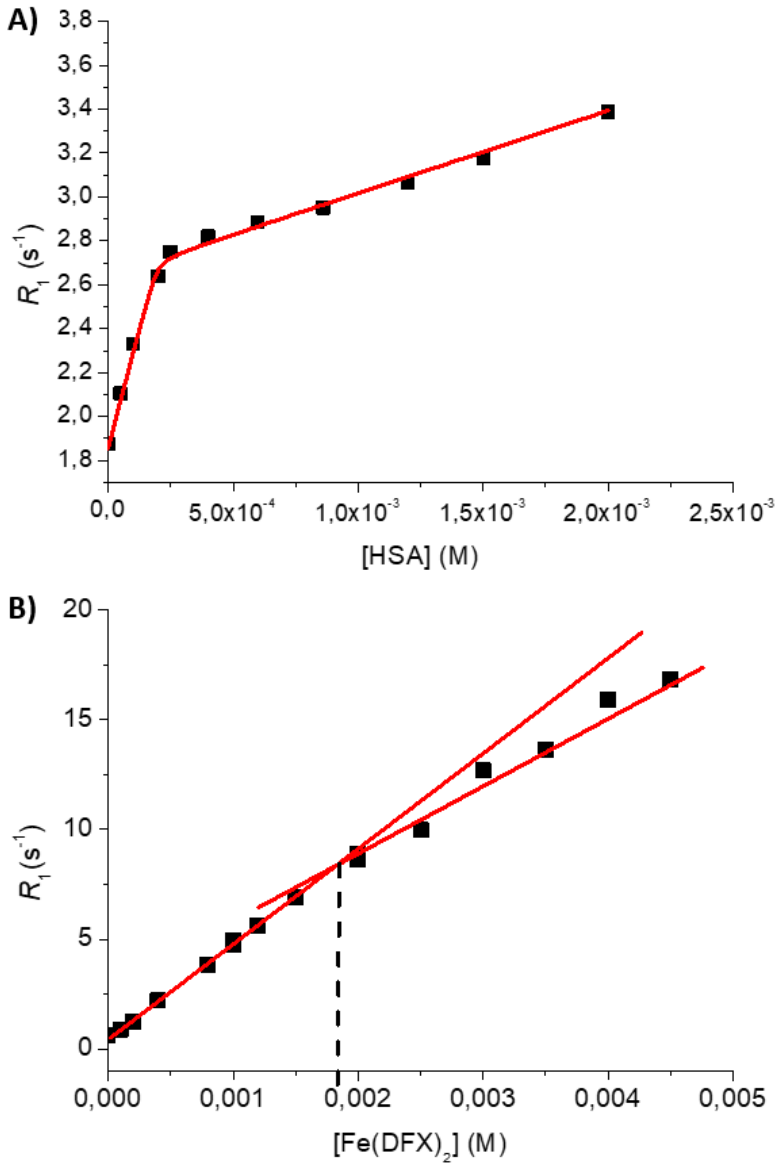

Figure 5.3. A) Proton relaxation enhancement (PRE) titration of $Fe(DFX)_2$ (0.56 mM) with increasing concentrations of HSA, in phosphate buffer, 298 K, 0.47 T. The curve is the best fit of the experimental data. **B**) PRE titration of HSA (0.6 mM) with increasing concentrations of $Fe(DFX)_2$, in phosphate buffer, 298 K, 0.47 T. The lines are the best linear fit of the experimental data at [CA] < 1.8 mM and [CA] > 1.8.

Further insights into the characterization of the binding sites were acquired by conducting relaxometric experiments in the presence of competitive ligands with well-known recognition abilities for specific binding sites on HSA (Figure 5.4).[117–120] The inhibitors used for each binding site were ibuprofen for subdomain IIIA (Sudlow site II), warfarin and iodipamide for subdomain IIA (Sudlow site I), and methyl orange for subdomain IB, respectively. Notably, subdomain IIA (Sudlow site I) was tested with both warfarin and iodipamide as inhibitors. The reason for using two inhibitors for subdomain IIA is based on previous studies involving a HSA-binding Gd-complex, which suggested that warfarin and the paramagnetic complex could potentially bind simultaneously due to the large size of the binding site. In contrast, iodipamide,

being larger in size, could displace the Gd(III) complex, leading to the need for two inhibitors in the experiment.[121]

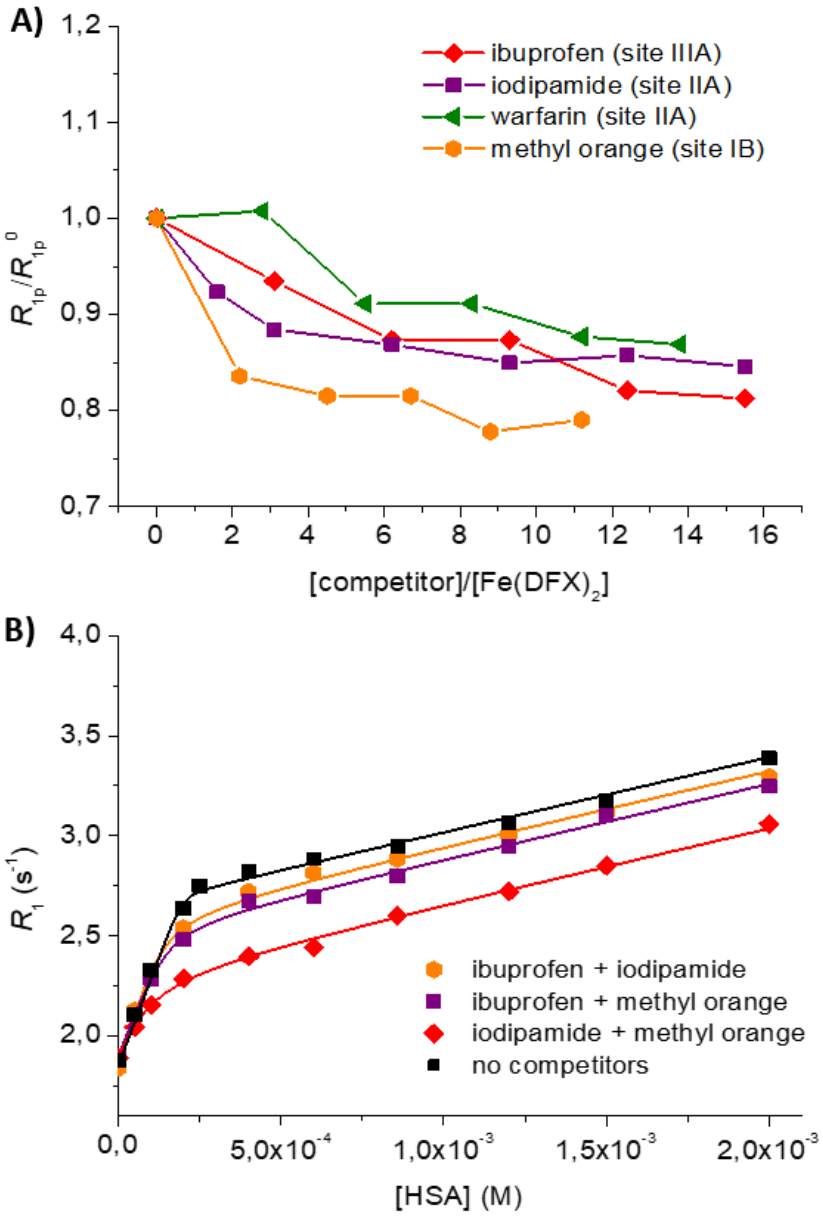

Figure 5.4. **A)** Displacement of $Fe(DFX)_2$ from HSA as determined by the change in relaxivity as function of increasing concentration of the added competitors relative to the respective binding site on HSA. (298 K, 0.47 T, $[Fe(DFX)_2]$=0.6 mM, [HSA]=0.2 mM in phosphate buffer). R_{1p}/R_{1p}^0 is the R_{1p} value of the solution normalized to the initial value (R_{1p}^0) without any inhibitor. $R_{1p}=R_{1obs}-R_{1d}$. **B)** Proton relaxation enhancement titration of $Fe(DFX)_2$ (0.56 mM in phosphate buffer) with increasing concentrations of HSA, in the presence of couples of competitors (as detailed in the legend) in 1.5:1 ratio with respect to HSA (298 K, 0.47 T).

The data shown in Figure 5.4A clearly indicate that all the used competitive ligands partially displace $Fe(DFX)_2$ from albumin. This confirms that the binding sites are located in the subdomains IB, IIA, and IIIA, consistent with the well-established description of albumin recognition properties. However, it is noteworthy that the asymptotic values at high concentrations of the competing ligands differ for the three sites. R_1 is the lowest for methyl

orange (IB), while the replacement of $Fe(DFX)_2$ at site IIA by warfarin or iodipamide, and at site IIIA by ibuprofen, yielded similar and higher R_1 values.

Next, to estimate the association constants of $Fe(DFX)_2$ for each albumin binding site, supplemental titrations were conducted. In such titrations, increasing concentrations of albumin were added simultaneously with two of the competing drugs specific to different principal binding sites (in a 1.5 : 1 ratio with HSA), leaving only one site free for $Fe(DFX)_2$ interaction (Figure 5.4B). By fitting each of these profiles with the same PRE equations used in Figure 5.3A, the association constant (K_a) and the bound relaxivity (r_1^b) for the unoccupied binding site were calculated. The results obtained are as follows: site IB, $K_a = 7.1\times10^4$ M^{-1} and $r_1^b = 3.8$ $mM^{-1}s^{-1}$; site IIA, $K_a = 5.9\times10^4$ M^{-1} and $r_1^b = 3.5$ $mM^{-1}s^{-1}$; site IIIA, $K_a = 1.9\times10^4$ M^{-1} and $r_1^b = 3.2$ $mM^{-1}s^{-1}$.

Based on these experiments, it can be concluded that sites IB and IIA exhibit the strongest affinity for $Fe(DFX)_2$ binding on albumin, while a slightly lower affinity is observed for site IIIA. It is important to note that the K_a value determined in the absence of any competing drug (Figure 5.3A) is approximately 4-5 times higher than the averaged K_a values determined from the individual measurements for each binding site. This discrepancy can likely be attributed to the fact that the competitors were added in excess (1.5 times) with respect to albumin. While this was necessary to ensure complete occupation of the respective binding site, it may have introduced some unwanted effects in the determination of the K_a values.

The obtained values for the relaxivity of $Fe(DFX)_2$ bound to each of the three binding sites confirm the qualitative trend reported in Figure 5.4A, with the highest r_1^b observed for $Fe(DFX)_2$ bound to site IB, followed by sites IIA and IIIA, respectively.

5.2.2 *In vivo* imaging studies

T_1-weighted MR images were acquired on a 3 T scanner to evaluate the *in vivo* performance of $Fe(DFX)_2$ as MRI CA in comparison with the clinically used Gd(DTPA) (Magnevist, gadopentetate dimeglumine) on the same mouse models at the same dose of 0.1 mmol/kg. At 3 T, Gd(DTPA) displays an *in vitro* relaxivity value, in water, not much different from $Fe(DFX)_2$.[36]

The *in vivo* experiments were conducted on mice (n = 6) bearing a TS/A breast tumor xenograft. In Figure 5.5 representative MR T_1-weighted images of the TS/A-inoculated mouse pre- and post-contrast ($Fe(DFX)_2$ and Gd(DTPA) are reported. Details on the changes in signal intensities (SI) for the tumor regions and selected organs are provided in Figure 5.6. In general, it can be observed that the contrast enhancement behaviors exhibited by $Fe(DFX)_2$ and Gd(DTPA) were quite similar. Additionally, the wash-out kinetics, as indicated by the return of SI to pre-contrast values, were also found to be relatively comparable between the two contrast agents.

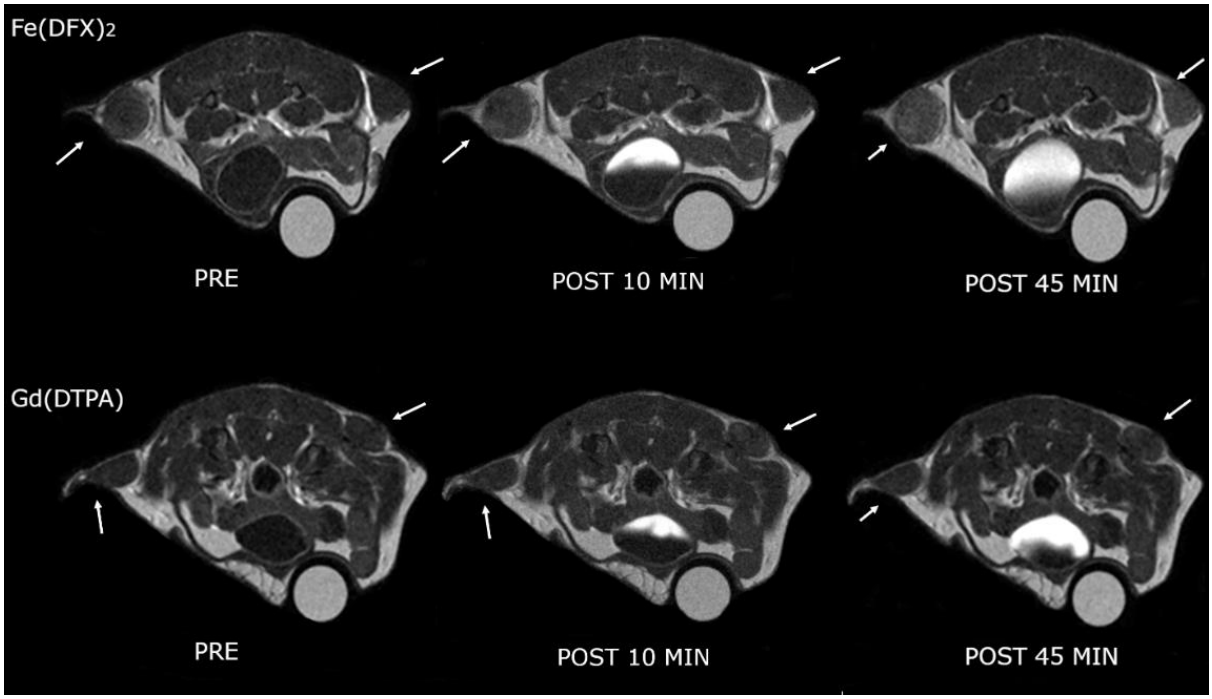

Figure 5.5. Representative MR T_1-weighted images of the TS/A-inoculated mouse pre- and post- (10 or 45 minutes) contrast agent administration ($Fe(DFX)_2$ and Gd(DTPA), 0.1 mmol/kg). The arrows indicate the tumor regions.

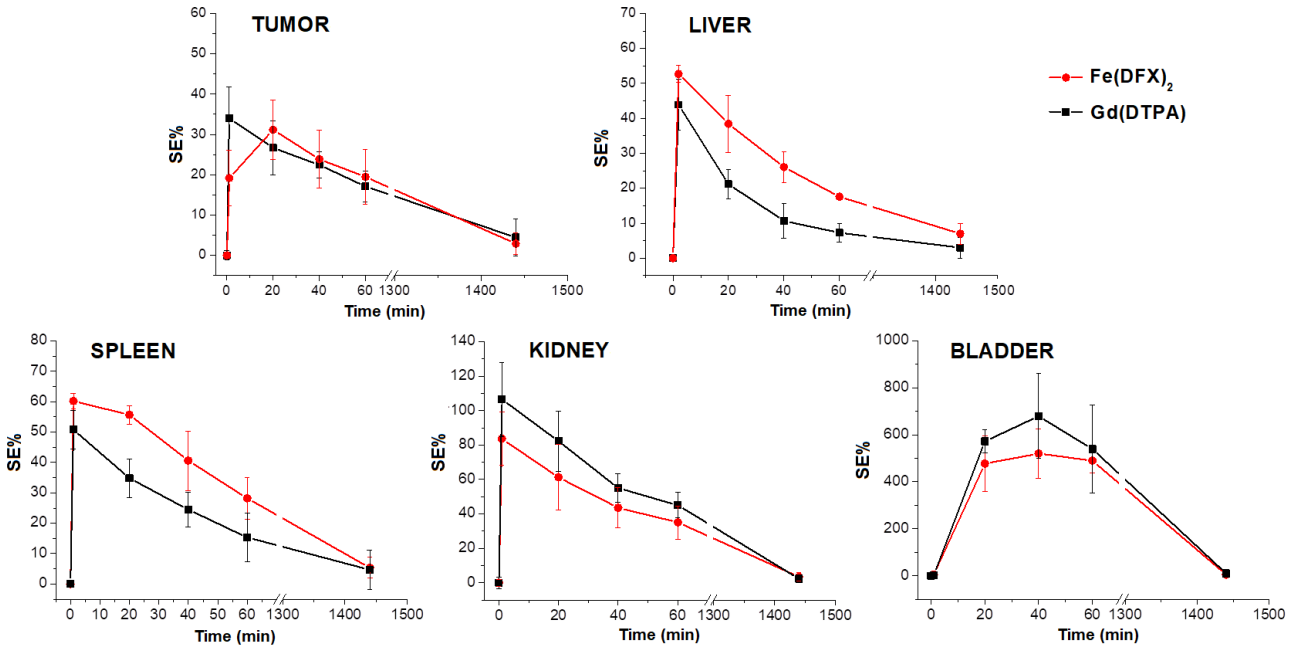

Figure 5.6. Comparison between the changes in signal enhancement (SE%) over time in various body regions after the *in vivo* administration of a dose (0.1 mmol/kg) of $Fe(DFX)_2$ and Gd(DTPA).

5.2.3 Assessment of the elimination of $Fe(DFX)_2$ from blood

The elimination rates of $Fe(DFX)_2$ or Gd(DTPA) from blood of healthy mice, following intravenous administration of 0.1 mmol/kg of the respective contrast agents, were determined by ICP-MS analyses of Fe and Gd levels in blood samples collected at various time points (Figure 5.7).

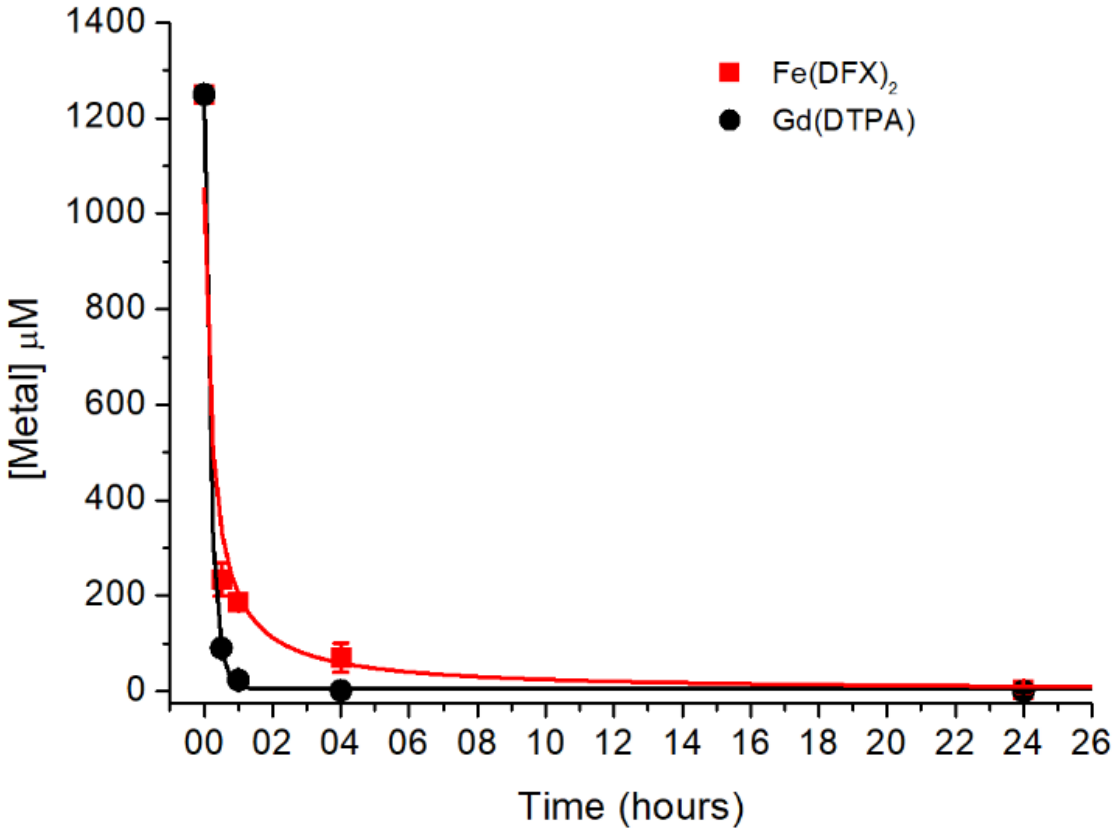

Figure 5.7. Curves representing the decrease of the exogenous Fe and Gd concentrations from the blood of healthy mice upon the intravenous administration of a dose (0.1 mmol/kg) of $Fe(DFX)_2$ or Gd(DTPA), respectively.

The plasma specimens were obtained from blood and mineralized following the procedure described in the Experimental Section. To account for the presence of residual heme iron in the plasma due to slight red blood cell lysis, UV-Vis absorption spectra were acquired at λ = 413 nm (Soret band), and the amount of heme iron was calculated and subtracted from the overall iron amount measured by ICP-MS. The decrease in $Fe(DFX)_2$ concentration in the blood was observed to follow a slower kinetic compared to Gd(DTPA).

At 1 hour after administration, the concentrations of total $Fe(DFX)_2$ and Gd(DTPA) in plasma were 16% and 1.6% of their initial blood metal concentrations, respectively. Similarly, at 2 hours after administration, the concentrations of total $Fe(DFX)_2$ and Gd(DTPA) in plasma decreased to 10% and 0.2% of their initial blood metal concentrations, respectively. These values are consistent with those reported in a pharmacokinetic study conducted on $Fe(DFX)_2$, where 12% of the injected dose was determined to be present in the blood 1 hour after

injection.[104] The slower elimination rate of $Fe(DFX)_2$ can be attributed to its blood-pool characteristics as an albumin-binding agent.

5.3 Discussion

The relaxation enhancement and overall biodistribution/excretion properties shown by $Fe(DFX)_2$ have been demonstrated very promising for the potential application of this complex as an alternative to the currently used GBCAs. Notably, on a 3 T scanner, the observed signal intensity enhancements in tumor regions and other body organs were comparable to those achieved by the clinical Gd(DTPA). The NMRD profiles showed a significant increase in relaxivity in the 1-2 T range of magnetic field strength, suggesting that $Fe(DFX)_2$ may furnish even better performances at the commonly used field strength of 1.5 T in clinical scanners.

One of the primary advantages of $Fe(DFX)_2$ lies in its proven biocompatibility. The DFX ligand is widely used by thalassemic patients to extract accumulated iron ions from their tissues upon blood transfusions necessary for their survival. By acting as a sequestering agent, DFX forms a highly stable complex with the metal ions provided by the iron pool. In the intended use of $Fe(DFX)_2$ as MRI CA, it is synthesized *in vitro* and administered intravenously. While circulating in the body, it behaves as to the complex formed *in vivo* when DFX is used as a sequestering agent, ensuring no metal release or interference with iron or other metal ion homeostasis due to its exceptional stability. It should be noted that the clinical application of DFX as an orally administered iron chelator involves a daily dose of 5 - 40 mg/kg (0.013 - 0.1 mmol/kg) with a maximum plasma concentration (C_{max}) of 0.02 - 0.12 mM.[103] This range of values remains significantly below the maximum concentration achieved by GBCAs immediately after intravenous injection. On the other hand, the prolonged retention of $Fe(DFX)_2$ in the bloodstream, facilitated by its high plasma protein binding, allows for a longer-lasting contrast effect compared to rapidly decreasing plasma concentrations of GBCAs. Therefore, the utilization of $Fe(DFX)_2$ as an MRI contrast agent needs to be adapted to its distinctive properties.

In plasma, three units of $Fe(DFX)_2$ bind to one albumin molecule, specifically to the IB, IIA, and IIIA binding sites on the protein. Competitive assays demonstrated that the decrease in relaxation enhancement, when $Fe(DFX)_2$ is displaced by competing ligands, is site-specific. In each experiment, the observed relaxivity is a combination of the relaxation enhancement contributed by the paramagnetic agent in the two non-involved sites, along with the contribution from the released $Fe(DFX)_2$. Notably, when the complex is displaced from site IB, the resulting R_1 value is the lowest, indicating that this site largely contributes to the overall r_1 of $Fe(DFX)_2$ bound to HSA. This conclusion is further supported by the calculated r_1^b values when $Fe(DFX)_2$ is bound to each of the three binding sites, with the order of bound-relaxivities being IB > IIA > IIIA. This observation can guide the design of site-specific binders to HSA for achieving higher relaxivities.

Furthermore, $Fe(DFX)_2$ exhibits remarkable stability against redox chemistry at the iron center, acting as a weak oxidizing agent (above pH 6, $E_{1/2}$ = -0.58 V): no reduction to $Fe(II)(DFX)_2$ is expected under physiological conditions.[105]

Moreover, its stability reinforces the view that it poses no toxicological concerns. This approach has also been the basis for similar studies proposed by other research groups utilizing highly stable metal complexes, including other sequestering agents such as deferoxamine.[122–124] One of the clear advantages of $Fe(DFX)_2$ is its excellent relaxivity, which is the highest ever reported for a $q = 0$ Fe(III)-complex in serum, at the best of our knowledge. The binding of $Fe(DFX)_2$ to HSA forms a tightly bound 3:1 supramolecular adduct. This binding to albumin appears to induce structural changes in the second coordination sphere proton network. It is likely that the water molecules in the second sphere are hydrogen-bonded to the negatively charged coordinating phenoxide oxygens, and their motion is influenced by the lifetime of these H-bonds. Consequently, the mobility of water molecules trapped in the supramolecular adduct with HSA is significantly reduced compared to those in the free complex.

The reorientational motion of these second sphere water molecules becomes crucial in determining the relaxivity enhancement as the magnetic field strength increases. Exploiting the lengthening of T_{1e} has been a common practice with slowly moving GBCAs that exhibit relaxivity peaks around 1 T. In fact, at this magnetic field, the correlation times for the electronic relaxation of Gd(III) ions approach the molecular reorientational time (for HSA bound complexes, τ_R is in the range of 3-20 ns).[12,125] Recently, a system based on a Fe(III) ion coordinated to three catecholate ligands with a rhodamine moiety on their surface was reported to display relaxometric enhancement properties similar to those observed for $Fe(DFX)_2$ through binding to HSA.[126]

It should be noted that the assignment of the observed relaxation enhancement for $Fe(DFX)_2$ in serum to the closest protons on second sphere water molecules may oversimplify the situation, as other mobile protons on the protein in the vicinity of the interaction site may also contribute. These protons, regardless of their origin, undergo fast exchange with the bulk solvent, as evidenced by the decrease in observed relaxivity with increasing temperature. At 298 K, the relaxivity of the $Fe(DFX)_2$/HSA adduct is 3.8 $mM^{-1}\,s^{-1}$ at 0.47 T, but it increases to 5.7 $mM^{-1}\,s^{-1}$ at 2 T.

Interestingly, it has been reported that the tumor extracellular matrix (ECM) may contain a significant amount of albumin, as this protein serves as the primary energy and nutrition source for tumor growth and has been proposed as a cancer biomarker.[127] This may explain the good signal intensity (SI) and relatively long wash-out observed for $Fe(DFX)_2$ in the tumor region.

Currently, radiologists are actively exploring the use of iron-based MRI contrast agents through off-label applications of ferumoxytol, a drug designed to supply iron to anemia patients. Ferumoxytol consists of ultra-small superparamagnetic iron oxide nanoparticles (USPIONs) whose mediated proton relaxation rate enhancement strongly depends on the compartmentalization of the agent.[128] There is an obvious analogy between the use of ferumoxytol and the proposed $Fe(DFX)_2$ approach, as both aim to exploit systems that are already part of clinical practice. However, the intravascular confinement of ferumoxytol, due to its larger size, makes it a poor replacement for GBCAs, as it may take hours to days for lesion enhancements to occur.

5.4 Conclusion

$Fe(DFX)_2$ demonstrated promising potential as an alternative to currently used GBCAs due to its high biocompatibility, particularly evident by its *in vivo* formation when DFX is employed as an iron-sequestering agent. This study added significant relaxometric and imaging properties of $Fe(DFX)_2$, which are comparable, and at 1.5 T potentially superior, to the clinical GBCAs. Additionally, there is the opportunity to explore the design of other systems based on the coordination cage of DFX, incorporating substituents that could provide enhanced control over the mobility of second-sphere water molecules. This approach may further optimize the field-dependent properties exhibited by $Fe(DFX)_2$, opening up new avenues for development in this area.

5.5 Experimental section

5.5.1 General

Deferasirox was purchased from Advanced Chemblocks Inc. Magnevist (gadopentetate dimeglumine, Gd(DTPA)) was purchased from Bayer S.P.A. All the other chemicals were purchased from Sigma-Aldrich Co. and were used without further purification. pH measurements were made using an AS pH meter equipped with a glass electrode. Chromatographic purification was performed using an AKTA Purifier equipped with a UV-900 system, P-900 pump, frac-920 fraction collector and a Sephadex® G-10 resin column. Mass spectra were recorded on a Waters 3100 Mass Detector (direct infusion with H_2O/CH_3OH 2:1). HPLC analyses were carried out on a HPLC-Waters Alliance Separation Module with a 2998 PDA detector.

5.5.2 Synthesis of iron complexes

5.5.2.3 $[Fe(deferasirox)_2]^{3-}$

75 mg (0.2 mmol, MW = 373.73) of 4-(3,5-bis(2-hydroxyphenyl)-1,2,4-triazol-1-yl)benzoic acid (deferasirox, DFX) were suspended in water (100 mL), basified to pH 9 with a 5 M aqueous solution of *N*-methyl-D-glucamine (meglumine, MGL) and heated at 60 °C under magnetic stirring until complete dissolution. 3.04 mL of a 25 mM aqueous solution of $FeCl_3$ (0.076 mmol) were added dropwise, while maintaining pH 8 with MGL 5 M. The mixture was heated at 60 °C for 1 h under magnetic stirring. The product was purified by chromatography on Sephadex® G-10 resin using water as eluent. The fraction containing the pure product was evaporated and freeze dried. 75 mg of a red solid were obtained.

Anal. Calc.d for $C_{63}H_{77}FeN_9O_{23}\cdot 5H_2O$: C, 51.33; H, 5.95; N, 8.55. Found: C, 51.47; H, 5.72; N, 8.59.

The product was further analyzed by adjusting a method reported in literature[129] on a HPLC-Waters Alliance Separation Module with a 2998 PDA detector and using an Atlantis RP-C18 column. Eluent: 35% buffer (ammonium acetate 50 mM, tetrabutylammonium hydrogen sulfate 10 mM), 45% methanol, 20% acetonitrile. Wavelengths: 225 and 467 and nm.

Retention time: 2.7 min. Mass spectra in direct infusion yielded: $C_{42}H_{27}FeN_6O_8$ ESI-MS (-): *m/z* calcd 798.13 $[M-H]^-$, found 798.34; *m/z* calcd 398.58 $[M-2H]^{2-}$, found 398.76.

5.5.3.4 $[Fe(DTPA)]^{2-}$ and $[Fe(CDTA)]^-$

The meglumine salts of the complexes were prepared following the procedures reported in literature and dissolved in neat water for the ^{17}O-R_2-NMR experiments.[130]

5.5.3 Relaxometric measurements

Observed longitudinal relaxation rates ($R_1^{obs} = 1/T_1^{obs}$) values were determined by inversion recovery at 21.5 MHz and 298 K using a Stelar SpinMaster spectrometer (Stelar s.r.l, Mede (PV), Italy). Temperature was controlled with a Stelar VTC-91 airflow heater and the temperature inside the probe checked with a calibrated RS PRO RS55-11 digital thermometer. Data were acquired using a recovery time ≥ 5 x T_1 and with 2 scans per data point. The absolute error in R_{1obs} measurements was less than 1%.

R_2 values were measured by using the Carr Purcell-Meiboom-Gill (CPMG) sequence on a Bruker WP80 NMR electromagnet (21.5–80 MHz). Data were acquired using echo delay of 8000 ms and with 4 scans per data point.

The iron concentration of the investigated solutions of the $Fe(DFX)_2$ complex was determined by the procedure reported in literature.[131] Briefly, the iron complex containing solutions were mixed in a 1:10 ratio with 69% HNO_3 and heated in sealed vials at 120 °C overnight to yield a solution of Fe^{3+} aqua ion. The R_{1obs} of the solution was measured at 298 K and 21.5 MHz and the concentration determined using the equation: $R_{1obs} = R_{1d} + r_{1p}^{Fe}$ [Fe]. Where R_{1d} is the diamagnetic contribution (0.48 s^{-1}) and r_{1p}^{Fe} is the Fe^{3+} aqua ion relaxivity (18.47 $mM^{-1}s^{-1}$) under the same experimental conditions. The iron concentration of the complexes was confirmed by ICP-MS analysis.

Longitudinal relaxivity (r_1) values reported in Table 5.1 were calculated as slope of the lines correlating observed relaxation rates measured at pH = 7.4, 298 K or 310 K (0.47 T or 1 T) as a function of $Fe(DFX)_2$ concentration.

Stability experiments were performed measuring the R_{1obs} values at 25 °C and 21.5 MHz over several days while the phosphate buffer and human serum solutions of the complex were stored in sealed tubes at 37 °C.

The interaction of the iron complex to human serum albumin (HSA) was studied using the PRE method. Namely, the apparent binding constant (K_a) and the relaxivity of the adduct (r_1^b) were determined by measuring R_1 values of $Fe(DFX)_2$ (0.56 mM) as a function of increasing HSA concentration (0.05-2 mM) in PBS at 298 K, 21.5 MHz, pH 7.4 (Figure 5.3A). On the other hand, the number of binding sites was identified through the relaxometric titration of albumin solutions, at a fixed concentration of 0.6 mM, with increasing $Fe(DFX)_2$ concentrations (0.02-4.5 mM) - Figure 5.3B.

Two sets of competitive experiments were carried out for the identification and characterization of the binding sites on human serum albumin. For the experimental data reported in Figure 5.4A, the R_1 values of solutions containing $Fe(DFX)_2$ (0.6 mM) and HSA (0.2 mM) as function of increasing concentration of the added competitors were measured in

PBS at pH 7.4, 298 K, 21.5 MHz. For the titrations reported in Figure 5.4B, R_1 were measured for solutions of $Fe(DFX)_2$ (0.56 mM) as a function of increasing HSA concentration (0.05-2 mM) in the presence of pairs of competitors in a ratio 1.5 : 1 towards HSA in PBS at pH 7.4, 298 K, 21.5 MHz.

5.5.3.1 NMRD profiles

NMRD profiles were obtained using a Stelar SpinMaster FFC NMR relaxometer from 0.01 to 20 MHz. Additional data in the 20−120 MHz frequency range were obtained with a High Field Relaxometer (Stelar) equipped with the HTS-110 3T Metrology cryogen-free superconducting magnet and a Bruker WP80 NMR electromagnet (21.5–80 MHz), both equipped with a Stelar VTC-91 for temperature control; the temperature inside the probe was checked with a calibrated RS PRO RS55-11 digital thermometer. Aqueous and human serum solutions of the complex were measured at 25 and 37 °C. The NMRD profiles data were fitted using the Solomon-Bloembergen-Morgan and Freed's models modified to take into account contributions from second and outer sphere water molecules.

5.5.3.2 ^{17}O-R_2-NMR measurements

^{17}O-NMR measurements were recorded at 14.1 T on a Bruker Avance 600 spectrometer at variable temperature, with a D_2O capillary for sample locking. Samples contained 1% of $H_2{}^{17}O$ (Cambridge Isotope) and the Fe(III) complexes (20 mM $Fe(DFX)_2$, 20 mM Fe(DTPA) and 4.5 mM Fe(CDTA)). The width at half maximum ($\Delta\omega_{dia}$) of the $H_2{}^{17}O$ signal in pure water was measured over the investigated temperature range and subtracted from the width at half maximum ($\Delta\omega_{Fe}$) of the test solutions containing the Fe-complexes. Then, R_2 was calculated as follows: $R_2=\pi[\Delta\omega_{Fe}-\Delta\omega_{dia}]$. To compare the different profiles, R_2 values were normalized to 20 mM concentration of Fe(III)-complex.

5.5.3.3 Proton relaxation enhancement (PRE) fitting equations

HSA binding parameters were determined using the PRE method, which considers the relaxation enhancement due to the formation of a slowly moving macromolecular adduct, considering the following equilibrium, with the association constant defined as follows:

$Fe(L)_2 + nHSA \leftrightarrow Fe(L)_2\text{-}HSA$

(1)

$$K_a = \frac{[Fe(L)2-HSA]}{[Fe(L)2]\,[nHSA]}$$

(2)

where n is the number of independent binding sites and K_a the apparent binding constant.

Moreover:

$$[Fe(L)_2]_{tot} = [Fe(L)_2]_{free} + [Fe(L)_2\text{-}HSA] \quad (3)$$

and

$$[HSA]_{tot} = [HSA]_{free} + [Fe(L)_2\text{-}HSA] \quad (4)$$

R_{1obs} was defined as follows:

$$R_{1obs} = R_{1p} + R_{1d} = r_1\,[Fe(L)_2] + r_1{}^b\,[Fe(L)_2\text{-}HSA] + R_{1d} \quad (5)$$

Where R_{1p} and R_{1d} are the paramagnetic and diamagnetic contributions to the observed relaxation rates, respectively. And r_1 and r_1^b are the millimolar relaxivities of the iron complex free and bound to HSA, respectively.

The diamagnetic contribution (R_{1d}) was determined as a function of increasing HSA concentration in PBS and included in the fitting function derived from combination of equations 1-5:

$$R_{1obs} = \frac{(K_A[\mathrm{Fe(L)_2}]_{\mathrm{tot}} + nK_A[HSA]_{tot} + 1) - \sqrt{(K_A[\mathrm{Fe(L)_2}]_{\mathrm{tot}} + nK_A[HSA]_{tot} + 1)^2 - 4K_A^2[\mathrm{Fe(L)_2}]_{\mathrm{tot}} n[HSA]_{tot}}}{2K_A}$$

$$\times (r_1^b - r_1 + r_1[\mathrm{Fe(L)_2}]_{\mathrm{tot}}) \times 1000 + (0.25 \times [HSA]_{tot} \times 1000) + 0.359$$

5.5.4 Cell culture and animals

TS/a murine breast cancer cells were derived at the University of Torino from a spontaneous mammary adenocarcinoma which arose in a retired breeder BALB/c female. They were grown in RPMI (Roswell Park Memorial Institute)1064 medium supplemented with 10% heat-inactivated fetal bovine serum (FBS), 2 mM glutamine, 100 U/mL penicillin, and 100 μg/mL streptomycin. Cells were seeded in 75-cm^2 flasks at density of ca. 5 × 10^4 cells/cm^2 in a humidified 5% CO_2 incubator at 37 °C. At confluence, they were detached by adding 1 mL of Trypsin-EDTA solution (0.25% (w/v) Trypsin-0.53 mM EDTA). Cells were negative for mycoplasma as tested by using the MycoAlert™Mycoplasma Detection Kit. Cell media and supplements (RPMI, FBS, glutamine, pen/strep, MycoAlert™ Mycoplasma Detection Kit) were purchased from Lonza Sales AG-EuroClone SpA, Milano (IT). In vivo experiments were carried out by using 10-week-old female Balb/C mice (Charles River Laboratories, Calco, Italy). Mice were kept in standard housing (12 h light/dark cycle) with rodent chow and water available ad libitum. The experiments were performed according to the Amsterdam Protocol on Animal Protection and in conformity with institutional guidelines that are in compliance with national laws (D.L.vo 116/92, D.L.vo 26/2014 and following additions) and international laws and policies (2010/63/EU, EEC Council Directive 86/609, OJL 358, Dec 1987, NIH Guide for the Care and Use of Laboratory Animals, U.S. National Research Council, 1996). This study was carried out in the framework of a protocol approved by the Italian Ministry of Health (authorization number: 808/2017-PR). For tumor-model preparation, mice were anesthetized via an intramuscular injection of tiletamine/zolazepam (Zoletil 100; Virbac, Milan, Italy) 20 mg/kg plus xylazine (Rompun; Bayer, Milan, Italy) 5 mg/kg using a 27-gauge syringe. Ca. 3x10^5 TS/A cells were suspended in 0.1 mL of phosphate buffer solution and subcutaneously injected into each leg of mice (n = 6). Two tumors were implanted into each mouse, to double the number of analyzed tumors. Animals were weekly monitored by calipers for changes in tumor size.

5.5.5 MRI acquisition and data analysis

MR images were acquired 15 days after the tumor inoculation, with tumor volume in a range of 80 - 120 mm^3. For administration of Gd(DTPA) (0.1 mmol/kg) or $Fe(DFX)_2$ (0.1 mmol/kg) an intravenous catheter was inserted in the tail vein of the animal under anaesthesia, before positioning inside the MR scanner. MR images were acquired with a Bruker BioSpec 3 T MRI

GmbH scanner (Bruker Biospin, Ettlingen, Germany) equipped with a 30mm ^{1}H quadrature coil at room temperature (R.T. = 21 °C). T_{1W} images were acquired using a standard multislice multiecho sequence with the following parameters: repetition time (TR) 200 ms; echo time (TE) 11 ms; flip angle = 180°, number of averages = 4, field of view (FOV) 30 mm x 30 mm, slice thickness 1 mm; matrix size 256 x 256. T_{2W} images were acquired using a standard RARE (rapid acquisition with refocused echoes) sequence with the following parameters: TR 3000 ms; TE 12 ms; FOV 30 mm x 30 mm; slice thickness 1 mm, flip angle = 180°, number of averages = 4, RARE factor 32; matrix size 256 x 256. A series of T_1-weighted MSME scans were acquired before and after the intravenous administration of the contrast agents in order to follow the kinetics of bio-distribution.
The T_1 contrast enhancement (SE%) was calculated as follows:

$$SE\% = \frac{\left(\frac{SI(ROI)post}{SI(muscle)post}\right) - \left(\frac{SI(ROI)pre}{SI(muscle)pre}\right)}{\left(\frac{SI(ROI)pre}{SI(muscle)pre}\right)} \times 100$$

where $SI(ROI)post$ and $SI(ROI)pre$ are the signal intensities in the regions of interest (both normalized by dividing for signal intensity in muscle taken as reference) post- and pre-injection of both contrast agents.

5.5.6 Assessment of the elimination of $Fe(DFX)_2$ complex from blood

The kinetics of $Fe(DFX)_2$ and Gd(DTPA) removal from the blood were assessed by ICP-MS quantification of the Gd and Fe content in the plasma. For this purpose, after the intravenous injection of one dose (0.1 mmol/kg) of $Fe(DFX)_2$ or Gd(DTPA) to healthy mice (n = 3 for each time point), blood was collected from mice tail veins at variable time points (t = 30 min, 1 h, 4 h, 24 h). Blood was centrifuged for 7 min at 2300 rpm, R.T., to separate and collect the plasma fraction. An aliquot of plasma was used for measurement of Gd or overall (heme and not-heme) Fe by inductively coupled plasma mass spectrometry (ICP-MS). Another part was used for quantification of heme iron by UV-Vis spectroscopy through the measure of the absorbance at λ = 413 nm (Soret Band) by using a 6715 UV-Vis Spectrophotometer Jenway (Bibby Scientific Limited, Beacon Road, Stone, Staffordshire, ST15 OSA, UK). The heme iron concentration was calculated based on a previously obtained calibration curve in which the absorbance at λ = 413 nm was plotted against the iron concentration measured by ICP-MS in plasma samples collected from mice which were never received $Fe(DFX)_2$ (Figure 5.8).

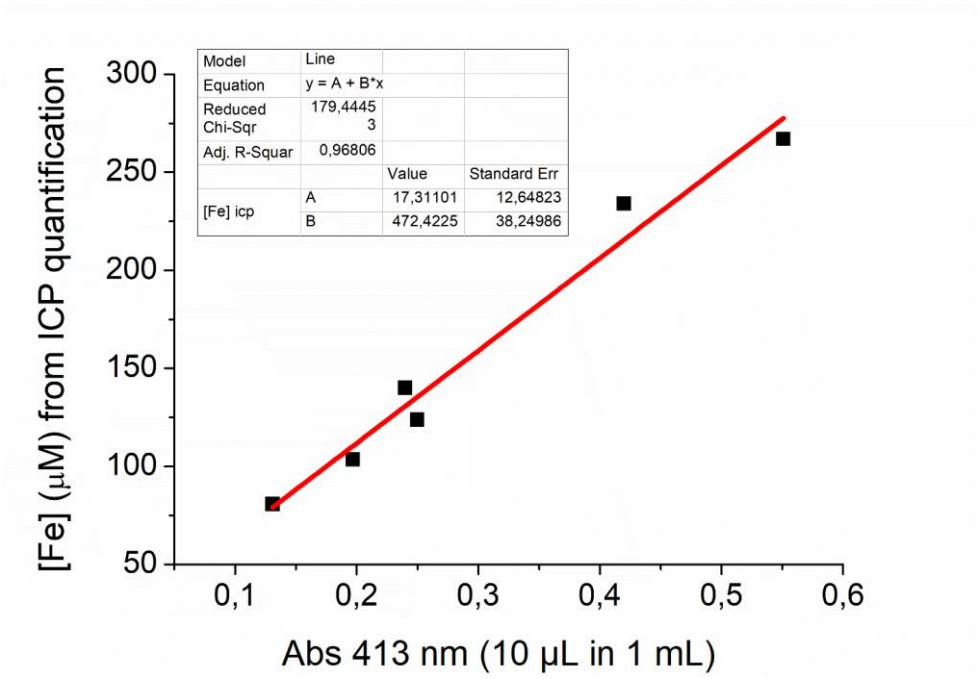

Figure 5.8. Linear correlation between the absorbance measured at 413 nm and the residual heme-iron content in plasma samples of mice which never received $Fe(DFX)_2$.

Before ICP-MS analysis, plasma samples were digested with concentrated HNO_3 (70%) under microwave heating (Milestone MicroSYNTH Microwave lab-station, Milestone Inc., Bergamo, Italy). After the digestion, 2 mL of ultrapure water were added to each sample. The specimens were then subjected to ICP-MS analysis (Element-2; Thermo-Finnigan, Rodano (MI), Italy) to measure the concentration of Fe and Gd with respect to standard curves. The total iron content was subtracted by the Heme iron to assess the effective plasma concentration of iron derived from $Fe(DFX)_2$ complex.

Chapter 6

Preliminary studies on the Fe(III) complexes of two deferasirox-β-cyclodextrin hybrids as potential MRI T_1 contrast agents

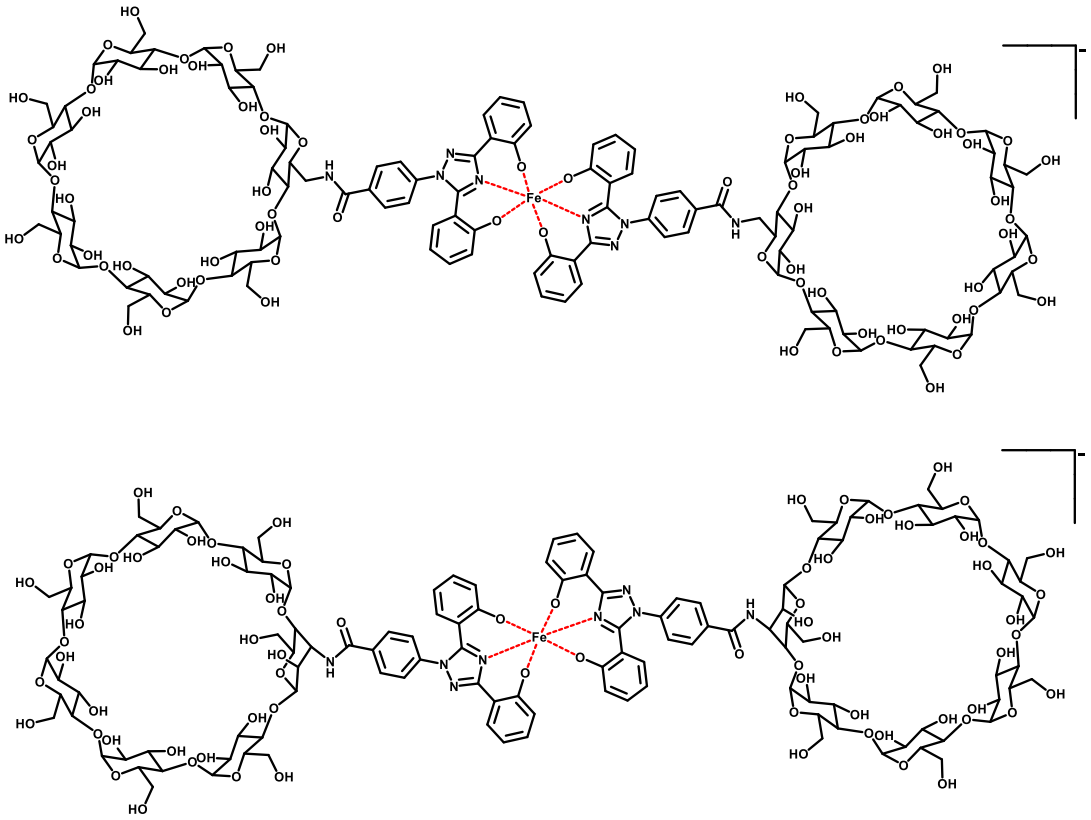

6.1 Introduction

In the fifth chapter of this thesis, the Fe(III) complex with two units of deferasirox (DFX), an iron sequestering agent commonly used in thalassemic patients, was shown to display a MRI contrast comparable to that of the commercial Gd-DTPA agent.[132] As a continuation of the work, it was deemed of interest to functionalize the compound in order to improve the most important characteristics of the metal complex as potential MRI CA, such as relaxivity, solubility and biocompatibility. Indeed, the carboxylate group of DFX does not participate in the chelation of the metal center and thus guarantees an excellent site for functionalization.

In 2019, Gascon and coworkers conjugated DFX via an amide coupling reaction, to both 3^A-amino-3^A-deoxy-2^A(S),3^A(S)-β-cyclodextrin (3a) and 6^A-amino-6^A-deoxy-β-cyclodextrin (6a) and demonstrated a significant improvement of the biological properties of this iron chelating drug accompanied by a cytotoxicity decrease.[133]

Cyclodextrins (CyDs) are cyclic oligosaccharides made up of α-(1,4) linked glucopyranose subunits, forming a cage-like supramolecular structure (see Figure 6.1).

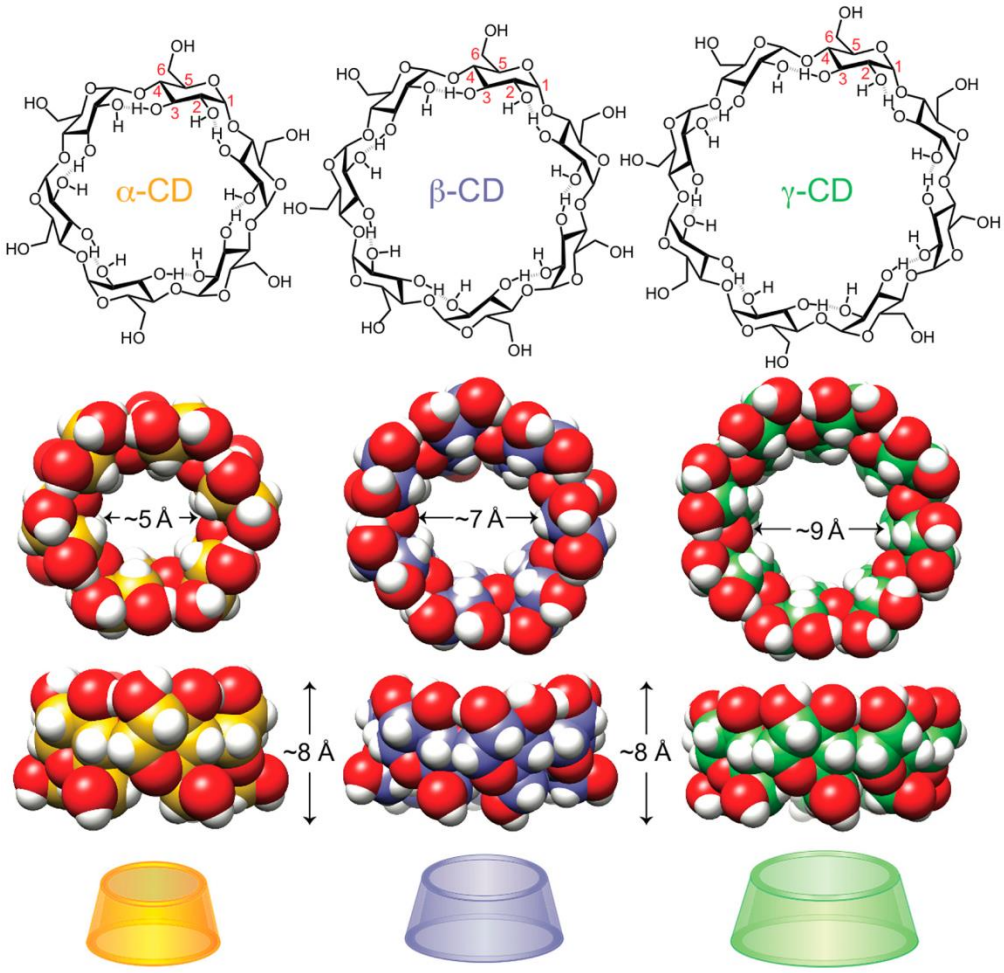

Figure 6.1. Structural, space-filling, and graphical representations of the three main cyclodextrin (CD) molecules: α-CD (yellow), β-CD (blue), and γ-CD (green). Reprinted from [134].

Based on the number of subunits, they can be divided into α-cyclodextrins (6 subunits), β-cyclodextrins (7 subunits) or γ-cyclodextrins (8 subunits). These compounds are capable of forming inclusion complexes with several molecules, often significantly modifying the properties of the materials they interact with.[134]

CyDs find extensive use in various technologies, analytical methods and industrial products, and show negligible cytotoxicity in applications such as drug delivery, cosmetics, textiles, and more.[135] They offer a broad spectrum of interactions with biomolecules, and can also be functionalized for specific interactions with chosen bimolecular targets. This versatility holds significant promise in the field of medicine, and numerous applications are anticipated to emerge in the coming years.[136]

In this chapter, the synthesis and the relaxometric characterization of the iron(III) complexes of the two deferasirox-β-cyclodextrin hybrids (3a-DFX) and (6a-DFX) are described. The chemical structures of the two ligands are shown in Chart 6.1.

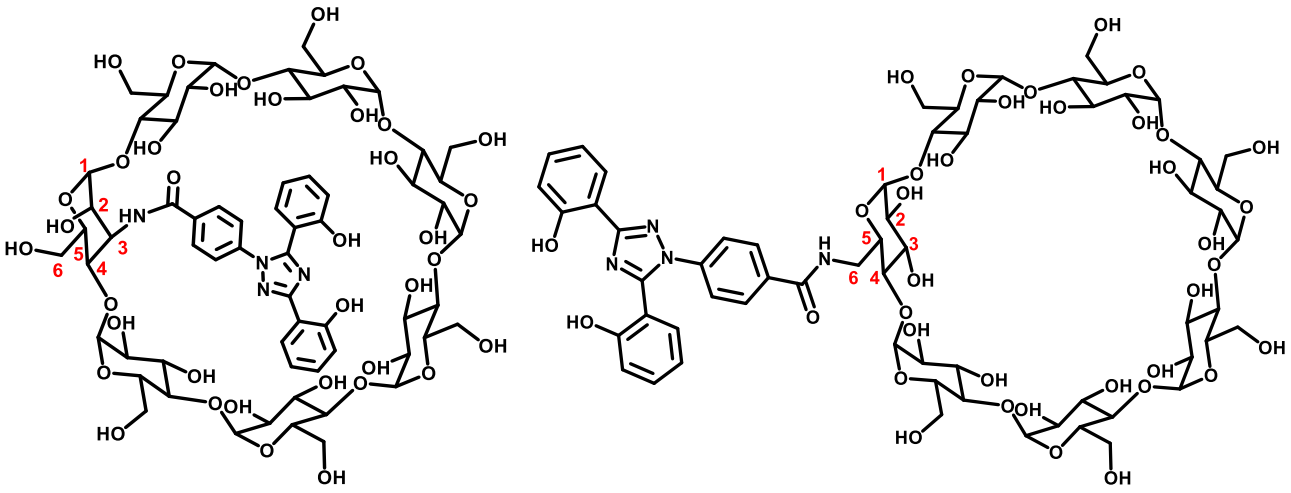

Chart 6.1. Chemical structure of the ligands 3a-DFX (left) and 6a-DFX (right).

Although no examples reporting the isolated Fe(III) complexes of these hybrids are present in literature, their thermodynamic stability is known to be very high: log β = 36.0 for Fe(3a-DFX)$_2$, and log β = 35.3 for Fe(6a-DFX)$_2$).[133] These values are only slightly lower than the one reported for the precursor Fe(DFX)$_2$ (log β = 38.6).[102]

6.2 Results and discussion

6.2.1 Synthesis

The syntheses of the complexes [Fe(3a-DFX)$_2$]$^-$ (Scheme 6.1) and [Fe(6a-DFX)$_2$]$^-$ (Scheme 6.2) were achieved by an amide coupling reaction of deferasirox (4-[(3,5-bis-(2-idroxyphenyl)-1,2,4)triazol-1-yl]-benzoic acid, DFX) with 3^A-amino-3^A-deoxy-2^A(S),3^A(S)-β-cyclodextrin (3a) or 6^A-amino-6^A-deoxy-β-cyclodextrin (6a), followed by complexation with Fe(III). In the following sections, the two Fe(III) complexes are simply reported as Fe(3a-DFX)$_2$ and Fe(6a-DFX)$_2$.

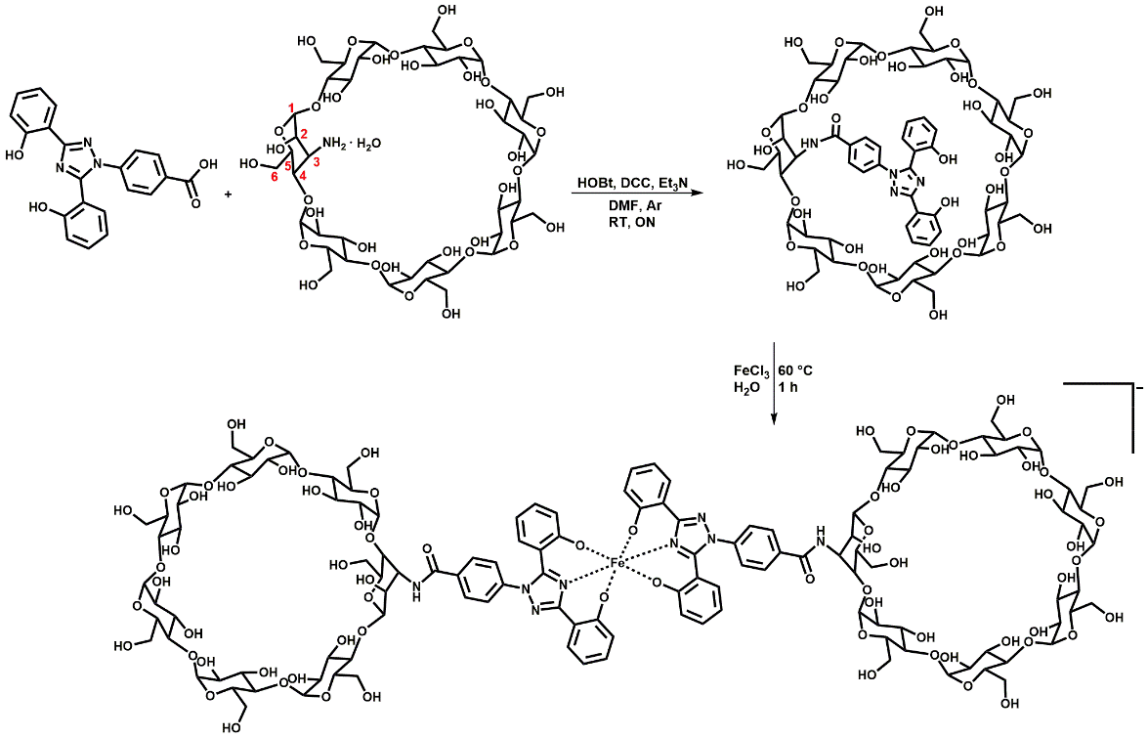

Scheme 6.1. Synthesis of $[Fe(3a\text{-}DFX)_2]^-$.

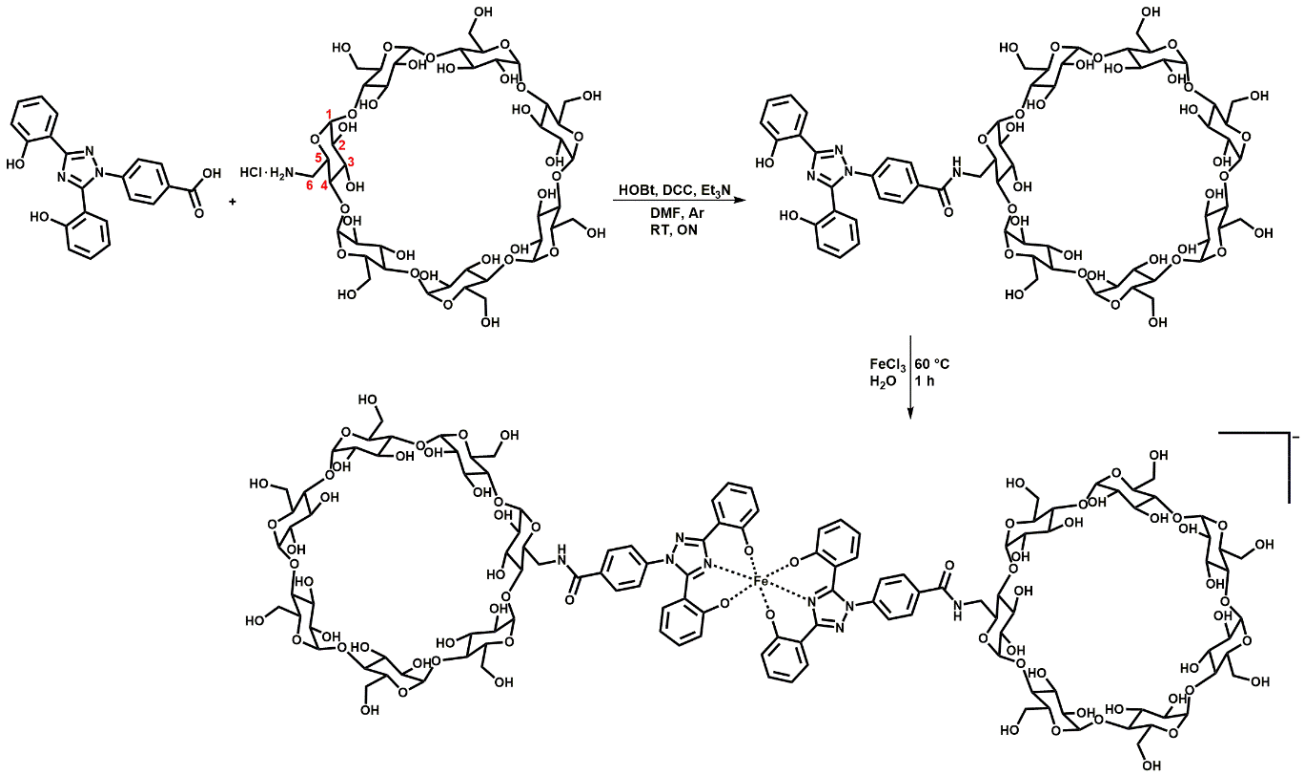

Scheme 6.2. Synthesis of $[Fe(6a\text{-}DFX)_2]^-$.

6.2.2 Relaxometric measurements

The r_1 relaxivity values for Fe(3a-DFX)$_2$ and Fe(6a-DFX)$_2$ were obtained by measuring the relaxation rate of the iron complexes at different concentrations in water and in human serum (Figure 6.2), at 298 K, 0.47 and pH 7.4.

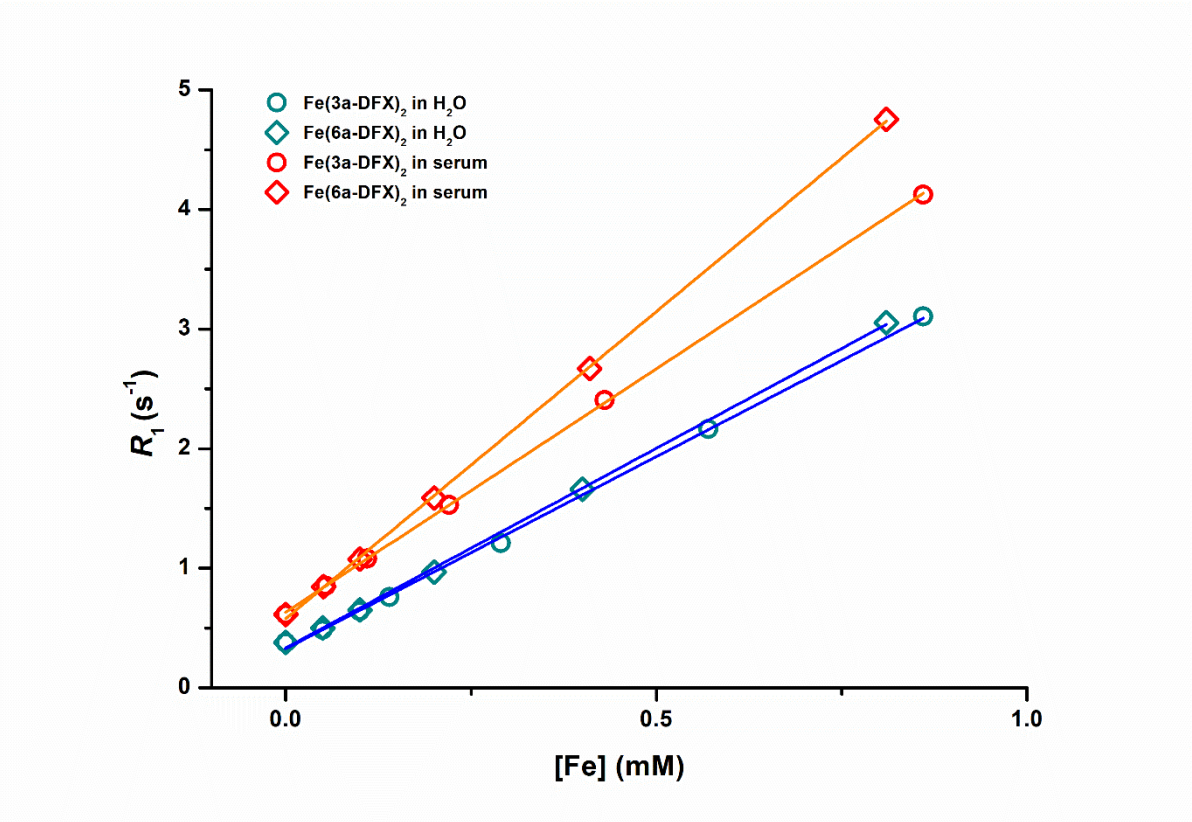

Figure 6.2. Longitudinal relaxation rate as a function of the contrast agents concentration in water (blue) and human serum (red) measured for Fe(3a-DFX)$_2$ (circles) and Fe(6a-DFX)$_2$ (diamonds). 0.47 T, 298 K, pH 7.4.

The r_1 values obtained by the experimental data in Figure 6.2 are shown in Table 6.1 and compared with the ones of parent compound Fe(DFX)2.

Table 6.1. Relaxivity values at 0.47 T, 298 K, pH 7.4.

	r_1 in H_2O	r_1 in human serum
Fe(3a-DFX)$_2$	3.2 ± 0.04	4.1 ± 0.02
Fe(6a-DFX)$_2$	3.3 ± 0.05	5.1 ± 0.03
Fe(DFX)$_2$	2.5 ± 0.31	3.4 ± 0.32

Relaxivity values of Fe(3a-DFX)$_2$ and Fe(6a-DFX)$_2$ calculated from the experimental data in Figure 6.2 and compared with the ones of the parent compound Fe(DFX)$_2$.

Both for Fe(3a-DFX)$_2$ and Fe(6a-DFX)$_2$ the r_1 values, either in pure water and in human serum, were higher than that of the parent compound. Such increase is likely ascribable to the increased molecular weight of the two isomers, as well as to a larger contribution arising from second sphere water molecules interacting with the hydrophilic cyclodextrin moieties.

The observed relaxivities remained constant over several days when the solutions of both complexes were maintained at 310 K.

As in the case of the parent compound, the verification of the absence of any contribution to the observed relaxivity arising from inner sphere water molecules directly coordinated to the metal center was assessed by carrying out the variable-temperature ^{17}O-R_2-NMR experiments. [36] The ^{17}O-transverse relaxation rate of aqueous solutions of both Fe(3a-DFX)$_2$ and Fe(6a-DFX)$_2$ were measured at different temperatures. In Figure 6.3 the profiles of the new iron complexes are compared with the one of the parent compound and the ones of two well-known complexes with q = 1 (Fe(CDTA)) and q = 0 (Fe(DTPA)). As for Fe(DFX)$_2$, it is evident that Fe(3a-DFX)$_2$ and Fe(6a-DFX)$_2$ behave as a system with no water molecules coordinated to the Fe(III) ion.

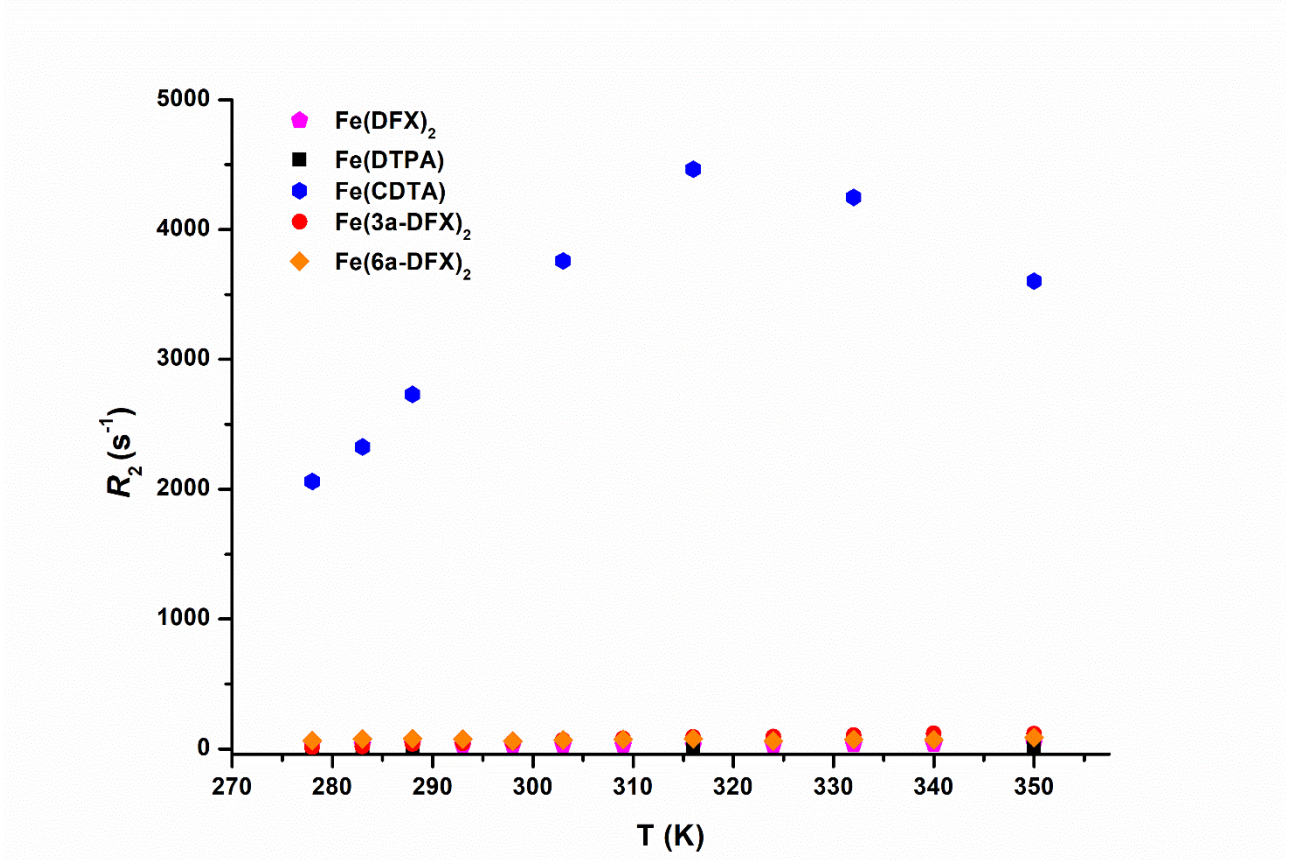

Figure 6.3. Comparison between ^{17}O-transverse relaxation rate measured as a function of temperature obtained for Fe(3a-DFX)$_2$, Fe(6a-DFX)$_2$, Fe(DFX)$_2$, Fe(DTPA) and Fe(CDTA). Data are normalized to 20 mM iron concentration. 14.1 T, pH 7.4.

Further information regarding the determinants of the observed relaxivity was obtained recording the $1/T_1$ ^{1}H-NMRD profiles over an extended range of magnetic field strengths (0.01 - 80 MHz as proton Larmor Frequency). The NMRD profiles, measured in water at neutral pH and 298 K, for Fe(3a-DFX)$_2$ and Fe(6a-DFX)$_2$ are shown in Figure 6.4, compared with the parent Fe(DFX)$_2$.

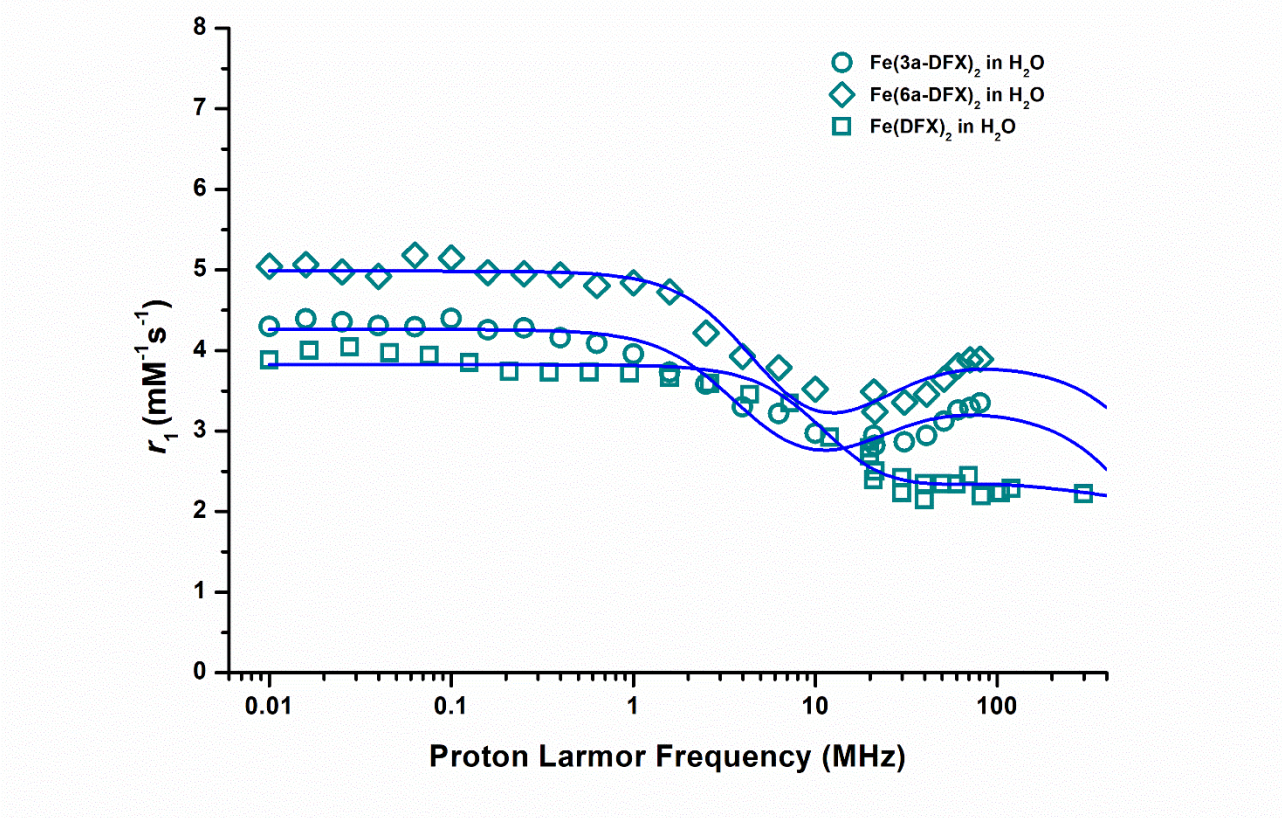

Figure 6.4. NMRD profiles of Fe(3a-DFX)$_2$, Fe(6a-DFX)$_2$ and Fe(DFX)$_2$ measured in H_2O at 298 K, pH 7.4.

The relaxivity values measured for Fe(6a-DFX)$_2$ resulted higher than the isomer Fe(3a-DFX)$_2$ in the whole range of magnetic field strengths recorded. For both compounds, the shape of the NMRD profile, with a broad hump in the high field region 0.5 – 2 T, is typical of the Fe(III) complexes with relatively high MW, showing an elongated reorientational time.

The experimental relaxivity data were fitted by using Solomon-Bloembergen-Morgan (SBM) theory of paramagnetic relaxation.[108–110]. The relevant relaxometric parameters obtained by the fitting are shown in Table 6.2.

Table 6.2. Relaxometric parameters obtained by the fitting of the experimental data in Figure 6.4 using a Solomon-Bloembergen-Morgan model.

H_2O	Δ^2 (10^{20} s^{-2})	τ_V (ps)	n^{SS}	r^{SS} (Å)	τ_C^{SS} (ps)
Fe(3a-DFX)$_2$	1.02 ± 0.21	15.7 ± 2.0	2	3.48	242 ± 35
Fe(6a-DFX)$_2$	1.30 ± 0.27	14.9 ± 1.8	4	3.48	164 ± 18
Fe(DFX)$_2$	1.01 ± 0.17	24.7 ± 2.1	4	3.48	74 ± 0.49

Δ^2: Squared mean transient zero-field splitting (ZFS) energy; τ_V: correlation time for the collision-related modulation of the ZFS Hamiltonian; n^{SS}: number of second sphere water protons; r^{SS}: distance between Fe and protons of second sphere water molecules; τ_C^{SS}: correlation time for the modulation of the dipolar interaction of the second coordination sphere water molecules (exchange and/or rotation).

The following parameters were fixed during the fitting procedure: q^{is} (number of inner sphere water molecules) = 0; D (solute-solvent diffusion coefficient) = 2.24 10^{-5} cm^2 s^{-1}; r_{FeH}^{ss} (distance between Fe^{3+} ion and protons of the second sphere water molecules) = 3.48 Å (calculated as follows: Fe-O average bond length from crystal structure = 1.98 Å[105] + O-H strong hydrogen bond = 1.5 Å[115]).

The second sphere molecular correlation time τ_c^{SS} reflects the molecular reorientational time of the complex, and the contribution of H-bonded water molecules or paramagnetically relaxed mobile protons on the complex surface. An elongation of τ_c^{SS} commonly yields an increase in relaxivity. With respect to $Fe(DFX)_2$, $Fe(3a\text{-}DFX)_2$ showed a large increase in τ_c^{SS}, with a value more than threefold than the parent compound (242 ps vs. 74 ps). In the case of $Fe(6a\text{-}DFX)_2$ the obtained value is relatively lower (164 ps), but still more than twofold than $Fe(DFX)_2$. The number of second sphere water protons n^{SS} obtained from the best fit for $Fe(3a\text{-}DFX)_2$ and $Fe(6a\text{-}DFX)_2$ was 2 and 4, respectively. Although the τ_c^{SS} and n^{SS} values obtained for the two complexes are significantly different, the observed relaxivities in water are similar, indicating that the contributions of these two parameters compete to the overall r_1 relaxivity. It is likely that in $Fe(3a\text{-}DFX)_2$, 2 protons from 2 water molecules are hydrogen bonded to the coordinating negatively charged oxygens, while in the case of $Fe(6a\text{-}DFX)_2$ 2 more protons are present in the second coordination sphere, possibly due to the more accessible paramagnetic center of this complex. In fact, although the two compounds are isomers, in $Fe(3a\text{-}DFX)_2$ the cyclodextrin moiety is closer to the core of the system. However, it cannot be ruled out that, with the more flexible structure of $Fe(6a\text{-}DFX)_2$, exchanging protons of the cyclodextrin moieties can take part in the relaxation mechanism too.

In Figure 6.5 the NMRD profiles of $Fe(3a\text{-}DFX)_2$ and $Fe(6a\text{-}DFX)_2$, measured in human serum at 298 K, are shown and compared with the parent $Fe(DFX)_2$.

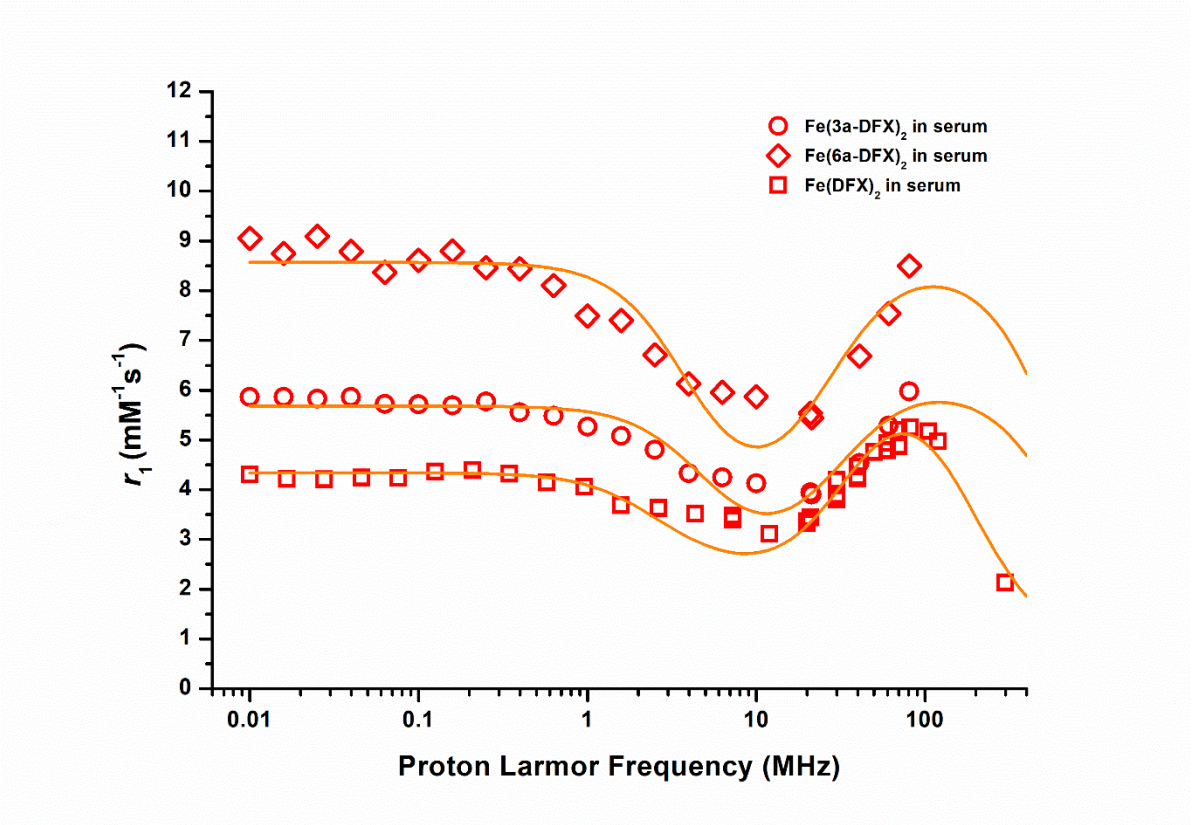

Figure 6.5 NMRD profiles of Fe(3a-DFX)$_2$, Fe(6a-DFX)$_2$ and Fe(DFX)$_2$ measured in human serum at 298 K, pH 7.4.

In human serum, the difference between the r_1 values of the two compounds appears more marked than in water, with Fe(6a-DFX)$_2$ endowed with higher relaxivity in the whole investigated range. Differently than the parent compound, both the novel complexes display high r_1 values already in the low range of magnetic field strength, indicating a strong increase of the contribution from the second coordination sphere.[12,30,32]

In Table 6.3 the relevant relaxometric parameters obtained by the fitting of the experimental data with the SBM theory are shown.

Table 6.3. Relaxometric parameters obtained by the fitting of the experimental data in Figure 6.5 using a Solomon-Bloembergen-Morgan model.

Human serum	Δ^2 (10^{20} s^{-2})	τ_V (ps)	n^{SS}	r^{SS} (Å)	τ_C^{SS} (ps)
Fe(3a-DFX)$_2$	2.07 ± 0.20	11.2 ± 1.1	5	3.48	232 ± 14
Fe(6a-DFX)$_2$	1.50 ± 0.23	11.6 ± 1.6	7	3.48	245 ± 17
Fe(DFX)$_2$	1.10 ± 0.10	13.3 ± 0.9	2	3.48	850 ± 53

Δ^2: Squared mean transient zero-field splitting (ZFS) energy; τ_v: correlation time for the collision-related modulation of the ZFS Hamiltonian; n^{SS}: number of second sphere water protons; r^{SS}: distance between Fe and protons of second sphere water molecules; τ_c^{SS}: correlation time for the modulation of the dipolar interaction of the second coordination sphere water molecules (exchange and/or rotation).

As in the case of the fitting of the NMRD profile in water, in serum the parameters q^{is}, D and r_{FeH}^{ss} were kept fixed at the same values.

It can be noted that the τ_c^{SS} value obtained for the two complexes was similar (232 ps for Fe(3a-DFX)$_2$ and 245 for Fe(6a-DFX)$_2$) and significantly lower than the one obtained for the parent compound (850 ps), likely due to a lower interaction with HSA. The number of second sphere water protons n^{SS} found with the best fitting was 5 for Fe(3a-DFX)$_2$ and 7 for Fe(6a-DFX)$_2$, indicating an increased pool of second sphere water molecules compared to Fe(DFX)$_2$ (n^{SS} = 2). It is likely that some component present in the human serum is responsible for non-covalent interactions with the paramagnetic complexes, leading to a strong relaxivity enhancement, more pronounced in the case of Fe(6a-DFX)$_2$ reaching the r_1 impressive value of 8 mM^{-1} s^{-1} at the clinical field of 2 T.

To investigate a possible interaction with albumin, the most abundant protein in human plasma, the PRE titrations with increasing amounts of HSA were carried out for of Fe(3a-DFX)$_2$ (Figure 6.6) and Fe(6a-DFX)$_2$ (Figure 6.7).

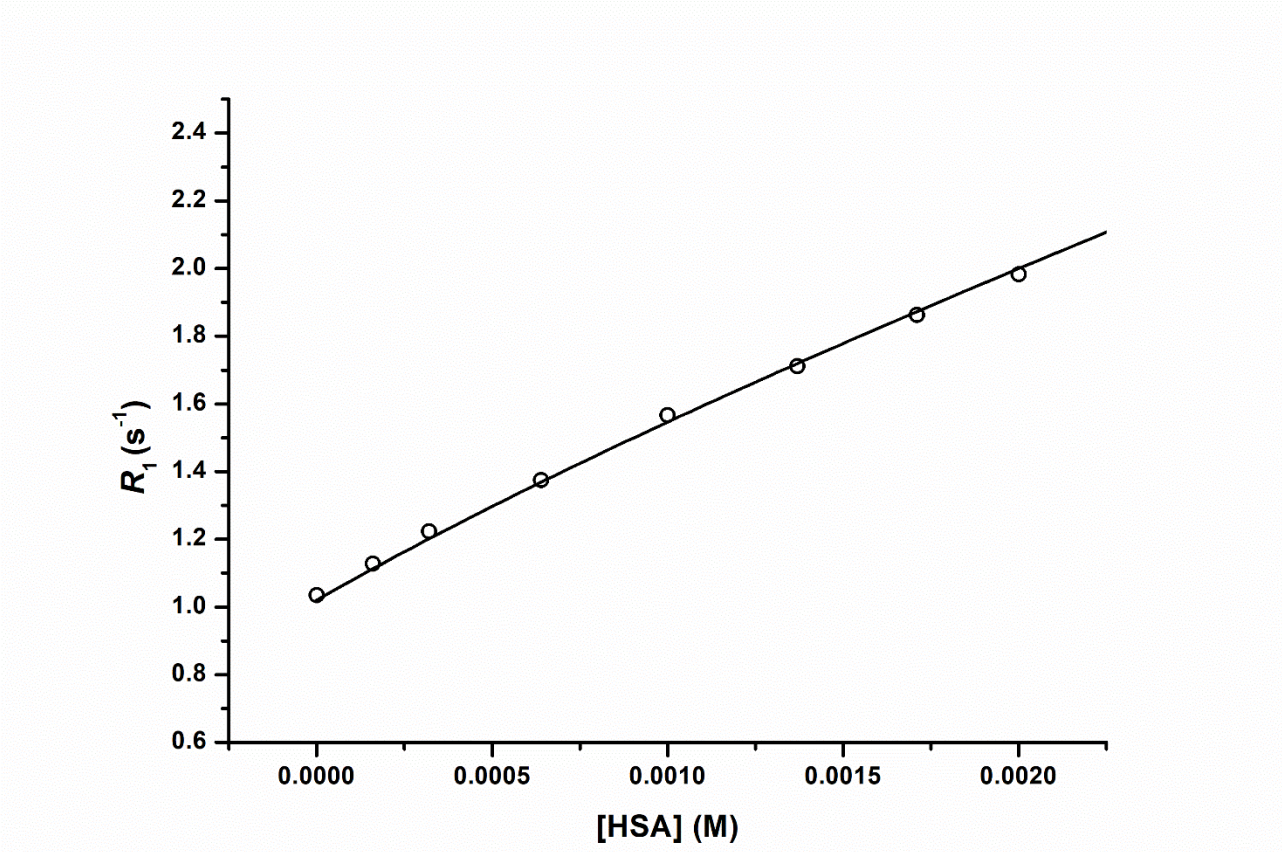

Figure 6.6. Proton relaxation enhancement (PRE) titration of Fe(3a-DFX)$_2$ (0.2 mM) with increasing concentration of human serum albumin (HSA), in phosphate buffer, 298 K, 0.47 T.

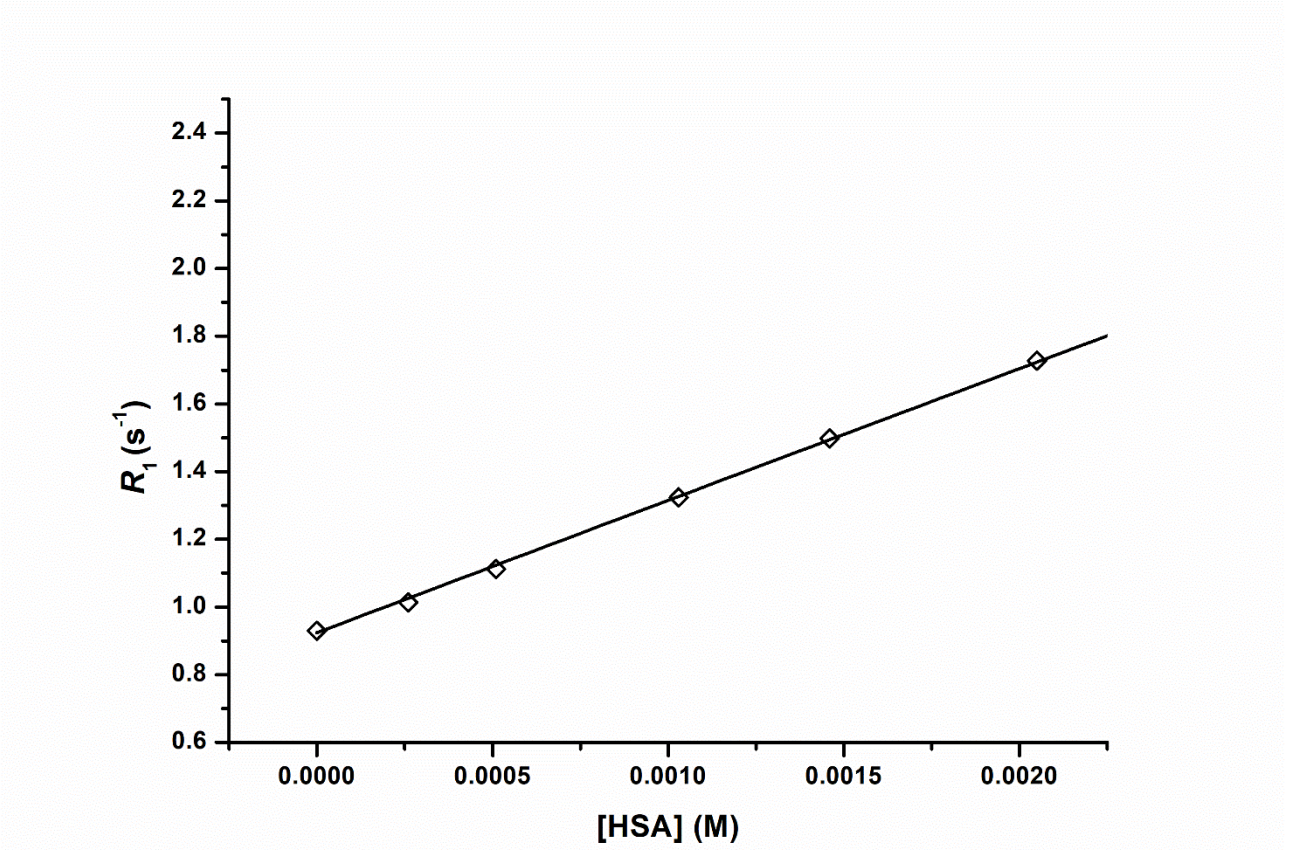

Figure 6.7. Proton relaxation enhancement (PRE) titration of Fe(6a-DFX)$_2$ (0.16 mM) with increasing concentration of human serum albumin (HSA), in phosphate buffer, 298 K, 0.47 T.

Table5. Parameters derived by the fitting of PRE titrations in Figure 6.6, Figure 6.7 and Figure 5.3A.

HSA-binding	K_a (M^{-1})	r_1^b ($mM^{-1}\ s^{-1}$)
Fe(3a-DFX)$_2$	525 ± 36	5.5 ± 0.2
Fe(6a-DFX)$_2$	68 ± 15	5.0 ± 0.1
Fe(DFX)$_2$	(2.8 ± 0.3) · 10^5	3.8 ± 0.1

Although a broad hump in relaxivity is noticeable in the high field range of both NMRD profiles, no evidence of strong albumin binding was observed from the fitting of the PRE titrations. Such behavior can be explained by the presence of the cyclodextrin moieties in the two derivatives. Indeed, the presence of two hydrophilic and sterically encumbering groups makes unlikely the possibility of a binding interaction to the hydrophobic Sudlow sites of HSA as in the case of the parent compound Fe(DFX)$_2$. However, the occurrence of weak and unspecific interactions between the iron complexes and albumin cannot be excluded.

Ghosh et al. reported evidence of α- β and γ-cyclodextrins binding to human and bovine serum albumin (BSA) at different positions, leading to a polarity change in the micro-environment of

the sites of interest.[137] Through experimental studies and docking simulations they showed that the binding site in albumin depends on the cavity size of the cyclodextrin: in the case of β-cyclodextrin the preferred site is the subdomain IIB, with an affinity constant K_a of 185 M^{-1} for HSA and 198 M^{-1} for BSA. Gao et al. studied the binding interaction between different modified mono- and bis-β-cyclodextrin and BSA via fluorescence spectroscopy and other techniques.[138] Interestingly, they found a stronger interaction for the bridged bis-β-cyclodextrin derivatives, with a structure and size similar to $Fe(3a\text{-}DFX)_2$ and $Fe(6a\text{-}DFX)_2$. The strong binding stability of bis-cyclodextrins is attributed to the cooperative effect of two adjacent cyclodextrin moieties. In another study about the conformational stability of selected proteins upon the addiction of cyclodextrin derivatives, only small effects were observed in the case of BSA.[139]

To investigate if any other component of the serum is responsible for the observed relaxivity enhancement in serum, the PRE titrations of the two compounds with increasing amounts of γ-globulins and cholesterol were carried out. No increase in relaxivity was found and the experiments are not reported.

6.3 Conclusion

The iron(III) complexes of two deferasirox-β-cyclodextrin hybrids (3a-DFX) and (6a-DFX) were synthesized and tested for their potential application in MRI as paramagnetic contrast agents.

In summary, the preliminary studies reported here showed that both $Fe(3a\text{-}DFX)_2$ and $Fe(6a\text{-}DFX)_2$ are interesting compounds for this purpose. Iron-based MRI CAs are considered very appealing, as they offer an alternative to the routinely used GBCAs without the use of any exogenous metal. The functionalization of the structure $Fe(DFX)_2$ with β-cyclodextrin moieties endows the herein novel compounds with high biocompatibility, since these cyclic sugars are highly water-soluble and nontoxic. A further advantage given by the use of cyclodextrins is the low cost for their production.

With respect to the parent compound $Fe(DFX)_2$, a strong increase in relaxivity, accompanied by an excellent improvement in solubility, were observed for both $Fe(3a\text{-}DFX)_2$ and $Fe(6a\text{-}DFX)_2$, either in pure water and in human serum.

In water, the fitting of the NMRD profiles showed that the observed relaxivity upgrade is ascribable to the increased molecular weight, leading to a slowing-down of the molecular tumbling, as well as to the presence of second sphere water molecules close to the paramagnetic center. For both complexes, no inner sphere water molecules were found, in analogy to the precursor $Fe(DFX)_2$ with $q = 0$.

In human serum, the relaxivity increase was even greater, with the highest values obtained for $Fe(6\text{-}DFX)_2$, with r_1 values even higher than the clinically used GBCAs (at 2 T, $r_1 = 8$ mM^{-1} s^{-1}). The fitting of the NMRD profiles showed a further increase in second sphere water molecules for both compounds and only a slight slowing-down of the molecular tumbling. Relaxometric PRE titrations showed no evidence of significant binding interaction with HSA for any of the two complexes.

Further relaxometric and structural investigation is still needed to elucidate the dynamics of these novel compounds in human serum. Studies on murine models to validate the effectiveness of these new Fe(III)-complexes as potential MRI CAs *in vivo* are also planned. Nevertheless, $Fe(3a\text{-}DFX)_2$ and $Fe(6a\text{-}DFX)_2$ showed to be excellent candidates as iron(III)-based MRI CAs, with a strong improvement in relation to the parent $Fe(DFX)_2$.

6.4 Experimental section

6.4.1 General

Deferasirox was purchased from Advanced Chemblocks Inc. 6^A-amino-6^A-deoxy-β-cyclodextrin hydrochloride was purchased from Cyclolab Ltd. 3^A-amino-3^A-deoxy-2^A(S),3^A(S)-β-cyclodextrin hydrate was purchased from TCI Europe N.V. All the other chemicals were purchased from Sigma-Aldrich Co. pH measurements were made using an AS pH meter equipped with a glass electrode. Chromatographic purification was performed using an AKTA Purifier equipped with a UV-900 system, P-900 pump, frac-920 fraction collector.

6.4.2 Synthesis

6.4.2.1 Synthesis of 4-[3,5-bis(2-hydroxyphenyl)-1H-1,2,4-triazol-1-yl]-*N*-[3A-deoxy-3A-amino-β-cyclodextrin]benzamide (3a-DFX)

The synthesis was made following, and slightly modifying, the procedure previously reported in literature.

37.3 mg (0.1 mmol) of deferasirox were dissolved in 2 mL of dry DMF under Ar flux. 13.5 mg (0.1 mmol) of HOBt and 20.6 mg (0.1 mmol) of DCC were added to the solution. After 30 min stirring at RT, 113.4 mg (0.1 mmol) of 3^A-amino-3^A-deoxy-2^A(S),3^A(S)-β-cyclodextrin hydrate were added, washing the flask with 1 more mL of dry DMF. The reaction mixture was kept stirring at RT under Ar for 48 h. The solvent was removed under reduced pressure. The crude product was triturated with diethyl ether and with cold acetone and the solid was purified by reversed-phase chromatography using an AKTA Purifier with a Waters C-18 column and H_2O/CH_3OH as eluents. A white solid was obtained. Yield 59 %.

Retention time: 10.12 min. Mass spectrum: ESI-MS (+): *m/z* calcd 1489.49 $[M+H]^+$, found 1489.66; *m/z* calcd 745.01 $[M+2H]^{2+}$, found 745.19.

^{1}H NMR (600 MHz, D_2O): δ = 8.04–7.72 (m, 3 H), 7.68–7.22 (m, 5 H), 7.18–6.93 (m, 3 H), 6.73 (s, 1 H), 5.16–4.96 (m, 5 H), 4.73–4.66 (m, 2 H), 4.48–2.72 (m, 42 H).

6.4.2.2 Synthesis of 4-[3,5-bis(2-hydroxyphenyl)-1H-1,2,4-triazol-1-yl]-*N*-[6A-amino-6A-deoxy-β-cyclodextrin]benzamide (6a-DFX)

The synthesis was made following, and slightly modifying, the procedure previously reported in literature.

37.3 mg (0.1 mmol) of deferasirox were dissolved in 2 mL of dry DMF under Ar flux. 13.5 mg (0.1 mmol) of HOBt, 20.6 mg (0.1 mmol) of DCC and 28 μL (0.3 mmol) of Et_3N were added to the solution. After 30 min stirring at RT, 117 mg (0.1 mmol) of 6^A-amino-6^A-deoxy-

β-cyclodextrin hydrochloride were also added, washing the flask with 1 more mL of dry DMF. The reaction mixture was kept stirring at RT under Ar for 48 h. The solvent was removed under reduced pressure. The crude product was triturated with diethyl ether and with cold acetone and the solid was purified by reversed-phase chromatography using an AKTA Purifier with a Waters C-18 column and H_2O/CH_3OH as eluents. A white solid was obtained. Yield 43%.

Retention time: 9.25 min. Mass spectrum: ESI-MS (+): *m/z* calcd 1489.49 $[M+H]^+$, found 1489.63; *m/z* calcd 745.01 $[M+2H]^{2+}$, found 745.69.

^1H NMR (600 MHz, D2O): δ = 7.95 (d, J = 7.8 Hz, 1 H), 7.48 (t, J = 7.7 Hz, 1 H), 7.41 (t, J = 8.0 Hz, 1 H), 7.32 (d, J = 8.0 Hz, 2 H), 7.28 (d, J = 7.5 Hz, 1 H), 7.10 (d, J = 8.2 Hz, 1 H), 7.08–6.98 (m, 4 H), 6.81 (d, J = 7.9 Hz, 1 H), 5.02 (bs, 1 H), 4.96 (m, 3 H), 4.92 (bs, 1 H), 4.82 (m, 2 H), 4.05 (d, J = 13.4 Hz, 1 H), 4.00–3.18 (m, 39 H), 3.15–2.96 (m, 2 H).

6.4.2.3 Synthesis of iron(III) complexes $[Fe(3a\text{-}DFX)_2]^-$ and $[Fe(6a\text{-}DFX)_2]^-$

1 equivalent ligand was suspended in water, basified to pH 8 with a 1 M aqueous solution of NaOH and heated at 60 °C under magnetic stirring until complete dissolution. 0.5 equivalents of $FeCl_3$ were added to the solution, while maintaining pH 8 with NaOH 1 M. The mixture was heated at 60 °C for 1 h under magnetic stirring. The product was purified by chromatography on Sephadex® G-10 resin using an AKTA Purifier with water as eluent. The pure product was evaporated and freeze dried. For both complexations, a pale red solid was obtained.

6.4.3 Relaxometric measurements

Observed longitudinal relaxation rates ($R_1^{obs} = 1/T_1^{obs}$) values were determined by inversion recovery at 21.5 MHz and 298 K using a Stelar SpinMaster spectrometer (Stelar s.r.l, Mede (PV), Italy). Temperature was controlled with a Stelar VTC-91 airflow heater and the temperature inside the probe checked with a calibrated RS PRO RS55-11 digital thermometer. Data were acquired using a recovery time ≥ 5 x T_1 and with 2 scans per data point. The absolute error in R_{1obs} measurements was less than 1%.

The iron concentration of the investigated solutions of the $Fe(DFX)_2$ complex was determined by the procedure reported in literature.[131] Briefly, the iron complex containing solutions were mixed in a 1:10 ratio with 69% HNO_3 and heated in sealed vials at 120 °C overnight to yield a solution of Fe^{3+} aqua ion. The R_{1obs} of the solution was measured at 298 K and 21.5 MHz and the concentration determined using the equation: $R_{1obs} = R_{1d} + r_{1p}^{Fe}$ [Fe], where R_{1d} is the diamagnetic contribution (0.48 s^{-1}) and r_{1p}^{Fe} is the Fe^{3+} aqua ion relaxivity (18.47 $mM^{-1}s^{-1}$) under the same experimental conditions. The iron concentration of the complexes was confirmed by ICP-MS analysis.

Longitudinal relaxivity (r_1) values reported in Table 6.1 were calculated as slope of the lines correlating observed relaxation rates measured at pH = 7.4, 298 K and 0.47 T as a function of Fe concentration.

6.4.3.1 NMRD profiles

NMRD profiles were obtained using a Stelar SmartTracer FFC NMR relaxometer from 0.01 to 10 MHz. Additional data in the 20 − 80 MHz frequency range were obtained with a High

Field Relaxometer (Stelar) equipped with the HTS-110 3T Metrology cryogen-free superconducting magnet and a Bruker WP80 NMR electromagnet (21.5 – 80 MHz), both equipped with a Stelar VTC-91 for temperature control; the temperature inside the probe was checked with a calibrated RS PRO RS55-11 digital thermometer. Aqueous and human serum solutions of the complex were measured at 298 K. The NMRD profiles data were fitted using the Solomon-Bloembergen-Morgan and Freed's models.

6.4.3.2 ^{17}O-R_2-NMR measurements

^{17}O-NMR measurements were recorded at 14.1 T on a Bruker Avance 600 spectrometer at variable temperature, with a D_2O capillary for sample locking. Samples contained 1% of $H_2{}^{17}O$ (Cambridge Isotope) and the Fe(III) complexes (20 mM Fe(3a-DFX)$_2$, 20 mM Fe(6a-DFX)$_2$). The width at half maximum ($\Delta\omega_{dia}$) of the $H_2{}^{17}O$ signal in pure water was measured over the investigated temperature range and subtracted from the width at half maximum ($\Delta\omega_{Fe}$) of the test solutions containing the Fe-complexes. Then, R_2 was calculated as follows: $R_2=\pi[\Delta\omega_{Fe}-\Delta\omega_{dia}]$.

6.4.3.3 Proton relaxation enhancement (PRE) fitting equations

HSA binding parameters were determined using the PRE method, which considers the relaxation enhancement due to the formation of a slowly moving macromolecular adduct, considering the following equilibrium, with the association constant defined as follows:

$$Fe(L)_2 + nHSA \leftrightarrow Fe(L)_2\text{-}HSA \quad (1)$$

$$K_a = \frac{[Fe(L)2-HSA]}{[Fe(L)2]\,[nHSA]} \quad (2)$$

where n is the number of independent binding sites and K_a the apparent binding constant.

Moreover:

$$[Fe(L)_2]_{tot} = [Fe(L)_2]_{free} + [Fe(L)_2\text{-}HSA] \quad (3)$$

and

$$[HSA]_{tot} = [HSA]_{free} + [Fe(L)_2\text{-}HSA] \quad (4)$$

R_{1obs} was defined as follows:

$$R_{1obs} = R_{1p} + R_{1d} = r_1\,[Fe(L)_2] + r_1{}^b\,[Fe(L)_2\text{-}HSA] + R_{1d} \quad (5)$$

Where R_{1p} and R_{1d} are the paramagnetic and diamagnetic contributions to the observed relaxation rates, respectively. And r_1 and $r_1{}^b$ are the millimolar relaxivities of the iron complex free and bound to HSA, respectively.

The diamagnetic contribution (R_{1d}) was determined as a function of increasing HSA concentration in PBS and included in the fitting function derived from combination of equations 1-5:

$$R_{1obs} = \frac{(K_A[Fe(L)_2]_{tot} + nK_A[HSA]_{tot} + 1) - \sqrt{(K_A[Fe(L)_2]_{tot} + nK_A[HSA]_{tot} + 1)^2 - 4K_A^2[Fe(L)_2]_{tot}\,n[HSA]_{tot}}}{2K_A}$$

$$\times (r_1^b - r_1 + r_1[Fe(L)_2]_{tot}) \times 1000 + (0.25 \times [HSA]_{tot} \times 1000) + 0.359$$

General conclusion

During this PhD project various metal complexes based on paramagnetic metals were investigated mainly for their potential applications as MRI T_1 contrast agents.

The studies on the gadolinium complexes, described in the second and third chapter, offer important contribution for the advance in fully understanding the molecular and structural dynamics of a largely used class of pharmaceuticals like GBCAs. Indeed, research in this topic is primarily focused on their efficiency improvement in order to lower the administered doses.

The forth chapter showed that complexes based on paramagnetic metals can also be adopted as responsive agents for the *in vivo* measurement of specific biomarkers thanks to innovative approaches making use of other imaging techniques.

The fifth and sixth chapter showed that Fe(III)-complexes can be very appealing for MRI applications, as they can offer a valuable and more biocompatible alternative to GBCAs, although intensive research in the next years is still needed to bring this class of compounds closer to clinical translation.

In these years of PhD, many branches of chemistry were touched: from organic, inorganic, medicinal chemistry, to radiochemistry interfaced during the period abroad spent in Texas. Both in Torino and in Houston, I had the opportunity to collaborate with extraordinary multidisciplinary teams composed by people with strong expertise in biotechnology, physics, medicine and I tried to learn as much as possible from them.

References

(1) van Geuns, R.-J. M.; Wielopolski, P. A.; de Bruin, H. G.; Rensing, B. J.; van Ooijen, P. M. A.; Hulshoff, M.; Oudkerk, M.; de Feyter, P. J. Basic Principles of Magnetic Resonance Imaging. *Prog. Cardiovasc. Dis.* **1999**, *42* (2), 149–156. https://doi.org/10.1016/S0033-0620(99)70014-9.

(2) Dale, B. M.; Brown, M. A.; Semelka, R. C. Principles of Magnetic Resonance Imaging - 1. In *MRI Basic Principles and Applications*; John Wiley & Sons, Ltd, 2015; pp 26–38. https://doi.org/10.1002/9781119013068.ch4.

(3) Cleary, J. O. S. H.; Guimarães, A. R. Magnetic Resonance Imaging. In *Pathobiology of Human Disease*; McManus, L. M., Mitchell, R. N., Eds.; Academic Press: San Diego, 2014; pp 3987–4004. https://doi.org/10.1016/B978-0-12-386456-7.07609-7.

(4) Brown, M. A.; Semelka, R. C. Concepts of Magnetic Resonance. In *MRI: Basic Principles and Applications*; John Wiley & Sons, Ltd, 2003; pp 11–19. https://doi.org/10.1002/0471467936.ch2.

(5) McRobbie, D. W.; Moore, E. A.; Graves, M. J.; Prince, M. R. *MRI from Picture to Proton*, 2nd ed.; Cambridge University Press: Cambridge, 2006. https://doi.org/10.1017/CBO9780511545405.

(6) Lauterbur, P. C. Magnetic Resonance Zeugmatography. *Pure Appl. Chem.* **1974**, *40* (1–2), 149–157. https://doi.org/10.1351/pac197440010149.

(7) Merbach, A. S.; Helm, L.; Tóth, É. *The Chemistry of Contrast Agents in Medical Magnetic Resonance Imaging*; John Wiley & Sons, 2013.

(8) Wahsner, J.; Gale, E. M.; Rodríguez-Rodríguez, A.; Caravan, P. Chemistry of MRI Contrast Agents: Current Challenges and New Frontiers. *Chem. Rev.* **2019**, *119* (2), 957–1057. https://doi.org/10.1021/acs.chemrev.8b00363.

(9) Lohrke, J.; Frenzel, T.; Endrikat, J.; Alves, F. C.; Grist, T. M.; Law, M.; Lee, J. M.; Leiner, T.; Li, K.-C.; Nikolaou, K.; Prince, M. R.; Schild, H. H.; Weinreb, J. C.; Yoshikawa, K.; Pietsch, H. 25 Years of Contrast-Enhanced MRI: Developments, Current Challenges and Future Perspectives. *Adv. Ther.* **2016**, *33* (1), 1–28. https://doi.org/10.1007/s12325-015-0275-4.

(10) Serkova, N. J. Nanoparticle-Based Magnetic Resonance Imaging on Tumor-Associated Macrophages and Inflammation. *Front. Immunol.* **2017**, *8: 590*. https://doi.org/10.3389/fimmu.2017.00590.

(11) Aime, S.; Botta, M.; Terreno, E. Gd(III)-Based Contrast Agents For MRI. In *Advances in Inorganic Chemistry*; Academic Press, 2005; Vol. 57, pp 173–237. https://doi.org/10.1016/S0898-8838(05)57004-1.

(12) Jacques, V.; Dumas, S.; Sun, W.-C.; Troughton, J. S.; Greenfield, M. T.; Caravan, P. High-Relaxivity Magnetic Resonance Imaging Contrast Agents Part 2: Optimization of Inner- and Second-Sphere Relaxivity. *Invest. Radiol.* **2010**, *45* (10), 613–624. https://doi.org/10.1097/RLI.0b013e3181ee6a49.

(13) Burtea, C.; Laurent, S.; Vander Elst, L.; Muller, R. N. Contrast Agents: Magnetic Resonance. In *Molecular Imaging I*; Semmler, W., Schwaiger, M., Eds.; Handbook of

Experimental Pharmacology; Springer: Berlin, Heidelberg, 2008; pp 135–165. https://doi.org/10.1007/978-3-540-72718-7_7.
(14) Aime, S.; Gianolio, E.; Viale, A. Relaxometry and Contrast Agents. In *Paramagnetism in Experimental Biomolecular NMR*; 2018; pp 189–218. https://doi.org/10.1039/9781788013291-00189.
(15) Clough, T. J.; Jiang, L.; Wong, K.-L.; Long, N. J. Ligand Design Strategies to Increase Stability of Gadolinium-Based Magnetic Resonance Imaging Contrast Agents. *Nat. Commun.* **2019**, *10* (1), 1420. https://doi.org/10.1038/s41467-019-09342-3.
(16) Giardiello, M.; Botta, M.; Lowe, M. P. Synthesis of Lanthanide(III) Complexes Appended with a Diphenylphosphinamide and Their Interaction with Human Serum Albumin. *J. Incl. Phenom. Macrocycl. Chem.* **2011**, *71* (3), 435–444. https://doi.org/10.1007/s10847-011-0009-4.
(17) Kanal, E.; Tweedle, M. F. Residual or Retained Gadolinium: Practical Implications for Radiologists and Our Patients. *Radiology* **2015**, *275* (3), 630–634. https://doi.org/10.1148/radiol.2015150805.
(18) Lange, S.; Mędrzycka-Dąbrowska, W.; Zorena, K.; Dąbrowski, S.; Ślęzak, D.; Malecka-Dubiela, A.; Rutkowski, P. Nephrogenic Systemic Fibrosis as a Complication after Gadolinium-Containing Contrast Agents: A Rapid Review. *Int. J. Environ. Res. Public. Health* **2021**, *18* (6), 3000. https://doi.org/10.3390/ijerph18063000.
(19) Lancelot, E.; Desché, P. Gadolinium Retention as a Safety Signal: Experience of a Manufacturer. *Invest. Radiol.* **2020**, *55* (1), 20. https://doi.org/10.1097/RLI.0000000000000605.
(20) McDonald, R. J.; Levine, D.; Weinreb, J.; Kanal, E.; Davenport, M. S.; Ellis, J. H.; Jacobs, P. M.; Lenkinski, R. E.; Maravilla, K. R.; Prince, M. R.; Rowley, H. A.; Tweedle, M. F.; Kressel, H. Y. Gadolinium Retention: A Research Roadmap from the 2018 NIH/ACR/RSNA Workshop on Gadolinium Chelates. *Radiology* **2018**, *289* (2), 517–534. https://doi.org/10.1148/radiol.2018181151.
(21) Robert, P.; Fingerhut, S.; Factor, C.; Vives, V.; Letien, J.; Sperling, M.; Rasschaert, M.; Santus, R.; Ballet, S.; Idée, J.-M.; Corot, C.; Karst, U. One-Year Retention of Gadolinium in the Brain: Comparison of Gadodiamide and Gadoterate Meglumine in a Rodent Model. *Radiology* **2018**, *288* (2), 424–433. https://doi.org/10.1148/radiol.2018172746.
(22) Bower, D. V.; Richter, J. K.; von Tengg-Kobligk, H.; Heverhagen, J. T.; Runge, V. M. Gadolinium-Based MRI Contrast Agents Induce Mitochondrial Toxicity and Cell Death in Human Neurons, and Toxicity Increases With Reduced Kinetic Stability of the Agent. *Invest. Radiol.* **2019**, *54* (8), 453. https://doi.org/10.1097/RLI.0000000000000567.
(23) Mallio, C. A.; Rovira, À.; Parizel, P. M.; Quattrocchi, C. C. Exposure to Gadolinium and Neurotoxicity: Current Status of Preclinical and Clinical Studies. *Neuroradiology* **2020**, *62* (8), 925–934. https://doi.org/10.1007/s00234-020-02434-8.
(24) Jost, G.; Frenzel, T.; Boyken, J.; Lohrke, J.; Nischwitz, V.; Pietsch, H. Long-Term Excretion of Gadolinium-Based Contrast Agents: Linear versus Macrocyclic Agents in an Experimental Rat Model. *Radiology* **2019**, *290* (2), 340–348. https://doi.org/10.1148/radiol.2018180135.
(25) Gianolio, E.; Bardini, P.; Arena, F.; Stefania, R.; Di Gregorio, E.; Iani, R.; Aime, S. Gadolinium Retention in the Rat Brain: Assessment of the Amounts of Insoluble

Gadolinium-Containing Species and Intact Gadolinium Complexes after Repeated Administration of Gadolinium-Based Contrast Agents. *Radiology* **2017**, *285* (3), 839–849. https://doi.org/10.1148/radiol.2017162857.

(26) Rasschaert, M.; Emerit, A.; Fretellier, N.; Factor, C.; Robert, P.; Idée, J.-M.; Corot, C. Gadolinium Retention, Brain T1 Hyperintensity, and Endogenous Metals: A Comparative Study of Macrocyclic Versus Linear Gadolinium Chelates in Renally Sensitized Rats. *Invest. Radiol.* **2018**, *53* (6), 328. https://doi.org/10.1097/RLI.0000000000000447.

(27) Trapasso, G.; Chiesa, S.; Freitas, R.; Pereira, E. What Do We Know about the Ecotoxicological Implications of the Rare Earth Element Gadolinium in Aquatic Ecosystems? *Sci. Total Environ.* **2021**, *781*, 146273. https://doi.org/10.1016/j.scitotenv.2021.146273.

(28) Brünjes, R.; Hofmann, T. Anthropogenic Gadolinium in Freshwater and Drinking Water Systems. *Water Res.* **2020**, *182*, 115966. https://doi.org/10.1016/j.watres.2020.115966.

(29) Chen, S.; An, L.; Yang, S. Low-Molecular-Weight Fe(III) Complexes for MRI Contrast Agents. *Molecules* **2022**, *27* (14), 4573. https://doi.org/10.3390/molecules27144573.

(30) Kras, E. A.; Snyder, E. M.; Sokolow, G. E.; Morrow, J. R. Distinct Coordination Chemistry of Fe(III)-Based MRI Probes. *Acc. Chem. Res.* **2022**, *55* (10), 1435–1444. https://doi.org/10.1021/acs.accounts.2c00102.

(31) Baranyai, Z.; Carniato, F.; Nucera, A.; Horváth, D.; Tei, L.; Platas-Iglesias, C.; Botta, M. Defining the Conditions for the Development of the Emerging Class of Fe III -Based MRI Contrast Agents. *Chem. Sci.* **2021**, *12* (33), 11138–11145. https://doi.org/10.1039/D1SC02200H.

(32) Nucera, A.; Carniato, F.; Baranyai, Z.; Platas-Iglesias, C.; Botta, M. Characterization of the Fe(III)-Tiron System in Solution through an Integrated Approach Combining NMR Relaxometric, Thermodynamic, Kinetic, and Computational Data. *Inorg. Chem.* **2023**, *62* (10), 4272–4283. https://doi.org/10.1021/acs.inorgchem.2c04393.

(33) Uzal-Varela, R.; Lucio-Martínez, F.; Nucera, A.; Botta, M.; Esteban-Gómez, D.; Valencia, L.; Rodríguez-Rodríguez, A.; Platas-Iglesias, C. A Systematic Investigation of the NMR Relaxation Properties of Fe(III)-EDTA Derivatives and Their Potential as MRI Contrast Agents. *Inorg. Chem. Front.* **2023**, *10* (5), 1633–1649. https://doi.org/10.1039/D2QI02665A.

(34) Asik, D.; Smolinski, R.; Abozeid, S. M.; Mitchell, T. B.; Turowski, S. G.; Spernyak, J. A.; Morrow, J. R. Modulating the Properties of Fe(III) Macrocyclic MRI Contrast Agents by Appending Sulfonate or Hydroxyl Groups. *Molecules* **2020**, *25* (10), 2291. https://doi.org/10.3390/molecules25102291.

(35) Cineus, R.; Abozeid, S. M.; Sokolow, G. E.; Spernyak, J. A.; Morrow, J. R. Fe(III) T1 MRI Probes Containing Phenolate or Hydroxypyridine-Appended Triamine Chelates and a Coordination Site for Bound Water. *Inorg. Chem.* **2023**, *62* (40), 16513–16522. https://doi.org/10.1021/acs.inorgchem.3c02344.

(36) Snyder, E. M.; Asik, D.; Abozeid, S. M.; Burgio, A.; Bateman, G.; Turowski, S. G.; Spernyak, J. A.; Morrow, J. R. A Class of FeIII Macrocyclic Complexes with Alcohol Donor Groups as Effective T1 MRI Contrast Agents. *Angew. Chem.* **2020**, *132* (6), 2435–2440. https://doi.org/10.1002/ange.201912273.

(37) Sokolow, G. E.; Crawley, M. R.; Morphet, D. R.; Asik, D.; Spernyak, J. A.; McGray, A. J. R.; Cook, T. R.; Morrow, J. R. Metal−Organic Polyhedron with Four Fe(III) Centers Producing Enhanced T1 Magnetic Resonance Imaging Contrast in Tumors. *Inorg. Chem.* **2022**, *61* (5), 2603–2611. https://doi.org/10.1021/acs.inorgchem.1c03660.
(38) Wan, Y.; An, L.; Zhu, Z.; Tian, Q.; Lin, J.; Yang, S. Iron–Polyphenol Dendritic Complexes for Regulating Amplification of Phenolic Hydroxyl Groups to Improve Magnetic Resonance Imaging. *Chem. Eng. J.* **2023**, *458*, 141322. https://doi.org/10.1016/j.cej.2023.141322.
(39) Kuźnik, N.; Wyskocka, M. Iron(III) Contrast Agent Candidates for MRI: A Survey of the Structure–Effect Relationship in the Last 15 -Years of Studies. *Eur. J. Inorg. Chem.* **2016**, *2016* (4), 445–458. https://doi.org/10.1002/ejic.201501166.
(40) Koppenol, W. H.; Hider, R. H. Iron and Redox Cycling. Do's and Don'ts. *Free Radic. Biol. Med.* **2019**, *133*, 3–10. https://doi.org/10.1016/j.freeradbiomed.2018.09.022.
(41) Hingorani, D. V.; Bernstein, A. S.; Pagel, M. D. A Review of Responsive MRI Contrast Agents: 2005–2014. *Contrast Media Mol. Imaging* **2015**, *10* (4), 245–265. https://doi.org/10.1002/cmmi.1629.
(42) Yoo, B.; Pagel, M. D. An Overview of Responsive MRI Contrast Agents for Molecular Imaging. *Front. Biosci.-Landmark* **2008**, *13* (5), 1733–1752. https://doi.org/10.2741/2796.
(43) Frullano, L.; Catana, C.; Benner, T.; Sherry, A. D.; Caravan, P. Bimodal MR–PET Agent for Quantitative pH Imaging. *Angew. Chem. Int. Ed.* **2010**, *49* (13), 2382–2384. https://doi.org/10.1002/anie.201000075.
(44) Pollard, A. C.; de la Cerda, J.; Schuler, F. W.; Pollard, T. R.; Kotrotsou, A.; Pisaneschi, F.; Pagel, M. D. Radiometal-Based PET/MRI Contrast Agents for Sensing Tumor Extracellular pH. *Biosensors* **2022**, *12* (2), 134. https://doi.org/10.3390/bios12020134.
(45) Aime, S.; Botta, M.; Fasano, M.; Terreno, E. Lanthanide(III) Chelates for NMR Biomedical Applications. *Chem. Soc. Rev.* **1998**, *27* (1), 19–29. https://doi.org/10.1039/A827019Z.
(46) Aime, S.; Gianolio, E.; Terreno, E.; Giovenzana, G. B.; Pagliarin, R.; Sisti, M.; Palmisano, G.; Botta, M.; Lowe, M. P.; Parker, D. Ternary Gd(III)L-HSA Adducts: Evidence for the Replacement of Inner-Sphere Water Molecules by Coordinating Groups of the Protein. Implications for the Design of Contrast Agents for MRI. *JBIC J. Biol. Inorg. Chem.* **2000**, *5* (4), 488–497. https://doi.org/10.1007/PL00021449.
(47) Lowe, M. P.; Parker, D.; Reany, O.; Aime, S.; Botta, M.; Castellano, G.; Gianolio, E.; Pagliarin, R. pH-Dependent Modulation of Relaxivity and Luminescence in Macrocyclic Gadolinium and Europium Complexes Based on Reversible Intramolecular Sulfonamide Ligation. *J. Am. Chem. Soc.* **2001**, *123* (31), 7601–7609. https://doi.org/10.1021/ja0103647.
(48) Robic, C.; Port, M.; Rousseaux, O.; Louguet, S.; Fretellier, N.; Catoen, S.; Factor, C.; Le Greneur, S.; Medina, C.; Bourrinet, P.; Raynal, I.; Idée, J.-M.; Corot, C. Physicochemical and Pharmacokinetic Profiles of Gadopiclenol. *Invest. Radiol.* **2019**, *54* (8), 475–484. https://doi.org/10.1097/RLI.0000000000000563.
(49) Oyane, A.; Onuma, K.; Ito, A.; Kim, H.-M.; Kokubo, T.; Nakamura, T. Formation and Growth of Clusters in Conventional and New Kinds of Simulated Body Fluids. *J. Biomed. Mater. Res. A* **2003**, *64A* (2), 339–348. https://doi.org/10.1002/jbm.a.10426.

(50) Gianolio, E.; Cabella, C.; Colombo Serra, S.; Valbusa, G.; Arena, F.; Maiocchi, A.; Miragoli, L.; Tedoldi, F.; Uggeri, F.; Visigalli, M.; Bardini, P.; Aime, S. B25716/1: A Novel Albumin-Binding Gd-AAZTA MRI Contrast Agent with Improved Properties in Tumor Imaging. *JBIC J. Biol. Inorg. Chem.* **2014**, *19* (4), 715–726. https://doi.org/10.1007/s00775-014-1111-z.

(51) Aime, S.; Botta, M.; Fasano, M.; Terreno, E. Prototropic and Water-Exchange Processes in Aqueous Solutions of Gd(III) Chelates. *Acc. Chem. Res.* **1999**, *32* (11), 941–949. https://doi.org/10.1021/ar970300u.

(52) Swift, T. J.; Connick, R. E. NMR-Relaxation Mechanisms of O17 in Aqueous Solutions of Paramagnetic Cations and the Lifetime of Water Molecules in the First Coordination Sphere. *J. Chem. Phys.* **2004**, *37* (2), 307–320. https://doi.org/10.1063/1.1701321.

(53) Laurent, S.; Vander Elst, L.; Henoumont, C.; Muller, R. N. How to Measure the Transmetallation of a Gadolinium Complex. *Contrast Media Mol. Imaging* **2010**, *5* (6), 305–308. https://doi.org/10.1002/cmmi.388.

(54) Dougherty, D. A. The Cation−π Interaction. *Acc. Chem. Res.* **2013**, *46* (4), 885–893. https://doi.org/10.1021/ar300265y.

(55) Meot-Ner, M.; Deakyne, C. A. Unconventional Ionic Hydrogen Bonds. 1. CH.Delta.+.Cntdot..Cntdot..Cntdot.X. Complexes of Quaternary Ions with n- and .Pi.-Donors. *J. Am. Chem. Soc.* **1985**, *107* (2), 469–474. https://doi.org/10.1021/ja00288a033.

(56) Schultz, J. The Nature and Origin of the Serum Proteins. In *Amino Acids and Serum Proteins*; Advances in Chemistry; American Chemical Society, 1964; Vol. 44, pp 1–16. https://doi.org/10.1021/ba-1964-0044.ch001.

(57) Roveri, O. A.; Braslavsky, S. E. π-Cation Interactions as the Origin of the Weak Absorption at 532 Nm Observed in Tryptophan-Containing Polypeptides. *Photochem. Photobiol. Sci.* **2012**, *11* (6), 962–966. https://doi.org/10.1039/c2pp05341a.

(58) Peters, T. Jr. *All About Albumin: Biochemistry, Genetics, and Medical Applications*; Academic Press, 1995.

(59) Tayubi, I. A.; Sethumadhavan, R. Nature of Cation-π Interactions and Their Role in Structural Stability of Immunoglobulin Proteins. *Biochem. Mosc.* **2010**, *75* (7), 912–918. https://doi.org/10.1134/S000629791007014X.

(60) Mizerska, U.; Fortuniak, W.; Pospiech, P.; Chojnowski, J.; Slomkowski, S. Gamma Globulins Adsorption on Carbofunctional Polysiloxane Microspheres. *J. Inorg. Organomet. Polym. Mater.* **2015**, *25* (3), 507–514. https://doi.org/10.1007/s10904-015-0209-2.

(61) Gallivan, J. P.; Dougherty, D. A. Cation-π Interactions in Structural Biology. *Proc. Natl. Acad. Sci.* **1999**, *96* (17), 9459–9464. https://doi.org/10.1073/pnas.96.17.9459.

(62) Ma, J. C.; Dougherty, D. A. The Cation−π Interaction. *Chem. Rev.* **1997**, *97* (5), 1303–1324. https://doi.org/10.1021/cr9603744.

(63) Digilio, G.; Bracco, C.; Barbero, L.; Chicco, D.; Del Curto, M. D.; Esposito, P.; Traversa, S.; Aime, S. NMR Conformational Analysis of Antide, a Potent Antagonist of the Gonadotropin Releasing Hormone. *J. Am. Chem. Soc.* **2002**, *124* (13), 3431–3442. https://doi.org/10.1021/ja0115464.

(64) Gebbie, M. A.; Wei, W.; Schrader, A. M.; Cristiani, T. R.; Dobbs, H. A.; Idso, M.; Chmelka, B. F.; Waite, J. H.; Israelachvili, J. N. Tuning Underwater Adhesion with

Cation–π Interactions. *Nat. Chem.* **2017**, *9* (5), 473–479. https://doi.org/10.1038/nchem.2720.
(65) Dastrù, W.; Menchise, V.; Ferrauto, G.; Fabretto, S.; Carrera, C.; Terreno, E.; Aime, S.; Castelli, D. D. Modulation of the Prototropic Exchange Rate in pH-Responsive Yb-HPDO3A Derivatives as ParaCEST Agents. *ChemistrySelect* **2018**, *3* (22), 6035–6041. https://doi.org/10.1002/slct.201800283.
(66) Aime, S.; Botta, M.; Fasano, M.; Marques, M. P. M.; Geraldes, C. F. G. C.; Pubanz, D.; Merbach, A. E. Conformational and Coordination Equilibria on DOTA Complexes of Lanthanide Metal Ions in Aqueous Solution Studied by 1H-NMR Spectroscopy. *Inorg. Chem.* **1997**, *36* (10), 2059–2068. https://doi.org/10.1021/ic961364o.
(67) Woods, M.; Aime, S.; Botta, M.; Howard, J. A. K.; Moloney, J. M.; Navet, M.; Parker, D.; Port, M.; Rousseaux, O. Correlation of Water Exchange Rate with Isomeric Composition in Diastereoisomeric Gadolinium Complexes of Tetra(Carboxyethyl)DOTA and Related Macrocyclic Ligands. *J. Am. Chem. Soc.* **2000**, *122* (40), 9781–9792. https://doi.org/10.1021/ja994492v.
(68) Tircso, G.; Webber, B. C.; Kucera, B. E.; Young, V. G.; Woods, M. Analysis of the Conformational Behavior and Stability of the SAP and TSAP Isomers of Lanthanide(III) NB-DOTA-Type Chelates. *Inorg. Chem.* **2011**, *50* (17), 7966–7979. https://doi.org/10.1021/ic2012843.
(69) Di Gregorio, E.; Lattuada, L.; Maiocchi, A.; Aime, S.; Ferrauto, G.; Gianolio, E. Supramolecular Adducts between Macrocyclic Gd(III) Complexes and Polyaromatic Systems: A Route to Enhance the Relaxivity through the Formation of Hydrophobic Interactions. *Chem. Sci.* **2021**, *12* (4), 1368–1377. https://doi.org/10.1039/D0SC03504A.
(70) Klein, B. Standardization of Serum Protein Analyses. *Ann. Clin. Lab. Sci.* **1978**, *8* (3), 249–253.
(71) Aime, S.; Botta, M.; Fasano, M.; Crich, S. G.; Terreno, E. Gd(III) Complexes as Contrast Agents for Magnetic Resonance Imaging: A Proton Relaxation Enhancement Study of the Interaction with Human Serum Albumin. *JBIC J. Biol. Inorg. Chem.* **1996**, *1* (4), 312–319. https://doi.org/10.1007/s007750050059.
(72) Yamauchi, M.; Sricholpech, M. Lysine Post-Translational Modifications of Collagen. *Essays Biochem.* **2012**, *52*, 113–133. https://doi.org/10.1042/bse0520113.
(73) Zarembinski, T. I.; Skardal, A.; Zarembinski, T. I.; Skardal, A. HyStem®: A Unique Clinical Grade Hydrogel for Present and Future Medical Applications. In *Hydrogels - Smart Materials for Biomedical Applications*; IntechOpen, 2018. https://doi.org/10.5772/intechopen.81344.
(74) Delli Castelli, D.; Caligara, M. C.; Botta, M.; Terreno, E.; Aime, S. Combined High Resolution NMR and 1H and 17O Relaxometric Study Sheds Light on the Solution Structure and Dynamics of the Lanthanide(III) Complexes of HPDO3A. *Inorg. Chem.* **2013**, *52* (12), 7130–7138. https://doi.org/10.1021/ic400716c.
(75) Tear, L. R.; Carrera, C.; Gianolio, E.; Aime, S. Towards an Improved Design of MRI Contrast Agents: Synthesis and Relaxometric Characterisation of Gd-HPDO3A Analogues. *Chem. – Eur. J.* **2020**, *26* (27), 6056–6063. https://doi.org/10.1002/chem.202000479.
(76) Tear, L. R.; Carrera, C.; Dhakan, C. B.; Cavallari, E.; Travagin, F.; Calcagno, C.; Aime, S.; Gianolio, E. An Albumin-Binding Gd-HPDO3A Contrast Agent for Improved

Intravascular Retention. *Inorg. Chem. Front.* **2021**, *8* (17), 4014–4025. https://doi.org/10.1039/D1QI00128K.
(77) Aime, S.; Baranyai, Z. How the Catalysis of the Prototropic Exchange Affects the Properties of Lanthanide(III) Complexes in Their Applications as MRI Contrast Agents. *Inorganica Chim. Acta* **2022**, *532*, 120730. https://doi.org/10.1016/j.ica.2021.120730.
(78) Boros, E.; Srinivas, R.; Kim, H.-K.; Raitsimring, A. M.; Astashkin, A. V.; Poluektov, O. G.; Niklas, J.; Horning, A. D.; Tidor, B.; Caravan, P. Intramolecular Hydrogen Bonding Restricts Gd–Aqua-Ligand Dynamics. *Angew. Chem. Int. Ed.* **2017**, *56* (20), 5603–5606. https://doi.org/10.1002/anie.201702274.
(79) Aime, S.; Baroni, S.; Delli Castelli, D.; Brücher, E.; Fábián, I.; Serra, S. C.; Fringuello Mingo, A.; Napolitano, R.; Lattuada, L.; Tedoldi, F.; Baranyai, Z. Exploiting the Proton Exchange as an Additional Route to Enhance the Relaxivity of Paramagnetic MRI Contrast Agents. *Inorg. Chem.* **2018**, *57* (9), 5567–5574. https://doi.org/10.1021/acs.inorgchem.8b00521.
(80) Baroni, S.; Maria Carnovale, I.; Carrera, C.; Boccalon, M.; Guidolin, N.; Demitri, N.; Lattuada, L.; Tedoldi, F.; Baranyai, Z.; Aime, S. H-Bonding and Intramolecular Catalysis of Proton Exchange Affect the CEST Properties of Eu III Complexes with HP-DO3A-like Ligands. *Chem. Commun.* **2021**, *57* (26), 3287–3290. https://doi.org/10.1039/D1CC00366F.
(81) Lattuada, L.; Horváth, D.; Serra, S. C.; Mingo, A. F.; Minazzi, P.; Bényei, A.; Forgács, A.; Fedeli, F.; Gianolio, E.; Aime, S.; B. Giovenzana, G.; Baranyai, Z. Enhanced Relaxivity of Gd III -Complexes with HP-DO3A-like Ligands upon the Activation of the Intramolecular Catalysis of the Prototropic Exchange. *Inorg. Chem. Front.* **2021**, *8* (6), 1500–1510. https://doi.org/10.1039/D0QI01333A.
(82) Di Gregorio, E.; Boccalon, M.; Furlan, C.; Gianolio, E.; Bényei, A.; Aime, S.; Baranyai, Z.; Ferrauto, G. Studies of the Hydrophobic Interaction between a Pyrene-Containing Dye and a Tetra-Aza Macrocyclic Gadolinium Complex. *Inorg. Chem. Front.* **2022**, *9* (14), 3494–3504. https://doi.org/10.1039/D2QI00596D.
(83) Batys, P.; Morga, M.; Bonarek, P.; Sammalkorpi, M. pH-Induced Changes in Polypeptide Conformation: Force-Field Comparison with Experimental Validation. *J. Phys. Chem. B* **2020**, *124* (14), 2961–2972. https://doi.org/10.1021/acs.jpcb.0c01475.
(84) Warburg, O. On the Origin of Cancer Cells. *Science* **1956**, *123* (3191), 309–314. https://doi.org/10.1126/science.123.3191.309.
(85) Vander Heiden, M. G.; Cantley, L. C.; Thompson, C. B. Understanding the Warburg Effect: The Metabolic Requirements of Cell Proliferation. *Science* **2009**, *324* (5930), 1029–1033. https://doi.org/10.1126/science.1160809.
(86) Ibrahim-Hashim, A.; Estrella, V. Acidosis and Cancer: From Mechanism to Neutralization. *Cancer Metastasis Rev.* **2019**, *38* (1), 149–155. https://doi.org/10.1007/s10555-019-09787-4.
(87) Estrella, V.; Chen, T.; Lloyd, M.; Wojtkowiak, J.; Cornnell, H. H.; Ibrahim-Hashim, A.; Bailey, K.; Balagurunathan, Y.; Rothberg, J. M.; Sloane, B. F.; Johnson, J.; Gatenby, R. A.; Gillies, R. J. Acidity Generated by the Tumor Microenvironment Drives Local Invasion. *Cancer Res.* **2013**, *73* (5), 1524–1535. https://doi.org/10.1158/0008-5472.CAN-12-2796.

(88) Robey, I. F.; Baggett, B. K.; Kirkpatrick, N. D.; Roe, D. J.; Dosescu, J.; Sloane, B. F.; Hashim, A. I.; Morse, D. L.; Raghunand, N.; Gatenby, R. A.; Gillies, R. J. Bicarbonate Increases Tumor pH and Inhibits Spontaneous Metastases. *Cancer Res.* **2009**, *69* (6), 2260–2268. https://doi.org/10.1158/0008-5472.CAN-07-5575.

(89) Chen, L. Q.; Randtke, E. A.; Jones, K. M.; Moon, B. F.; Howison, C. M.; Pagel, M. D. Evaluations of Tumor Acidosis Within In Vivo Tumor Models Using Parametric Maps Generated with AcidoCEST MRI. *Mol. Imaging Biol.* **2015**, *17* (4), 488–496. https://doi.org/10.1007/s11307-014-0816-2.

(90) Akhenblit, P. J.; Pagel, M. D. Recent Advances in Targeting Tumor Energy Metabolism with Tumor Acidosis as a Biomarker of Drug Efficacy. *J. Cancer Sci. Ther.* **2016**, *8* (1), 20–29. https://doi.org/10.4172/1948-5956.1000382.

(91) Akhenblit, P. J.; Hanke, N. T.; Gill, A.; Persky, D. O.; Howison, C. M.; Pagel, M. D.; Baker, A. F. Assessing Metabolic Changes in Response to mTOR Inhibition in a Mantle Cell Lymphoma Xenograft Model Using AcidoCEST MRI. *Mol. Imaging* **2016**, *15*, 1536012116645439. https://doi.org/10.1177/1536012116645439.

(92) Zhang, A.; Yao, L.; An, M. Reversing the Undesirable pH-Profile of Doxorubicin via Activation of a Di-Substituted Maleamic Acid Prodrug at Tumor Acidity. *Chem. Commun.* **2017**, *53* (95), 12826–12829. https://doi.org/10.1039/C7CC06843C.

(93) Klaus, T.; Deshmukh, S. pH-Responsive Antibodies for Therapeutic Applications. *J. Biomed. Sci.* **2021**, *28* (1), 11. https://doi.org/10.1186/s12929-021-00709-7.

(94) Chen, L. Q.; Howison, C. M.; Jeffery, J. J.; Robey, I. F.; Kuo, P. H.; Pagel, M. D. Evaluations of Extracellular pH within in Vivo Tumors Using acidoCEST MRI. *Magn. Reson. Med.* **2014**, *72* (5), 1408–1417. https://doi.org/10.1002/mrm.25053.

(95) Longo, D. L.; Dastrù, W.; Digilio, G.; Keupp, J.; Langereis, S.; Lanzardo, S.; Prestigio, S.; Steinbach, O.; Terreno, E.; Uggeri, F.; Aime, S. Iopamidol as a Responsive MRI-Chemical Exchange Saturation Transfer Contrast Agent for pH Mapping of Kidneys: In Vivo Studies in Mice at 7 T. *Magn. Reson. Med.* **2011**, *65* (1), 202–211. https://doi.org/10.1002/mrm.22608.

(96) Hvattum, E.; Normann, P. T.; Jamieson, G. C.; Lai, J.-J.; Skotland, T. Detection and Quantitation of Gadolinium Chelates in Human Serum and Urine by High-Performance Liquid Chromatography and Post-Column Derivatization of Gadolinium with Arsenazo III. *J. Pharm. Biomed. Anal.* **1995**, *13* (7), 927–932. https://doi.org/10.1016/0731-7085(95)01311-8.

(97) Shannon, R. D. Revised Effective Ionic Radii and Systematic Studies of Interatomic Distances in Halides and Chalcogenides. *Acta Crystallogr. Sect. A* **1976**, *32* (5), 751–767. https://doi.org/10.1107/S0567739476001551.

(98) Cotton, S. A. Scandium, Yttrium & the Lanthanides: Inorganic & Coordination Chemistry. In *Encyclopedia of Inorganic Chemistry*; John Wiley & Sons, Ltd, 2006. https://doi.org/10.1002/0470862106.ia211.

(99) Shirley, M.; Plosker, G. L. Deferasirox: A Review of Its Use for Chronic Iron Overload in Patients with Non-Transfusion-Dependent Thalassaemia. *Drugs* **2014**, *74* (9), 1017–1027. https://doi.org/10.1007/s40265-014-0238-0.

(100) Moukalled, N. M.; Bou-Fakhredin, R.; Taher, A. T. Deferasirox: Over a Decade of Experience in Thalassemia. *Mediterr. J. Hematol. Infect. Dis.* **2018**, *10* (1). https://doi.org/10.4084/MJHID.2018.066.

(101) Cappellini, M. D. Long-Term Efficacy and Safety of Deferasirox. *Blood Rev.* **2008**, *22*, S35–S41. https://doi.org/10.1016/S0268-960X(08)70007-9.
(102) Heinz, U.; Hegetschweiler, K.; Acklin, P.; Faller, B.; Lattmann, R.; Schnebli, H. P. 4-[3,5-Bis(2-Hydroxyphenyl)-1,2,4-Triazol-1-Yl]- Benzoic Acid: A Novel Efficient and Selective Iron(III) Complexing Agent. *Angew. Chem. Int. Ed.* **1999**, *38* (17), 2568–2570. https://doi.org/10.1002/(SICI)1521-3773(19990903)38:17<2568::AID-ANIE2568>3.0.CO;2-C.
(103) Tanaka, C. Clinical Pharmacology of Deferasirox. *Clin. Pharmacokinet.* **2014**, *53* (8), 679–694. https://doi.org/10.1007/s40262-014-0151-4.
(104) Bruin, G. J. M.; Faller, T.; Wiegand, H.; Schweitzer, A.; Nick, H.; Schneider, J.; Boernsen, K.-O.; Waldmeier, F. Pharmacokinetics, Distribution, Metabolism, and Excretion of Deferasirox and Its Iron Complex in Rats. *Drug Metab. Dispos.* **2008**, *36* (12), 2523–2538. https://doi.org/10.1124/dmd.108.022962.
(105) Steinhauser, S.; Heinz, U.; Bartholomä, M.; Weyhermüller, T.; Nick, H.; Hegetschweiler, K. Complex Formation of ICL670 and Related Ligands with FeIII and FeII. *Eur. J. Inorg. Chem.* **2004**, *2004* (21), 4177–4192. https://doi.org/10.1002/ejic.200400363.
(106) Weiss, H. M.; Fresneau, M.; Camenisch, G. P.; Kretz, O.; Gross, G. In Vitro Blood Distribution and Plasma Protein Binding of the Iron Chelator Deferasirox (Icl670) and Its Iron Complex Fe-[Icl670]2 for Rat, Marmoset, Rabbit, Mouse, Dog, and Human. *Drug Metab. Dispos.* **2006**, *34* (6), 971–975. https://doi.org/10.1124/dmd.105.006429.
(107) Dehghan, G.; Shaghaghi, M.; Sattari, S.; Jouyban, A. Interaction of Human Serum Albumin with Fe(III)–Deferasirox Studied by Multispectroscopic Methods. *J. Lumin.* **2014**, *149*, 251–257. https://doi.org/10.1016/j.jlumin.2014.01.047.
(108) Solomon, I. Relaxation Processes in a System of Two Spins. *Phys. Rev.* **1955**, *99* (2), 559–565. https://doi.org/10.1103/PhysRev.99.559.
(109) Bloembergen, N.; Morgan, L. O. Proton Relaxation Times in Paramagnetic Solutions. Effects of Electron Spin Relaxation. *J. Chem. Phys.* **2004**, *34* (3), 842–850. https://doi.org/10.1063/1.1731684.
(110) Bloembergen, N. Proton Relaxation Times in Paramagnetic Solutions. *J. Chem. Phys.* **2004**, *27* (2), 572–573. https://doi.org/10.1063/1.1743771.
(111) Bertini, I.; Capozzi, F.; Luchinat, C.; Xia, Z. Nuclear and Electron Relaxation of Hexaaquairon(3+). *J. Phys. Chem.* **1993**, *97* (6), 1134–1137. https://doi.org/10.1021/j100108a006.
(112) Koenig, S. H.; Brown, R. D.; Lindstrom, T. R. Interactions of Solvent with the Heme Region of Methemoglobin and Fluoro-Methemoglobin. *Biophys. J.* **1981**, *34* (3), 397–408. https://doi.org/10.1016/S0006-3495(81)84858-8.
(113) Koenig, S. H.; Brown, R. D. Relaxation of Solvent Protons by Paramagnetic Ions and Its Dependence on Magnetic Field and Chemical Environment: Implications for NMR Imaging. *Magn. Reson. Med.* **1984**, *1* (4), 478–495. https://doi.org/10.1002/mrm.1910010407.
(114) Cardoso, B. de P.; Vicente, A. I.; Ward, J. B. J.; Sebastião, P. J.; Chávez, F. V.; Barroso, S.; Carvalho, A.; Keely, S. J.; Martinho, P. N.; Calhorda, M. J. Fe(III) salEen Derived Schiff Base Complexes as Potential Contrast Agents. *Inorganica Chim. Acta* **2015**, *432*, 258–266. https://doi.org/10.1016/j.ica.2015.04.026.

(115) Grabowski, S. J. From Weak Interactions to Covalent Bonds: Weak, Moderate and Strong Hydrogen Bonds. In *Understanding Hydrogen Bonds*; 2020; pp 334–367. https://doi.org/10.1039/9781839160400-00334.
(116) Botta, M. Second Coordination Sphere Water Molecules and Relaxivity of Gadolinium(III) Complexes: Implications for MRI Contrast Agents. *Eur. J. Inorg. Chem.* **2000**, *2000* (3), 399–407. https://doi.org/10.1002/(SICI)1099-0682(200003)2000:3<399::AID-EJIC399>3.0.CO;2-B.
(117) Fanali, G.; di Masi, A.; Trezza, V.; Marino, M.; Fasano, M.; Ascenzi, P. Human Serum Albumin: From Bench to Bedside. *Mol. Aspects Med.* **2012**, *33* (3), 209–290. https://doi.org/10.1016/j.mam.2011.12.002.
(118) Sudlow, G.; Birkett, D. J.; Wade, D. N. The Characterization of Two Specific Drug Binding Sites on Human Serum Albumin. *Mol. Pharmacol.* **1975**, *11* (6), 824–832.
(119) Sudlow, G.; Birkett, D. J.; Wade, D. N. Further Characterization of Specific Drug Binding Sites on Human Serum Albumin. *Mol. Pharmacol.* **1976**, *12* (6), 1052–1061.
(120) Zsila, F. Subdomain IB Is the Third Major Drug Binding Region of Human Serum Albumin: Toward the Three-Sites Model. *Mol. Pharm.* **2013**, *10* (5), 1668–1682. https://doi.org/10.1021/mp400027q.
(121) Longo, D. L.; Arena, F.; Consolino, L.; Minazzi, P.; Geninatti-Crich, S.; Giovenzana, G. B.; Aime, S. Gd-AAZTA-MADEC, an Improved Blood Pool Agent for DCE-MRI Studies on Mice on 1 T Scanners. *Biomaterials* **2016**, *75*, 47–57. https://doi.org/10.1016/j.biomaterials.2015.10.012.
(122) Mino, Y.; Kitagaki, H.; Sasaki, M.; Ishii, K.; Mori, T.; Yamada, K.; Nagasawa, O. Characterization of Fe(III)-Deferoxamine and Mn(II)-Pectin as Magnetic Resonance Imaging Contrast Agents. *Biol. Pharm. Bull.* **1998**, *21* (12), 1385–1388. https://doi.org/10.1248/bpb.21.1385.
(123) Worah, D.; Berger, A. E.; Burnett, K. R.; Howard, H.; Kanal, E.; Kendall, C.; Leese, P. T.; Lyons, K. P.; Ross, E.; Wolf, G. L.; Quay, S. C. Ferrioxamine as a Magnetic Resonance Contrast Agent Preclinical Studies and Phase I and II Human Clinical Trials. *Invest. Radiol.* **1988**, *23*, S281. https://doi.org/10.1097/00004424-198809001-00061.
(124) Duewell, S.; Wüthrich, R.; Von Schulthess, G. K.; Jenny, H. B.; Muller, R. N.; Moerker, T.; Fuchs, W. F. Nonionic Polyethylene Glycol-Ferrioxamine as a Renal Magnetic Resonance Contrast Agent. *Invest. Radiol.* **1991**, *26* (1), 50–57. https://doi.org/10.1097/00004424-199101000-00010.
(125) Dumas, S.; Jacques, V.; Sun, W.-C.; Troughton, J. S.; Welch, J. T.; Chasse, J. M.; Schmitt-Willich, H.; Caravan, P. High Relaxivity Magnetic Resonance Imaging Contrast Agents Part 1: Impact of Single Donor Atom Substitution on Relaxivity of Serum Albumin-Bound Gadolinium Complexes. *Invest. Radiol.* **2010**, *45* (10), 600–612. https://doi.org/10.1097/RLI.0b013e3181ee5a9e.
(126) Maheshwaran, D.; Nagendraraj, T.; Balaji, T. S.; Kumaresan, G.; Kumaran, S. S.; Mayilmurugan, R. Smart Dual T1 MRI-Optical Imaging Agent Based on a Rhodamine Appended Fe(III)-Catecholate Complex. *Dalton Trans.* **2020**, *49* (41), 14680–14689. https://doi.org/10.1039/D0DT02364G.
(127) Baroni, S.; Ruggiero, M. R.; Bitonto, V.; Broche, L. M.; Lurie, D. J.; Aime, S.; Geninatti Crich, S. In Vivo Assessment of Tumour Associated Macrophages in Murine

Melanoma Obtained by Low-Field Relaxometry in the Presence of Iron Oxide Particles. *Biomaterials* **2020**, *236*, 119805. https://doi.org/10.1016/j.biomaterials.2020.119805.
(128) Aghighi, M.; Golovko, D.; Ansari, C.; Marina, N. M.; Pisani, L.; Kurlander, L.; Klenk, C.; Bhaumik, S.; Wendland, M.; Daldrup-Link, H. E. Imaging Tumor Necrosis with Ferumoxytol. *PLOS ONE* **2015**, *10* (11), e0142665. https://doi.org/10.1371/journal.pone.0142665.
(129) Lu, M.-Y.; Wang, N.; Wu, W.-H.; Lai, C.-W.; Kuo, P.-H.; Chiang, P.-H.; Lin, K.-H.; Wu, T.-H. Simultaneous Determination of Plasma Deferasirox and Deferasirox-Iron Complex Using an HPLC-UV System and Pharmacokinetics of Deferasirox in Patients With β-Thalassemia Major: Once-Daily Versus Twice-Daily Administration. *Clin. Ther.* **2015**, *37* (8), 1751–1760. https://doi.org/10.1016/j.clinthera.2015.05.506.
(130) Boehm-Sturm, P.; Haeckel, A.; Hauptmann, R.; Mueller, S.; Kuhl, C. K.; Schellenberger, E. A. Low-Molecular-Weight Iron Chelates May Be an Alternative to Gadolinium-Based Contrast Agents for T1-Weighted Contrast-Enhanced MR Imaging. *Radiology* **2017**, *286* (2), 537–546. https://doi.org/10.1148/radiol.2017170116.
(131) Svenskaya, Y.; Garello, F.; Lengert, E.; Kozlova, A.; Verkhovskii, R.; Bitonto, V.; Ruggiero, M. R.; German, S.; Gorin, D.; Terreno, E. Biodegradable Polyelectrolyte/Magnetite Capsules for MR Imaging and Magnetic Targeting of Tumors. *Nanotheranostics* **2021**, *5* (3), 362–377. https://doi.org/10.7150/ntno.59458.
(132) Palagi, L.; Di Gregorio, E.; Costanzo, D.; Stefania, R.; Cavallotti, C.; Capozza, M.; Aime, S.; Gianolio, E. Fe(Deferasirox)2: An Iron(III)-Based Magnetic Resonance Imaging T1 Contrast Agent Endowed with Remarkable Molecular and Functional Characteristics. *J. Am. Chem. Soc.* **2021**, *143* (35), 14178–14188. https://doi.org/10.1021/jacs.1c04963.
(133) Gascon, J. M.; Oliveri, V.; McGown, A.; Kaya, E.; Chen, Y.-L.; Austin, C.; Walker, M.; Platt, F. M.; Vecchio, G.; Spencer, J. Synthesis and Study of Multifunctional Cyclodextrin–Deferasirox Hybrids. *ChemMedChem* **2019**, *14* (16), 1484–1492. https://doi.org/10.1002/cmdc.201900334.
(134) Bruns, C. J. Exploring and Exploiting the Symmetry-Breaking Effect of Cyclodextrins in Mechanomolecules. *Symmetry* **2019**, *11* (10), 1249. https://doi.org/10.3390/sym11101249.
(135) Del Valle, E. M. M. Cyclodextrins and Their Uses: A Review. *Process Biochem.* **2004**, *39* (9), 1033–1046. https://doi.org/10.1016/S0032-9592(03)00258-9.
(136) Braga, S. S. Cyclodextrins: Emerging Medicines of the New Millennium. *Biomolecules* **2019**, *9* (12), 801. https://doi.org/10.3390/biom9120801.
(137) Ghosh, S.; Paul, B. K.; Chattopadhyay, N. Interaction of Cyclodextrins with Human and Bovine Serum Albumins: A Combined Spectroscopic and Computational Investigation. *J. Chem. Sci.* **2014**, *126* (4), 931–944. https://doi.org/10.1007/s12039-014-0652-6.
(138) Gao, H.; Wang, Y.-N.; Fan, Y.-G.; Ma, J.-B. Interactions of Some Modified Mono- and Bis-β-Cyclodextrins with Bovine Serum Albumin. *Bioorg. Med. Chem.* **2006**, *14* (1), 131–137. https://doi.org/10.1016/j.bmc.2005.08.002.
(139) Samra, H. S.; He, F.; Bhambhani, A.; Pipkin, J. D.; Zimmerer, R.; Joshi, S. B.; Middaugh, C. R. The Effects of Substituted Cyclodextrins on the Colloidal and

Conformational Stability of Selected Proteins. *J. Pharm. Sci.* **2010**, *99* (6), 2800–2818. https://doi.org/10.1002/jps.22053.

Publications and conference presentations

Peer-reviewed manuscripts

Stefania, R. [§], **Palagi, L. [§]**, Di Gregorio, E., Ferrauto, G., Dinatale, V., Aime, S., & Gianolio, E. (2023). Seeking for Innovation with Magnetic Resonance Imaging Paramagnetic Contrast Agents: Relaxation Enhancement via Weak and Dynamic Electrostatic Interactions with Positively Charged Groups on Endogenous Macromolecules. *Journal of the American Chemical Society*. https://doi.org/10.1021/jacs.3c06275. [§]: these authors contributed equally to this work.

Abstract: Gd-L1 is a macrocyclic Gd-HPDO3A derivative functionalized with a short spacer to a trisulfonated pyrene. When compared to Gd-HPDO3A, the increased relaxivity appears to be determined by both the higher molecular weight and the occurrence of an intramolecularly catalyzed prototropic exchange of the coordinated OH moiety. In water, Gd-L1 displayed a relaxivity of 7.1 mM^{-1} s^{-1} (at 298 K and 0.5 T), slightly increasing with the concentration likely due to the onset of intermolecular aggregation. A remarkably high and concentration-dependent relaxivity was measured in human serum (up to 26.5 mM^{-1} s^{-1} at the lowest tested concentration of 0.005 mM). The acquisition of ^{1}H-nuclear magnetic relaxation dispersion (NMRD) and ^{17}O-R_2 vs. T profiles allowed to get an in-depth characterization of the system. *In vitro* experiments in the presence of human serum albumin, γ-globulins, and polylysine, as well as using media mimicking the extracellular matrix, provided strong support to the view that the trisulfonated pyrene fosters binding interactions with the exposed positive groups on the surface of proteins, responsible for a remarkable *in vivo* hyperintensity in T_{1w} MR images. The *in vivo* MR images of the liver, kidneys, and spleen showed a marked contrast enhancement in the first 10 min after the i.v. injection of Gd-L1, which was 2–6-fold higher than that for Gd-HPDO3A, while maintaining a very similar excretion behavior. These findings may pave the way to an improved design of MRI GBCAs, for the first time, based on the setup of weak and dynamic interactions with abundant positive groups on serum and ECM proteins.

Palagi, L., Di Gregorio, E., Costanzo, D., Stefania, R., Cavallotti, C., Capozza, M., Aime S., & Gianolio, E. (2021). Fe (deferasirox)$_2$: An Iron (III)-Based Magnetic Resonance Imaging T_1 Contrast Agent Endowed with Remarkable Molecular and Functional Characteristics. *Journal of the American Chemical Society*, *143*(35), 14178-14188. https://doi.org/10.1021/jacs.1c04963

Abstract: The search for alternatives to Gd-containing magnetic resonance imaging (MRI) contrast agents addresses the field of Fe(III)-bearing species with the expectation that the use of an essential metal ion may avoid the issues raised by the exogenous Gd. Attention is currently devoted to highly stable Fe(III) complexes with hexacoordinating ligands, although they may lack any coordinated water molecule. We found that the hexacoordinated Fe(III) complex with two units of deferasirox, a largely used iron sequestering agent, owns properties

that can make it a viable alternative to Gd-based agents. Fe(deferasirox)$_2$ displays an outstanding thermodynamic stability, a high binding affinity to human serum albumin (three molecules of complex are simultaneously bound to the protein), and a good relaxivity that increases in the range 20–80 MHz. The relaxation enhancement is due to second sphere water molecules likely forming H-bonds with the coordinating phenoxide oxygens. A further enhancement was observed upon the formation of the supramolecular adduct with albumin. The binding sites of Fe(deferasirox)$_2$ on albumin were characterized by relaxometric competitive assays. Preliminary *in vivo* imaging studies on a tumor-bearing mouse model indicate that, on a 3 T MRI scanner, the contrast ability of Fe(deferasirox)$_2$ is comparable to the one shown by the commercial Gd(DTPA) agent. ICP-MS analyses on blood samples withdrawn from healthy mice administered with a dose of 0.1 mmol/kg of Fe(deferasirox)$_2$ showed that the complex is completely removed in 24 h.

Sforzi, J. [§], **Palagi, L.** [§], & Aime, S. (2020). Liposome-Based Bioassays. *Biology*, *9*(8), 202. https://doi.org/10.3390/biology9080202. [§]: these authors contributed equally to this work.

Abstract: This review highlights the potential of using liposomes in bioassays. Liposomes consist of nano- or micro-sized, synthetically constructed phospholipid vesicles. Liposomes can be loaded with a number of reporting molecules that allow a dramatic amplification of the detection threshold in bioassays. Liposome-based sensors bind or react with the biological components of targets through the introduction of properly tailored vectors anchored on their external surface. The use of liposome-based formulations allows the set-up of bioassays that are rapid, sensitive, and often suitable for in-field applications. Selected applications in the field of immunoassays, as well as recognition/assessment of corona proteins, nucleic acids, exosomes, bacteria, and viruses are surveyed. The role of magnetoliposomes is also highlighted as an additional tool in the armory of liposome-based systems for bioassays.

Manuscripts in preparation

Palagi, L., Aime S., & Gianolio, E. *A relaxometric method to highlight binding interactions of GBCAs in biological media*.

Palagi, L., Carrera, C., Costanzo, D., Aime S., & Gianolio, E. *Towards new concepts in the design of improved Gd-based MRI contrast agents*.

Palagi, L., Aime S., & Gianolio, E. *Fe(III) complexes deferasirox-β-cyclodextrin hybrids as MRI T_1 contrast agents*.

Conference presentations

- *Relaxation enhancement via reversible, weak, electrostatic/cation-π interactions with protonated amino groups on endogenous macromolecules.* EMIM 2024 – Porto (Portugal), March 12-15, 2024. Oral presentation.

- *Relaxation enhancement via reversible, weak, electrostatic/cation-p interactions with protonated amino groups on endogenous macromolecules.* ESMRMB-GREC 2022 – Basel (Switzerland), October 4-7, 2023. Oral presentation – invited speaker.

- *Simultaneous PET/MRI can measure pH in the tumor microenvironment.* EMIM 2023 – Salzburg (Austria), March 14-17, 2024. Oral presentation.

- *Iron(III) complexes of deferasirox-β-cyclodextrin hybrids as potential MRI T_1 contrast agents.* 1st Workshop on Emerging Trends in Molecular Imaging – Torino (Italy), April, 19-20, 2023. Poster presentation.

- *Increasing Relaxivity to reduce GBCA doses: the current approaches.* ESMRMB-GREC 2022 – Roma (Italy), November 10-11, 2022. Oral presentation – invited speaker.

- *Fe(deferasirox)$_2$: A novel MRI contrast agent endowed with remarkable molecular and functional characteristics*. WMIC 2021 (virtual) – Miami, Florida (USA), October 6-9, 2021. Poster presentation and flash talk.

- *A novel iron(III)-based MRI T_1 contrast agent endowed with remarkable molecular and functional properties*. XXVII Congresso Nazionale della Società Chimica Italiana (virtual) – Milano (Italy), September 14-23 2021. Poster presentation.

- *Towards new concepts in the design of Gadolinium Based Magnetic Resonance Contrast Agents.* Merck Young Chemists' Symposium 2019 – Rimini (Italy), November 25-27, 2019. Poster presentation and flash talk.